Dielectric and Spin Susceptibilities using Density Functional Theory

Yusuf Aziz

Department of Physics
Royal Holloway University of London

This dissertation is submitted for the degree of
Doctor of Philosophy

August 2023

I would like to dedicate this thesis to my beloved grandfather . . .

Declaration

I hereby declare that except where specific reference is made to the work of others, the contents of this dissertation are original and have not been submitted in whole or in part for consideration for any other degree or qualification in this, or any other university. This dissertation is my own work and contains nothing which is the outcome of work done in collaboration with others, except as specified in the text and Acknowledgements. This dissertation contains fewer than 65,000 words including appendices, bibliography, footnotes, tables and equations and has fewer than 150 figures.

Yusuf Aziz
August 2023

Acknowledgements

First and foremost, I would like to thank my supervisor, Keith Refson. Your advice, insight and patience have been invaluable. In spite of retiring from the university mid-pandemic, I am extremely grateful that you were able to maintain frequent contact and see this thesis to completion. I am grateful for our stimulating discussions on Density Functional Theory and the CASTEP package.

Thank you to my friends and colleagues who have supported me over the years and were able to provide feedback on this work.

Thanks to the Royal Holloway Badminton team/community for providing me with an opportunity to represent the university at a competitive level and providing that outlet.

I am grateful to both Royal Holloway and the ISIS facility of Rutherford Appleton Laboratory for funding the Doctorate. I acknowledge the use of high-performance computing facilities provided by the STFC Scientific Computing Department's SCARF cluster and Royal Holloway.

Finally, I would like to thank my parents for their support throughout.

Abstract

The response of a system to some external perturbation is almost ubiquitous in Physics. The application of perturbation theory through an electronic structure method such as Density Functional Theory has had significant contributions over the last few decades. Its implementation, aptly named Density Functional Perturbation Theory has seen use in a number of *ab initio* calculations on a variety of physical properties of materials which depend on their lattice-dynamical behaviour. Specific heats, thermal expansion, infrared, Raman and optical spectra are to name just a few. Understanding the complex phenomena has significantly corroborated the current understanding of the quantum picture of solids. The Sternheimer scheme falls under the umbrella of methods to compute response functions in Time-Dependent Density Functional Theory. Initially developed to study the electronic polarisability, it is now commonly utilised in the field of lattice dynamics to study phonons and related crystal properties. The Sternheimer equation has also been used to model spin wave excitations by computation of the magnetic susceptibility. The poles of the susceptibility are known to correspond to magnon excitations and these computations have been corroborated by experimental inelastic neutron scattering data. These excitations are of a transverse nature, in that they involve fluctuations of the magnetisation perpendicular to a chosen z axis. The lesser-known longitudinal excitations involve fluctuations of the magnetisation along z, an investigation of collective modes present in transition metals may be carried out from self-consistent computations of the Sternheimer equation. The dielectric response is an important linear response function in solid-state physics. Its computation from first principles provides an invaluable tool in the characterisation of optical properties and can be compared to the experimental method of spectroscopic ellipsometry.

The work in this thesis concerns the implementation of the Sternheimer method in computing the dynamical response from either an external plane wave or spin-polarised perturbation. These response functions are the dielectric and spin (magnetisation) susceptibilities respectively.

The scheme to compute the frequency-dependent dielectric response is implemented in a plane-wave pseudopotential DFT package. Calculations are performed on the semiconducting systems of Silicon, Gallium Arsenide, Zinc Oxide and perovskite Methylammonium Lead Triiodide. The overall shape of the dielectric spectra is in good agreement with spectroscopic ellipsometry data, however, there is a shift which is attributed to the limitations of DFT.

The scheme developed to compute longitudinal spin dynamics is applied to the transition metal systems of body-centred cubic Iron and face-centred cubic Nickel. In a similar manner to another first principles approach, a single dominant peak is shown to be present in the magnetisation channel with the charge dynamics being effectively null in comparison. However, the exact position of these peaks is not in agreement with the other approach, a discussion is made regarding difficulties pertaining to self-consistent optimisation.

Table of contents

List of figures

List of tables

Chapter 1

Introduction

Electronic interactions form the fundamental fabric of nature. As the first elementary particle identified by J. J. Thomson in 1897, it marked a pivotal moment in the history of physics [1]. Thomson's experiments on cathode rays led to the identification of tiny, negatively charged particles that came to be known as electrons. This discovery challenged the prevailing classical understanding of physics and was followed by work from Robert A. Millikan which precisely determined the electron charge in 1913 [2].

These discoveries paved the way for the development of quantum mechanics, which provided a comprehensive framework for understanding the behaviour of electrons and other subatomic particles. Max Planck's quantum hypothesis in 1900 was corroborated by experimental observation and provided strong evidence that the energy of electron motion in matter is quantised [3]. Louis De Broglie proposed the wave-particle duality in 1924, suggesting that electrons exhibit wave-like characteristics, challenging the notion that such particles were necessarily localised [4]. Stimulated by this study, Erwin Schrödinger developed the wave equation in 1926, describing the behaviour of electrons through a mathematical function that he denoted as the wavefunction. This equation is central to this thesis and presents the mathematical formalism employed to calculate the probability distribution of finding electrons (or other quantum particles) in different states [5]. Werner Heisenberg's uncertainty principle, formulated in 1927, highlighted the inherent probabilistic nature of quantum mechanics and posed a fundamental limit to the precision of simultaneous measurements [6]. Paul Dirac in the late 1920s, whilst working on the quantum mechanics of systems with magnetic moments, realised that the electron had to possess an intrinsic angular momentum, which is now known as electron spin. This laid the foundation for quantum electrodynamics (QED), the theory of how electrons and photons interact. QED is one of the most successful

and precise theories in physics, accurately describing the behaviour of charged particles and electromagnetic interactions [7, 8]. Much of the technological advancements and discoveries of the 20th century were made possible due to the growing understanding of electronic interactions. From the use of semiconductors which form a critical part of every electronic device to lasers which have various uses in industry, medicine and communications.

1.1 Modelling Electronic Structure

Scientific simulations act as a powerful tool to bridge the gap between theoretical concepts and experimental observations [9]. The validity of a theoretical approach can be verified by comparing simulation to experimental data, potentially highlighting issues with the underlying model. Simulations provide a platform for testing hypotheses and exploring the effects of different parameters or variables on system behaviour. The simulation can be regarded as a virtual experiment and input parameters can be conveniently manipulated, allowing one to observe how changes impact the system [10]. This iterative process helps refine theories and gain a deeper understanding of the underlying mechanisms. There are often variables such as high temperature or pressure in which a researcher would want to study a prospective system. However, these are sometimes inaccessible or impractical to achieve experimentally; computational modelling provides a viable solution. An example particularly relevant in modern science is the search for high-energy storage capacity materials [11]. Without computational simulation, researchers would be restricted to the approach of synthesising various materials along with physical property measurements in attempts to find viable candidates. These processes are iterative and can be time-consuming as well as resource-intensive. Computational modelling in this instance aims to complement and accelerate this search with the ability for researchers to predict and screen systems before any experimental synthesis and testing. This hybrid approach is efficient and has been used to develop battery technologies [12, 13, 14].

Significant technological advances over the past decades have paved the bridge for novel computational simulation techniques [9]. In the field of electronic structure, the principle problem is to solve the (N) many-body Schrödinger equation [9, 15]:

$$H\psi(\boldsymbol{x}_1,...,\boldsymbol{x}_N) = E\psi(\boldsymbol{x}_1,...,\boldsymbol{x}_N), \tag{1.1}$$

where the Hamiltonian H contains the kinetic and potential interaction terms of the electrons, nuclei and the solution ψ describes the wavefunction associated with the eigenvalue E.

This solution, if found, is a powerful quantum mechanical object which encodes all the information of the system. However, despite modern high-performance computing, a direct numerical solution to the Schrodinger equation is unfeasible. The i-th electron position in the d-th dimension is denoted above by $\boldsymbol{x}_i = (x_{1,i}, ..., x_{d,i})$. Accordingly, an N electron system necessitates ψ to be a $d \cdot N$ dimensional object. Contextualising this within the context of modern computing, where storage and handling of the wavefunction are required. If a uniform discretisation of the wavefunction is assumed with an order of $O(K)$ points in each direction, it follows that the resulting wavefunction which must be stored involves $O(K^{d \cdot N})$ degrees of freedom. Assuming the usual $d = 3, N > 1$ and it becomes clear that storing this wavefunction is unfeasible. Consequently, there has been significant attention to developing various approximations and implementations to obtain the many-body wavefunction. Quantum Monte Carlo methods [16] deal directly with the interacting many-body wavefunction and the Hartree-Fock (HF) scheme [17] involves several approximations which make the computation feasible. This thesis is concerned with the development of Density Functional Theory (DFT) and its implementations in determining excited-state properties.

Over the past few decades, DFT has emerged as one of the most extensively employed methods for calculating the properties of electronic systems [9, 15, 18]. The fundamental concept revolves around a single quantity, the electronic density, which is proposed to contain all the information needed to extract the many-body wave function. Initially, this seems unlikely, the complicated N electron wavefunction is encapsulated in a simple scalar function of three variables in position. However, Hohenberg and Kohn (H-K) were able to show that the ground-state energy of a quantum system can be determined by minimising the energy as a *functional* of the density [19]. The energy is a function of the density which itself is also a function. The implementation of this to the many-body Schrödinger equation results in the Kohn-Sham (KS) equations, which in principle, correspond exactly to the ground-state density and energy [20]. This simplification of dealing with an electronic density that has x, y and z coordinates instead of the many-body wavefunction that scales exponentially with N electrons renders such computations feasible with modern technology.

H-K were able to show the correspondence of the electronic charge density and energy of the many-body wavefunction by postulating an exact functional [19]. Whilst H-K rigorously proved that a functional of the electron density exists, nothing was said about the actual form [9, 18]. This is one of the reasons why early DFT computations did not capture the serious interest of chemists [21]. Various approximations needed to be made to account for the exchange and correlation of electronic behaviour. Moreover, there exists no systematic procedure to refine the exact form of the functional. A competing electronic structure method favoured by chemists in the 20th century is the Hartree-Fock (HF) method [21]. The electron

is described in HF as a product of one-electron orbitals organised to the Pauli exclusion principle. The method accounts for Coulomb and exchange interactions of electrons but does not consider any correlation [9, 17]. However, HF could in principle be extended to more sophisticated approaches such as configuration interaction, which involves incorporating electron correlation effects beyond the mean-field approximation of HF [22]. The ideas accounting for electrostatics and exchange in HF were utilised by KS who also included correlation which resulted in a practical methodology to apply DFT to molecules and solids [20, 23]. Indeed, the overwhelming majority of DFT computations used today specifically employ the formalism introduced by Kohn and Sham [24].

Amongst the earliest DFT calculations include the works of Gunnarsson *et al* (1976), on computing the system energy of small diatomic molecules [25]. It was a success, even though a naive approach was made in using correlation from the homogeneous electron gas [26], DFT computations of properties such as dipole moments and binding energies exhibited better agreement with experimental data compared to HF calculations [27]. The program efficiency of these emerging methods was discussed through how they scaled with basis functions, a set of functions in which some linear combination is used to model the electronic wavefunction. An early work of Johnson *et al* in 1992 is mentioned for the interested reader [28]. The program used in the study (GAUSSIAN 92) demonstrated that DFT scales favourably in comparison to HF, with the number of basis set functions scaling an order of magnitude lower than HF [28]. Modern electronic structure packages make use of powerful linear algebra libraries [29] and parallel communications [30]. It is not as trivial to indicate which method is more efficient regardless of the system or physical property to be computed. Nevertheless, the relatively resource-efficient approach of handling the electron density as opposed to the many single-orbital wavefunctions of HF, has garnered significant computational advancements for the method's versatility across a broad spectrum of systems and properties [9, 15, 18]. The distribution of reference citations presents an exponential growth of DFT publications from an approximate period of 1970s to the late 1990s [21]. Since 2000, DFT-related publications have shown linear growth, with the current publication volume doubling every 5-6 years [24].

Owing to a significant scientific and computational effort, DFT has been used to calculate various properties of materials from first principles. These calculations, termed *ab initio*, are performed solely on fundamental physical principles and do not require the use of empirical parameters or experimental data. The Car-Parrinello method of 1985 introduced a practical approach to determining electronic structure and atomic positions [31]. This set a series of computational developments which is still in use today within first principles codes to perform molecular dynamics simulations [32]. Complex DFT calculations, which were

once computationally prohibitive, are now within reach, allowing for more accurate and comprehensive investigations of a wide range of materials and properties. Determination of lattice constants (equilibrium structure) [33, 34], binding energies [35], thermodynamic [36] and mechanical properties such as elastic constants [37] demonstrate the breadth of capability. This has been achievable owing to advancements in computational technology.

1.2 High Performance Computing

High performance computing (HPC) refers to the use of advanced computing technologies and systems to solve complex problems such as the many-body Schrödinger equation [38]. The latest advancements over the years include the widespread adoption of multicore processors with manufacturers continuing to increase the number of cores and processor clock speed [39]. The instruction set architectures for these processors have also been refined with optimisation to features such as SIMD (Single Instruction, Multiple Data), these allow processors to perform the same operation on multiple data elements simultaneously. For the dense linear algebra operations, particularly matrix-matrix multiplications utilised in DFT to solve the Kohn-Sham equations, these result in a computational speedup [40]. Advancements in reducing memory latency and improving data access speed over time have enabled faster computation and reduced data bottlenecks [39].

The introduction of parallel computing architectures and standards such as the Message Passing Interface (MPI) has allowed researchers to fully leverage the power of distributed systems [30]. These clusters offer scalability and efficiency with the ability to progressively scale resources to accommodate larger problem sizes and serve more users with varying requirements. The availability of high-performance libraries and tools built on MPI is utilised by scientific codes to optimise algorithms. The DFT package employed in this thesis utilises the Fast Fourier Transform, and the MPI interface ensures efficient communication as well as valid data distribution of the calculation amongst parallel processes [41]. It is often the case that a complex problem can be split into smaller, more manageable tasks that can be executed independently across different processes. The scientific code implemented in this thesis will implement parallelism that is directly related to the physics of the problem, providing clear scope for the user to understand and exploit parallel strategies.

Exascale computing refers to a level of computing performance capable of performing at least one exaflop, which is a quintillion (10^{18}) floating-point operations per second. The Frontier exascale supercomputer based at Oak Ridge National Laboratory is based on Hewlett Packard Enterprise Cray EX architecture with 9408 AMD compute nodes, each containing

a 64-core 2 Gigahertz CPU with 4 Radeon Instinct MI250X GPU's [42]. The LINPACK (Linear Algebra Package) benchmarks introduced by Jack Dongarra *et al* [43] measure how fast a computer solves a dense system of linear equations $Ax = b$, where A is a square matrix and x and b are vectors. Systems of this type are typical in the fields of engineering, computer science, economics and physics [44, 45]. Later on, it will be demonstrated that the solutions to these linear systems play a crucial role in the research presented in this thesis. The LINPACK 500 benchmark is widely recognised in the HPC community to assess and compare the computing performance of different systems, particularly for large-scale scientific simulations and data-intensive applications [46]. As of June 2023, Frontier has retained the first position in the TOP500, surpassing the Japanese Fugaku HPC system the previous year [47]. Typical use cases for Frontier include cosmological hydrodynamic simulations in efforts to accurately model the universe [48]. The system is host to the development and application of atmospheric modelling with the Energy Exascale Earth System Model (E3SM) project [49]. In particular, the Simple Cloud Resolving E3SM Atmosphere Model (SCREAM) is being run on the exascale system [50]. Resolving clouds is a famously challenging task for climate models, which typically operate at resolutions too coarse to represent clouds. The GPU-optimised SCREAM model was able to complete a simulated year of the global climate in a single day with resolved clouds and a 3.25 kilometre resolution [50]. This enhanced predictive ability is of great interest to researchers to predict how precipitation in various regions will change with the warming climate. There are several artificial intelligence and machine learning algorithms being explored which have profound applications in geological modelling and engineering [51]. Work is currently underway to optimise quantum mechanical simulations from first principles which will be used to investigate material properties as well as molecular processes [52, 53]. These have prospects of improving current energy storage and transport technologies [54, 55].

1.3 Linear Response

A widely employed approach to investigate the behaviour of electrons is to introduce a perturbation and analyse the resulting response. An electromagnetic field often serves as a suitable probe to investigate electron dynamics [9, 15]. Additionally, other particles such as beams of neutrons are used to explore various physical phenomena [56]. In principle, this concept forms the basis for all scattering/spectroscopic experimental techniques, including, but not limited to, spectroscopic ellipsometry, inelastic neutron scattering, Raman and electron energy loss spectroscopy [57, 58, 59].

The theoretical analogue to the above can be realised with the field of perturbation theory [60]. Starting with a system of equations that describe a system, applying some perturbation (in the form of some external field) and then solving for the perturbed system. The nature of this perturbation is of particular interest, it is clear that there must be a time dependence which is characterised by the perturbation [61]. If not, then by causality, it is entirely unclear as to whether the response of the system was indeed due to the perturbation. Considering the electron interaction with experimental probes as *small* disturbances to the system serves as a starting point for constructing a linear function that encapsulates electron behaviour [15].

In essence, the purpose of a response function is to provide a mapping between an external field and some physical observable. It is proposed that this response can be expanded in a power series with respect to the field strength, provided that the external field is weak [62]. Taking this perturbation to first-order and computing this function is the objective of linear response theory. For an observable A and an external field F, the linear response of the observable [63]:

$$\delta A^{(1)}(\boldsymbol{r},t) = \int dt' \int d\boldsymbol{r}' \chi(\boldsymbol{r},\boldsymbol{r}',t-t')\delta F^{(1)}(\boldsymbol{r}',t'), \tag{1.2}$$

where χ is defined to be the linear response function and $\delta F^{(1)}$ is the external field expanded to first order in field strength. One such example of a response function is the polarisability, which connects the first-order response of an electric dipole moment to an applied electric field [64]. The magnetic susceptibility connects the first-order response of a magnetic moment to a magnetic field perturbation [65, 66]. The work presented in this thesis will show that response functions can be computed by using properties of the unperturbed system. These response functions are shown to correspond to physical quantities which can be compared to experimental data.

The formulation of linear response in computing the physical quantities of a system away from equilibrium can be traced back to the works of Kubo [67]. Whilst the theoretical framework was applied to statistical thermodynamics, one can apply the approach of Kubo to explore the dynamic properties of materials in the condensed matter regime [60, 67]. It follows that in order to implement a perturbative-based formalism, one must already have knowledge of the equilibrium state. In principle, the theoretical framework introduced by Hohenberg and Kohn is exact for determining the ground-state [19]. Runge and Gross developed a comparable density-functional formalism for arbitrary time-dependent systems [68], approximately 20 years after the seminal papers of DFT were published. This prompted the development of a series of practical schemes that extended time-dependence to the

KS electron density and KS orbitals for subsequent use in perturbative computations. The first practical calculations of linear response Time-Dependent Density Functional Theory (TDDFT) were performed in the early 2000s [69, 70]. Various phenomena related to optical response and excited states comprised the majority of early TDDFT computations [71, 72, 73].

Within the field of TDDFT, there are several methods available for calculating response functions. The time-propagation method of Yabana and Bertsch [74], involves a numerical time-stepping scheme which propagates the KS orbitals [75]. The Sternheimer scheme takes an alternative approach of transforming the KS equations to frequency space [63]. Provided that the time-dependent external perturbation is weak, the KS states and Hamiltonian are expanded in a power series after which the response quantities can be extracted [64]. This scheme is central to the work of this thesis and a later discussion will demonstrate how only occupied KS states are involved in computing the response, highlighting computational efficiency [76]. Another TDDFT method derived by Casida follows from the Sternheimer formalism [77]. The response quantities are derived from a sum-over-states expansion of the KS orbitals which includes unoccupied states. The Casida scheme is typically used in the determination of excitation energies and absorption spectra [78, 79]. All of these methods are grounded in KS DFT and are formally equivalent, yet numerically distinct implementations to compute physical quantities. Whilst the work in this thesis will restrict the Sternheimer expansion to linear terms, it is possible to generalise to higher orders [80].

1.4 The Classic Harmonic Oscillator

Whilst this work will exclusively focus on the linear response regime in quantum mechanics, a number of key findings can be obtained from an example in classical physics. The development of linear response with respect to the damped harmonic oscillator will be presented here [81]. First, the equation of motion in the presence of some driving force is

$$\frac{d^2x}{dt^2} + \gamma\frac{dx}{dt} + \omega_0^2 x = F(t), \tag{1.3}$$

where γ is the damping constant and ω_0 is the natural frequency of the oscillator. In the linear response regime, as discussed in equation (1.2), the response function $\chi(t-t')$ maps the motion of the system to the driving force:

$$x(t) = \int_{-\infty}^{+\infty} dt' \chi(t-t') F(t'). \tag{1.4}$$

Now the form of $\chi(t)$ is required; the inverse Fourier transform:

$$\chi(t) = \int_{-\infty}^{+\infty} \frac{d\omega}{2\pi} e^{-i\omega t} \chi(\omega). \tag{1.5}$$

Substituting this into equation (1.3):

$$\int_{-\infty}^{+\infty} \frac{d\omega}{2\pi} \int_{-\infty}^{+\infty} dt' \left[-\omega^2 - i\gamma\omega + \omega_0^2\right] e^{-i\omega(t-t')} \chi(\omega) F(t') = F(t). \tag{1.6}$$

As the delta function is written as

$$\delta(t) = \frac{1}{2\pi} \int_{-\infty}^{+\infty} d\omega e^{-i\omega t}. \tag{1.7}$$

The form of the response function required in order to satisfy equation (1.6) is

$$\chi(\omega) = \frac{1}{-\omega^2 - i\gamma\omega + \omega_0^2}. \tag{1.8}$$

It is now useful to look at the real and imaginary parts of the response. Multiplying both the numerator and denominator of (1.8) by $\left[\left(\omega_0^2 - \omega^2\right) + i\gamma\omega\right]$ and simplifying:

$$\mathrm{Re}\left[\chi(\omega)\right] = \chi'(\omega) = \frac{\omega_0^2 - \omega^2}{\left(\omega_0^2 - \omega^2\right)^2 + \gamma^2\omega^2}, \tag{1.9}$$

and the imaginary part:

$$\mathrm{Im}\left[\chi(\omega)\right] = \chi''(\omega) = \frac{\omega\gamma}{\left(\omega_0^2 - \omega^2\right)^2 + \gamma^2\omega^2}, \tag{1.10}$$

where the notation for the response is of the form:

$$\chi(\omega) = \chi'(\omega) + i\chi''(\omega). \tag{1.11}$$

Figures 1.1a, 1.1b plot the real and imaginary part of the response function for real ω and a given ω_0, γ. The real part of the response is referred to as the *reactive* part of the response, it

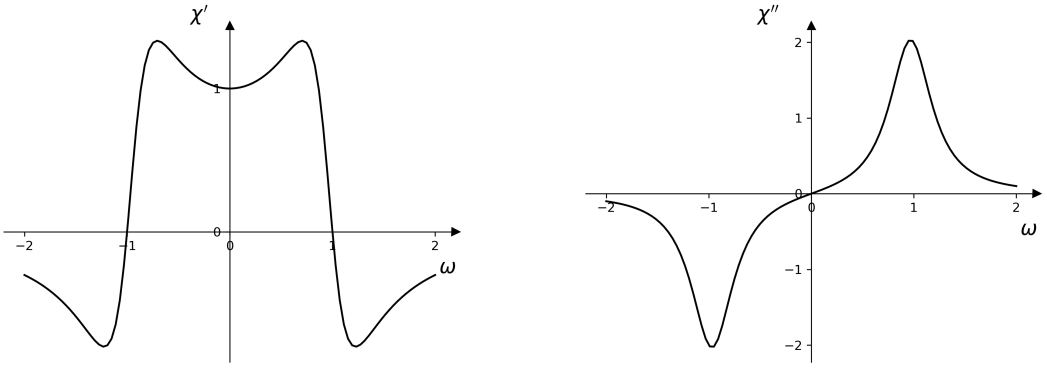

(a) Real part of the response.

(b) Imaginary part of the response.

Fig. 1.1 Components of the response function for the harmonic oscillator, plotted with $\omega_0 = 1$ and $\gamma = 0.5$

is noted to be an even function with $\chi'(\omega) = \chi'(-\omega)$. The imaginary part of the response is an odd function with $\chi''(\omega) = -\chi''(-\omega)$. Additionally, χ'' peaks around $\pm\omega_0$ (the natural frequency), the existence of these peaks and their origin is one of the main reasons as to why the imaginary part is focused upon. To understand this, the dissipation (or energy absorbed) of the system is considered:

$$\frac{dW}{dt} = F(t)\frac{dx}{dt}. \tag{1.12}$$

Inserting the response function from (1.4) and taking the inverse Fourier transform (1.5) of all functions:

$$\frac{dW}{dt} = \int_{-\infty}^{+\infty} \frac{d\omega}{2\pi}\frac{d\omega'}{2\pi}\left[-i\omega\chi(\omega)\right] e^{-i(\omega+\omega')t} F(\omega)F(\omega'). \tag{1.13}$$

The driving force is real with a frequency ν:

$$F(t) = \frac{F_0}{2}\left(e^{-i\nu t} + e^{i\nu t}\right). \tag{1.14}$$

Taking the Fourier transform and making use of the delta function (1.7):

$$F(\omega) = 2\pi F_0\left[\delta(\omega-\nu) + \delta(\omega+\nu)\right]. \tag{1.15}$$

Substituting into (1.13):

$$\frac{dW}{dt} = -iF_0^2 v \left[\chi(v)e^{-ivt} - \chi(-v)e^{+ivt}\right]\left[e^{-ivt} + e^{ivt}\right]. \tag{1.16}$$

Take the average of this over a cycle:

$$\overline{\frac{dW}{dt}} = \frac{v}{2\pi}\int_0^{2\pi/v} dt \frac{dW}{dt} = -iF_0^2 v\left[\chi(v) - \chi(-v)\right]. \tag{1.17}$$

As illustrated by figure 1.1a and in general, $\chi'(\omega)$ is an even function function whilst $\chi''(\omega)$ (shown in figure 1.1b) is an odd function. This means

$$\overline{\frac{dW}{dt}} = 2F_0^2 v\chi''(v). \tag{1.18}$$

Therefore the dissipation (work done) is proportional to χ'', explicitly written as

$$\overline{\frac{dW}{dt}} = 2F_0^2 \frac{\gamma v^2}{\left(\omega_0^2 - v^2\right)^2 + \gamma^2 v^2}. \tag{1.19}$$

At the natural frequency ($v = \omega_0$) the dissipation is at its maximum. It is at these frequencies that the system is able to absorb energy. As $\gamma \to 0$ the dissipative part of the response tends to two delta functions which are centred around $\pm v$. As will be shown in this thesis, peaks in the imaginary part of the response will be analysed. As discussed above, these peaks have a physical origin and their analysis is a powerful tool in characterising systems. Note that the relation between dissipation and χ'' follows only using the odd/even properties of the response function. In this example, as the exact form of the response is known, it is clear to see the relation of χ'' as ω approaches ω_0. However, in the *ab initio* quantum mechanical computations considered in this thesis, this relation is unknown and no analytic solution exists. What is accessible is only a spectrum of the response function at ω.

1.5 Technological Applications

The dielectric and spin response quantities computed in this thesis have numerous technological applications across various fields. Dielectric materials with a high dielectric constant are excellent candidates for capacitors [82]. The primitive structure of a capacitor consists of a dielectric material with metal plates attached to both sides. This allows for the storage and sensitive manipulation of electrical charges, as a result, they are ubiquitous in electrical

circuits. Examples of devices that employ capacitors include; amplifiers, uninterruptible power supplies, cameras and lasers [83]. Thin dielectric films are used in microelectronic and optoelectronic devices to provide electronic isolation and protection against the environment [84]. Some dielectric materials such as Zinc Oxide exhibit the piezoelectric effect [85], converting mechanical stress or pressure into electrical voltage and vice versa. These materials are used in sensors, actuators and ultrasound transducers typically employed in the medical industry [86]. Silicon-based dielectrics are the most common semiconductor material in solar cells, representing approximately 95% of all the modules sold [87]. Such dielectric materials can be used as encapsulating layers in solar cells to enhance light absorption, reduce reflection, and protect the active materials from environmental degradation [88].

Knowledge of the spin susceptibility provides a critical characterisation for the response of a material to an external magnetic field. Magnetic storage devices such as hard drives and magnetic tapes utilise magnetism to store and retrieve digital information [89]. A hard drive consists of one or more platters coated with a thin layer of magnetic material such as Iron or a Cobalt-based alloy [90]. The platter surface is segmented into regions known as magnetic domains, where each domain can be magnetised to signify a binary 0 or 1 of digital data. To write data, a magnetic write head positioned above the platter generates a magnetic field. This field aligns the magnetic domains on the platter, encoding the desired information. To read data, a magnetic read head detects the changes in magnetic fields as it moves over the spinning platter. The variations in the magnetic field correspond to the stored binary data, allowing the read head to retrieve the information. Magnetic tapes also use the same mechanism, to which the change in the system response to a magnetic field is used to encode digital data. Spintronics is a field dedicated to utilising the spin of electrons in order to develop new devices [91]. Magnetic Random Access Memory is a non-volatile memory technology, which means it retains data even when power is turned off. This memory employs an emerging technique, spin-transfer torque, using spin-polarised electrons to modify the orientation of a magnetic layer which in turn can be used to read/write binary data [92]. Navigation systems, biomedical devices and medical field imaging all require the use of spin sensors for detecting magnetic fields [93].

1.6 Thesis Outline

This thesis is concerned with the development of Density Functional Perturbation Theory (DFPT) in CASTEP to calculate the frequency-dependent dielectric and spin response. The implementation will make use of the Sternheimer scheme and is applied to semiconductor

systems for the case of the dielectric response and transition metals for the response to a perturbative spin-polarised external field.

The work described in this thesis is organised as follows:

1.6.1 Chapter 2

The many-body Schrödinger equation is introduced. The formulation developed by Hohenberg, Kohn and Sham is presented as a means to reduce the many-body problem into the single-particle self-consistent method of Density Functional Theory. An extension to time-dependent DFT is made, with a discussion of the relevant theorem developed by Runge and Gross. The Sternheimer equation, which is the central equation of this thesis is derived and involves a perturbative treatment of the Kohn-Sham equations. The electronic structure code of CASTEP is presented along with a practical discussion on computing the ground-state.

1.6.2 Chapter 3

This chapter aims to provide the reader with a background into the origin of quantities involved in the dielectric response. To this effect, the *GW* method is introduced. Quantities such as the non-interacting Green's function and the Dynamical Screening are discussed. It is shown that these make up the non-interacting density response function, after which taking into account frequency dependence, yields the dielectric matrix. Since the form of the density response function shown here involves an implicit sum over electronic states, a connection is made with sum-over-states perturbation theory and the Sternheimer scheme. Numerical methods are identified, most notably the BiConjugate Gradient Stabilised Scheme which is implemented for both dielectric and spin response computations.

1.6.3 Chapter 4

A series of density functional perturbation computations of the dielectric response is presented. The dielectric spectra of Silicon, Gallium Arsenide, Zinc Oxide and Perovskite Methylammonium Lead Triiodide are illustrated, along with experimental spectroscopic ellipsometry data. Such calculations require attention to the choice of computational parameters used in the CASTEP code package. The choice of the numerical method is substantiated by comparing the convergence behaviour of the BiConjugate Gradient method to that of the BiConjugate Gradient Stabilised scheme.

1.6.4 Chapter 5

In this chapter, the response to an external spin polarised potential is considered. The self-consistent Sternheimer scheme is developed to compute the susceptibility from a collinear magnetic ground-state. The importance of exchange-correlation which is a constituent of the Kohn Sham potential is highlighted. Spectra of the induced magnetisation are illustrated for the transition metal systems of body-centred cubic Iron and face-centred cubic Nickel.

1.6.5 Chapter 6

A summary of work completed to date is provided. Conclusions and perspectives are presented, along with suggestions for further work and investigations.

Chapter 2

Theory

The solution of the time-dependent Schrödinger is prohibitively expensive, there has been significant development and implementations of various approximations to solve the equations for a many-body system of interacting electrons and nuclei. The first which will be discussed is known as the *Born-Oppenheimer approximation* (BO) [94], which posits that the dynamics of the electrons can be decoupled with respect to the nuclei as electrons are orders of magnitude lighter. This means that the nuclei can be regarded as fixed and that we can express a wave function in terms of the electron and nuclear positions. Atomic units are used throughout this thesis ($\hbar = e = 1$). The many-body Schrödinger equation is

$$\hat{H}\psi(\boldsymbol{r}_i, \boldsymbol{R}_I) = E\psi(\boldsymbol{r}_i, \boldsymbol{R}_I), \tag{2.1}$$

where $\hat{H}$ is the Hamiltonian operator, E is the total ground-state energy of the system, $\boldsymbol{r}_i$ are the electron coordinates and $\boldsymbol{R}_I$ are the nuclei coordinates. The Hamiltonian operator contains a sum of kinetic energy and potential operators. The terms of the Hamiltonian, in order, correspond to the kinetic energy of the nuclei and electrons as well as the potential energy operators associated with nuclei-nuclei, electron-electron and nuclei-electron interaction. This is expressed as

$$\hat{H} = \hat{T}_N + \hat{T}_e + \hat{V}_{NN} + \hat{V}_{ee} + \hat{V}_{Ne}, \tag{2.2}$$

where the kinetic energy operators are

$$\hat{T} = \hat{T}_e + \hat{T}_N = -\sum_i \frac{1}{2m_i}\nabla_i^2 - \sum_I \frac{1}{2M_I}\nabla_I^2, \tag{2.3}$$

where m_i, M_I are the masses of the electron and nuclei respectively. The BO approximation allows one to neglect the kinetic energy T_N since it is smaller than T_e by a factor of M_I/m_i which is of order $\sim 10^3 - 10^5$ and their position is fixed. The potential energy operators include the Coulomb interactions between electrons and nuclei, with Z_I, Z_J referring to the nuclear charges:

$$\hat{V} = \hat{V}_{NN} + \hat{V}_{ee} + \hat{V}_{Ne} = \frac{1}{2}\sum_{I\neq J}\frac{Z_I Z_J}{|\boldsymbol{R}_I - \boldsymbol{R}_J|} + \frac{1}{2}\sum_{i\neq j}\frac{1}{|\boldsymbol{r}_i - \boldsymbol{r}_j|} - \sum_{i,I}\frac{Z_I}{|\boldsymbol{r}_i - \boldsymbol{R}_I|}. \tag{2.4}$$

Since the nuclear positions are well-defined, V_{NN} is instead added as constant to the eigenvalue equation. The many-body Hamiltonian under the BO approximation reduces to

$$H = -\sum_i \frac{1}{2m_i}\nabla_i^2 - \sum_{i,I}\frac{Z_I}{|\boldsymbol{r}_i - \boldsymbol{R}_I|} + \frac{1}{2}\sum_{i\neq j}\frac{1}{|\boldsymbol{r}_i - \boldsymbol{r}_j|}, \tag{2.5}$$

where the nuclei-nuclei interaction energy would have to be added to yield the total energy of the system. All of this is to obtain the many-body wavefunction which should provide all the information about the system in question. A popular implementation will now be discussed which aims to obtain the many-body wavefunction via a method which is computationally feasible.

2.1 Density Functional Theory

2.1.1 Hohenberg-Kohn Theorems

The basis of the theoretical framework regarding DFT naturally begins with the discussion of the Hohenberg-Kohn theorems [19]. The theorems state:

1. The external potential is a unique functional of the electronic density in the ground-state $n(\boldsymbol{r})$. As a consequence, all properties of the system are functionals of the ground-state density.

2. The total energy ($E[n]$) of an electronic system has a minimum equal to the ground-state energy at the exact ground-state density.

Hohenberg and Kohn (H-K) defined a universal functional $F[n]$ which includes all electronic energy, that is the kinetic energy (T) and potential energy from electron-electron interaction

(V_{ee}). The Born-Oppenheimer approximation allows one to neglect the nuclei kinetic energy and consider only a static (external) nuclear potential. From the first theorem above, this universal functional along with its constituents is a functional of the density:

$$F[n(\boldsymbol{r})] = T[n] + V_{ee}[n]. \tag{2.6}$$

For a given external potential $v_{ext}(\boldsymbol{r})$, the energy functional $E[n]$ is

$$E[n] = F[n] + \int v_{ext}(\boldsymbol{r}) n(\boldsymbol{r}) d\boldsymbol{r}. \tag{2.7}$$

The exact density dependence of this universal functional is not known. From the second H-K theorem, the minimum of the energy functional is found at the exact ground-state density ($n = n_{\mathrm{GS}}$):

$$\frac{\delta F}{\delta n(\boldsymbol{r})} = -v_{ext}(\boldsymbol{r}). \tag{2.8}$$

Though the H-K theorems are able to prove that this universal functional exists, for realistic systems, there remains no practical method of determining what this functional is, nor how to obtain the ground-state density [9].

2.1.2 The Kohn-Sham method

The Kohn-Sham (KS) equations provide a practical implementation of the H-K theorems [20, 23]. The method is to take the many-body interacting particle picture and instead, impose a non-interacting, fictitious potential to describe the electrons. As long as this potential produces the same ground-state density as compared to the many-body picture, then by the first H-K theorem, all properties of the interacting system are now accessible. Kohn-Sham proposed the following for the universal functional:

$$F[n] = T_0[n] + E_H[n] + E_{xc}[n], \tag{2.9}$$

where $T_0[n]$ is the kinetic energy of the system of non-interacting electrons, $E_H[n]$ is the Hartree energy functional:

$$E_H[n] = \frac{1}{2}\int\int \frac{n(\boldsymbol{r})n(\boldsymbol{r'})}{|\boldsymbol{r}-\boldsymbol{r'}|}d\boldsymbol{r}d\boldsymbol{r'}. \tag{2.10}$$

$E_{\mathrm{xc}}[n]$ is the exchange-correlation (XC) functional and factors in the remainder of the total kinetic energy not included in $T_0[n]$. The functional derivative of an energy functional is the potential [9, 15]. Taking the functional derivative of all terms, the minimisation problem presented in equation (2.8) is now expressed:

$$\frac{\delta T_0[n]}{\delta n(\boldsymbol{r})} = -v_H - v_{xc} - v_{ext}. \tag{2.11}$$

Now consider the following functional:

$$E_{\mathrm{KS}}[n] = T_0[n] + \int n(\boldsymbol{r})v_{\mathrm{KS}}(\boldsymbol{r})d\boldsymbol{r}, \tag{2.12}$$

where,

$$v_{\mathrm{KS}}(\boldsymbol{r}) = v_{\mathrm{H}}(\boldsymbol{r}) + v_{\mathrm{xc}}(\boldsymbol{r}) + v_{ext}(\boldsymbol{r}). \tag{2.13}$$

Equation (2.12) is a functional of a system of non-interacting electrons with respect to a fixed, potential $v_{\mathrm{KS}}(\boldsymbol{r})$, denoted as the KS potential. The minimisation of the energy functional $E_{\mathrm{KS}}[n]$ is equivalent to the minimisation of the universal functional in equation (2.11). The KS potential is an effective potential, experienced by all electrons. The single-particle equation is

$$\left[-\frac{1}{2}\nabla_i^2 + v_{\mathrm{KS}}(\boldsymbol{r}) - \varepsilon_i\right]\phi_i(\boldsymbol{r}) = 0. \tag{2.14}$$

This is equivalent to the Schrödinger equation but with the KS potential instead of the external potential. Note that the KS ground-state orbitals (ϕ_i) and eigenvalues (ε_i) are mathematical formulations. Whilst the KS electron density is connected to the interacting system [15], the validity of directly taking the KS eigenvalues to model physical properties such as the bandgap will be discussed. The KS potential relies upon the electronic density, which, in the KS method is dependent on the single-particle states as shown by equation (2.15). These dependencies necessitate that the KS scheme is solved in a self-consistent manner. The summation of Kohn-Sham orbitals run over the occupied states:

$$n(\boldsymbol{r}) = \sum_{i}^{\text{occ}} |\phi_i(\boldsymbol{r})|^2. \tag{2.15}$$

In practice, the determination of the self-consistent ground-state electronic density is an iterative process. An initial density is constructed in which the KS potential can then be calculated. Through the solution of equation (2.14) and then with equation (2.15), a new electron density is calculated. The energy associated with the initial and new densities are compared and if sufficiently similar, the ground-state density is found. If not, then the iterative process continues in minimising the energy functional. An alternative formulation of the KS scheme of equation (2.15) is to minimise the functional [95]:

$$E[n] = 2\sum_{i}^{\text{occ}} \varepsilon_i - \frac{1}{2}\int\int \frac{n(\boldsymbol{r})n(\boldsymbol{r}')}{|\boldsymbol{r}-\boldsymbol{r}'|} d\boldsymbol{r}d\boldsymbol{r}' - \int v_{xc}(\boldsymbol{r})n(\boldsymbol{r})d\boldsymbol{r} + \tilde{E}_{xc}[n], \tag{2.16}$$

where $\tilde{E}_{\text{xc}}[n]$ includes the exchange-correlation kinetic energy. The summation over eigenvalues considers the spin degeneracy, hence the factor of two.

2.1.3 Spin Density Functional Theory

Until now, the prevailing assumption regarding electron spin has been that the expression for two electrons occupying a spatial orbital is the same. Thus, the Kohn-Sham states feature a spin-degeneracy and it is sufficient to solve the Kohn-Sham equations for only one of the spins. However, the magnetic behaviour of solid-state systems such as transition metals is not captured by this approach, requiring one to treat the spin of electrons separately [96]. This section will present the work of von Barth, Hedin, Rajagopal and Callaway who originally formulated the development of spin-DFT [26, 97]. The wavefunction is now composed of two-component spinors which require a 2×2 size Hamiltonian. The spinor wavefunctions, $|\phi\rangle$, are projected onto an orthonormal spin basis of $|\alpha\rangle$ and $|\beta\rangle$. These spin indices run over the electron $|\uparrow\rangle$ and $|\downarrow\rangle$ states, note that an implicit sum over electronic states is assumed here:

$$n_{\alpha\beta}(\boldsymbol{r}) = \frac{1}{2}\left[n(\boldsymbol{r})\delta_{\alpha\beta} + \boldsymbol{m}(\boldsymbol{r})\boldsymbol{\sigma}\right]. \tag{2.17}$$

For a complete description of the state of an itinerant magnetic system, the spin (magnetisation) density, as well as the charge density, is required. The charge density is given by

$$n(\boldsymbol{r}) = \sum_{\alpha\beta} \langle \phi_{\alpha\beta}(\boldsymbol{r}) | \, \delta_{\alpha\beta} \, | \phi_{\alpha\beta}(\boldsymbol{r}) \rangle \, . \tag{2.18}$$

Along with the vector magnetisation density which is nonzero for the magnetic case:

$$\boldsymbol{m}(\boldsymbol{r}) = \sum_{\alpha\beta} \langle \phi_{\alpha\beta}(\boldsymbol{r}) | \, \boldsymbol{\sigma} \, | \phi_{\alpha\beta}(\boldsymbol{r}) \rangle \, , \tag{2.19}$$

where the Pauli spin matrices are used to define the three components $\boldsymbol{m} = (m_x, m_y, m_z)$ of the magnetisation vector.

$$\sigma_x = \begin{pmatrix} 0 & 1 \\ 1 & 0 \end{pmatrix}, \qquad \sigma_y = \begin{pmatrix} 0 & -i \\ i & 0 \end{pmatrix}, \qquad \sigma_z = \begin{pmatrix} 1 & 0 \\ 0 & -1 \end{pmatrix}. \tag{2.20}$$

The kinetic energy, external potential and Coulomb operators of the Hamiltonian have the following form:

$$T_{\alpha\beta} = -\delta_{\alpha\beta} \sum_{i=1}^{N} \nabla_i^2, \tag{2.21}$$

$$V_{\alpha\beta} = \sum_{i=1}^{N} v_{\alpha\beta}^{ext}(\boldsymbol{r}_i), \tag{2.22}$$

$$U_{\alpha\beta} = \sum_{i=j=1, i\neq j} \frac{\delta_{\alpha\beta}}{|\boldsymbol{r}_i - \boldsymbol{r}_j|}. \tag{2.23}$$

Other than the external potential, this is formally equivalent to non-spin inclusive DFT. A redefinition of equation (2.7) is required to include operators that yield spin components of the density matrix ($\tilde{n}$) with elements $n_{\alpha\beta}$:

$$E[\tilde{n}] = F[\tilde{n}] + V[\tilde{n}], \tag{2.24}$$

where,

$$F[\tilde{n}] = T[\tilde{n}] + \int\int \frac{n(\boldsymbol{r}) n(\boldsymbol{r}')}{|\boldsymbol{r} - \boldsymbol{r}'|} d\boldsymbol{r} d\boldsymbol{r}' + E_{xc}[\tilde{n}], \tag{2.25}$$

and,

$$V[\tilde{n}] = \sum_{\alpha\beta} \int v^{ext}_{\alpha\beta}(\boldsymbol{r}) n_{\alpha\beta}(\boldsymbol{r}) d\boldsymbol{r}. \tag{2.26}$$

The density matrix elements can be further simplified if single-particle wavefunctions ($\phi_{i\alpha}$) are used, this holds for the associated eigenvalues which lie below the Fermi energy E_F:

$$n_{\alpha\beta}(\boldsymbol{r}) = \sum_{\substack{i=1, \\ \varepsilon_{i\alpha}\varepsilon_{i\beta} \leq E_F}}^{N} \phi_{i\alpha}(\boldsymbol{r}) \phi^*_{i\beta}(\boldsymbol{r}). \tag{2.27}$$

The spin-KS equation is postulated:

$$\sum_{\beta} \left(-\delta_{\alpha\beta} \nabla^2 + v^{\mathrm{KS}}_{\alpha\beta}(\boldsymbol{r}) - \varepsilon_i \delta_{\alpha\beta} \right) \phi_{i\beta}(\boldsymbol{r}) = 0. \tag{2.28}$$

From this, the kinetic energy is written as

$$T_0[\tilde{n}] = \sum_{i=1}^{N} \varepsilon_i - \sum_{\alpha\beta} \int v^{\mathrm{KS}}_{\alpha\beta}(\boldsymbol{r}) n_{\alpha\beta}(\boldsymbol{r}) d\boldsymbol{r}. \tag{2.29}$$

The variational principle from H-K sets the condition:

$$\frac{\delta E[\tilde{n}]}{\delta \tilde{n}_{\alpha\beta}(\boldsymbol{r})} = 0. \tag{2.30}$$

Which yields the KS potential:

$$v^{\mathrm{KS}}_{\alpha\beta}(\boldsymbol{r}) = v^{ext}_{\alpha\beta}(\boldsymbol{r}) + 2\delta_{\alpha\beta} \int \frac{n(\boldsymbol{r}')}{|\boldsymbol{r} - \boldsymbol{r}'|} d\boldsymbol{r}' + v^{xc}_{\alpha\beta}(\boldsymbol{r}), \tag{2.31}$$

where,

$$v^{xc}_{\alpha\beta}(\boldsymbol{r}) = \frac{\delta}{\delta \tilde{n}_{\alpha\beta}(\boldsymbol{r})} \left(E_{xc}[\tilde{n}] + T_{xc}[\tilde{n}] \right). \tag{2.32}$$

Equations (2.28), (2.31) and (2.32) form the spin-dependent KS equations which are coupled and thus require self-consistent treatment. The total energy functional is reformed in a similar manner to that of equation (2.16):

$$E[\tilde{n}] = \sum_{\substack{i=1,\\ \varepsilon_i \leq E_F}}^{N} \varepsilon_i - \int\int \frac{n(\boldsymbol{r})n(\boldsymbol{r}')}{|\boldsymbol{r}-\boldsymbol{r}'|} d\boldsymbol{r}d\boldsymbol{r}' - \sum_{\alpha\beta}\int v^{xc}_{\alpha\beta}(\boldsymbol{r})n_{\alpha\beta}(\boldsymbol{r})d\boldsymbol{r} + E_{xc}[\tilde{n}], \tag{2.33}$$

where the notable differences are the α and β indices which run over the electron spin states.

2.1.4 Exchange-Correlation (XC)

The first term of equation (2.13) is the Hartree term and takes into account electrostatic interactions. The external potential is not a functional of the electronic density and will be discussed later. The exact form of the exchange-correlation potential is not known and in practice, approximate functionals are used which are based on the electronic density. One of the simplest is known as the *local density approximation* (LDA) [23], it assumes that the exchange-correlation energy at a point $\boldsymbol{r}$ is equivalent to the exchange-correlation energy of a homogeneous electron gas which has the same density at point $\boldsymbol{r}$:

$$E^{\mathrm{LDA}}_{xc}[n(\boldsymbol{r})] = \int n(\boldsymbol{r})\varepsilon_{xc}(n(\boldsymbol{r}))d\boldsymbol{r}, \tag{2.34}$$

where ε_{xc}, the exchange-correlation energy is a function of the density and is only local. The exchange-correlation potential may be written as

$$v_{xc}(\boldsymbol{r}) = \frac{\delta E_{xc}[n(\boldsymbol{r})]}{\delta n(\boldsymbol{r})}. \tag{2.35}$$

The assumption made in the LDA means that inhomogeneities in the electron density are ignored. However, it is able to capture several electronic structure properties such as lattice constants, cohesive energies and bandgaps [98, 99, 100]. The accuracy to which the electronic bandgap can be captured using the LDA will be highlighted in due course. For spin-polarised systems, exchange and correlation of the homogeneous spin-polarised electron gas is utilised. This is known as the *local spin density approximation* and will be further discussed in a later section regarding longitudinal response.

Another common approximation often employed is the generalised gradient approximation (GGA) [99, 101]. This is a semi-local functional which incorporates the effect of inhomogeneities by including the gradient of the electron density in addition to the density. There

are many forms of this functional; the Perdew, Burke and Ernzerhof (PBE) [102] is employed in this work:

$$E_{xc}^{\mathrm{GGA}}[n(\boldsymbol{r})] = \int n(\boldsymbol{r})\varepsilon_{xc}(n(\boldsymbol{r}),\nabla n(\boldsymbol{r}))d\boldsymbol{r}. \tag{2.36}$$

Both of these functionals are attempts to fit a functional that is exact in the Kohn Sham formulation of (2.9) and no tuning parameters are used.

2.2 Time Dependent Density Functional Theory

Until now the time-dependence regarding DFT has not been discussed. The H-K theorems stated before allow for the connection of the ground-state electronic density to the properties of a system. That is, all properties of a system are functionals of the electronic density. However, does this apply to the time-dependent case? The Runge-Gross and Van Leeuwen theorems provide the basis for this.

2.2.1 Runge-Gross Theorem

Consider a time-dependent Hamiltonian,

$$\hat{H}(t) = \hat{T} + \hat{V}_{ee} + \hat{V}_{ext}. \tag{2.37}$$

Runge and Gross [68] proved that there is a 1-1 mapping:

$$n(\boldsymbol{r},t) \overset{\Psi_0}{\longleftrightarrow} v_{ext}(\boldsymbol{r},t). \tag{2.38}$$

This is in essence, a similar result to the first H-K theorem. The densities $n(\boldsymbol{r},t)$ and $n'(\boldsymbol{r},t)$ evolving with $\hat{H}(t)$ from a common initial state Ψ_0 are *necessarily different*. This is true provided that the two local (now time-dependent) potentials $v_{ext}(\boldsymbol{r},t)$ and $v'_{ext}(\boldsymbol{r},t)$ which are expandable in a Taylor series about the initial time t_0 satisfy the following:

$$v_{ext}(\boldsymbol{r},t) \neq v'_{ext}(\boldsymbol{r},t) + c(t). \tag{2.39}$$

Later, a generalisation of this theorem was proved by van Leeuwen [61, 103]. By extension of Runge-Gross, it holds that this 1-1 mapping exists for both fully interacting systems and for non-interacting particles. Therefore, there are two unique potentials that correspond to a given time-dependent density $n(\boldsymbol{r},t)$. One potential $v_{ext}[n,\Psi_0](\boldsymbol{r},t)$ propagates the interacting time-dependent Schrödinger equation with an initial state Ψ_0 and another potential $v_{\mathrm{KS}}[n,\Phi_0](\boldsymbol{r},t)$ which yields the same density by propagating the *non-interacting* time-dependent Schrödinger with initial state Φ_0.

$$v_{ext}[n,\Psi_0](\boldsymbol{r},t) \longleftrightarrow n(\boldsymbol{r},t) \longleftrightarrow v_{\mathrm{KS}}[n,\Phi_0](\boldsymbol{r},t). \tag{2.40}$$

The time-dependent KS system of equations can now be introduced, where again it is stressed that the density on the ground-state $n(\boldsymbol{r})$ given by the KS wavefunction is assumed to be the same as the one given by the interacting (true) wave function.

$$i\frac{\partial}{\partial t}\phi_i(\boldsymbol{r},t) = \left[-\frac{1}{2}\nabla^2 + v_{\mathrm{KS}}(\boldsymbol{r},t)\right]\phi_i(\boldsymbol{r},t). \tag{2.41}$$

With the time-dependent electronic density:

$$n(\boldsymbol{r},t) = \sum_{i}^{\mathrm{occ}} |\phi_i(\boldsymbol{r},t)|^2. \tag{2.42}$$

It is now understood that this 1-1 mapping is only possible if the exact local potential $v_{\mathrm{KS}}(\boldsymbol{r},t)$ is known. However, similar to determining the stationary ground-state density, there is no recipe for building a potential which is exact in principle. There is a self-consistent dependency of the KS (effective) potential on the density which in itself, depends on the initial state calculated through equation (2.42).

$$v_{\mathrm{KS}}[n](\boldsymbol{r},t) = v_H[n](\boldsymbol{r},t) + v_{xc}[n](\boldsymbol{r},t) + v_{ext}(\boldsymbol{r},t). \tag{2.43}$$

In practice again this is an iterative process in which for the first iteration, the initial orbitals which are used to compute the stationary ground-state density are now reused. The time-dependent KS equations are solved self-consistently using an approximate KS potential.

2.2.2 Time Dependent Exchange-Correlation

In ordinary DFT, the XC potential is normally written as a functional derivative of the XC energy. However, it is not straightforward to extend this formulation to the time-dependent case [104]. The XC functional at time t' is a functional of the electronic density at time t and it is necessary that $t' \geq t$. The contrary would otherwise violate causality. One of the earliest works to include time-dependence in XC was Ullrich *et al* who proposed a time-dependent optimised effective potential to explicitly determine the time evolution of the system in response to an external potential [105]. Later, Dobson *et al* proposed an alternative form of the XC potential which contained memory of the electronic density at previous times [106].

The linear response work of this thesis will exclusively employ the *adiabatic local density approximation* (ALDA) [103]. The exchange-correlation functional is taken to be the derivative of the ground-state energy functional evaluated at an instantaneous density.

$$v_{xc}^{\mathrm{ALDA}}(\boldsymbol{r},t) = \left.\frac{\delta E_{xc}^{\mathrm{LDA}}}{\delta n(\boldsymbol{r},t)}\right|_{(n(\boldsymbol{r},\boldsymbol{t})=n(\boldsymbol{r}))}. \tag{2.44}$$

This procedure is computationally simple and allows for the use of existing functionals (LDA, PBE) employed for ground-state DFT. The approximation made here is that the construction of the functional is *local* in time. In principle, this should be adequate to describe the time-dependency in systems close to equilibrium [104].

2.2.3 Formulation of the Sternheimer Equation

The central equation of this thesis is the Sternheimer equation, here it is formulated in a general manner using perturbation theory up to linear order. The time-independent Schrödinger equation is

$$\hat{H}\,|\psi_n\rangle = \varepsilon_n\,|\psi_n\rangle\,, \tag{2.45}$$

where $\hat{H}$ is the unperturbed Hamiltonian, ψ and ε refer to the quantum mechanical wavefunction and its corresponding energy eigenvalue. The parameterisation in $\boldsymbol{r}$ is dropped for convenience and the subscript n runs over the electron states. The quantities in (2.45) are perturbed to first-order by adding a linear term:

$$\hat{H}(\lambda)\,|\psi_n(\lambda)\rangle = \varepsilon_n(\lambda)\,|\psi_n(\lambda)\rangle\,, \tag{2.46}$$

with,

$$\hat{H}(\lambda) = \hat{H} + \lambda \hat{H}^{(1)}, \tag{2.47}$$

$$\psi_n(\lambda) = \psi_n + \lambda \psi_n^{(1)}, \tag{2.48}$$

$$\varepsilon_n(\lambda) = \varepsilon_n + \lambda \varepsilon_n^{(1)}. \tag{2.49}$$

Inserting the linear perturbation in (2.47), (2.48) and (2.49) into equation (2.46) yields:

$$(\hat{H} + \lambda \hat{H}^{(1)}) \, |\psi_n + \lambda \psi_n^{(1)}\rangle = (\varepsilon_n + \lambda \varepsilon_n^{(1)}) \, |\psi_n + \lambda \psi_n^{(1)}\rangle \, . \tag{2.50}$$

Expanding:

$$\begin{aligned} \hat{H} \, |\psi_n\rangle + \lambda \hat{H} \, |\psi_n^{(1)}\rangle + \lambda \hat{H}^{(1)} \, |\psi_n\rangle + \lambda^2 \hat{H}^{(1)} \, |\psi_n\rangle \\ = \varepsilon_n \, |\psi_n\rangle + \lambda \varepsilon_n \, |\psi_n^{(1)}\rangle + \lambda \varepsilon_n^{(1)} \, |\psi_n\rangle + \lambda^2 \varepsilon_n^{(1)} \, |\psi_n^{(1)}\rangle \, . \end{aligned} \tag{2.51}$$

Terms which are quadratic in λ are neglected and therefore only the linear response of the system is considered. What is left is the original unperturbed equation and terms linear in λ which are:

$$\hat{H} \, |\psi_n^{(1)}\rangle + \hat{H}^{(1)} \, |\psi_n\rangle = \varepsilon_n \, |\psi_n^{(1)}\rangle + \varepsilon_n^{(1)} \, |\psi_n\rangle \, . \tag{2.52}$$

Factoring out the wavefunctions,

$$(\hat{H} - \varepsilon_n) \, |\psi_n^{(1)}\rangle = -(\hat{H}^{(1)} - \varepsilon_n^{(1)}) \, |\psi_n\rangle \, . \tag{2.53}$$

At this point the right-hand side of equation (2.53) is considered and the following operators are introduced:

$$\hat{P}_{occ} = \sum_{n \in occ} |\psi_n\rangle \langle \psi_n| \, , \tag{2.54}$$

$$\hat{P}_{unocc} = \sum_{n \in unocc} |\psi_n\rangle \langle \psi_n| , \tag{2.55}$$

where $\hat{P}_{occ}$ is a projection operator over occupied states and $\hat{P}_{unocc}$ is over unoccupied states. These operators obey the condition of

$$1 = \hat{P}_{occ} + \hat{P}_{unocc}. \tag{2.56}$$

Due to the orthonormality condition imposed on the zeroth-order wavefunctions:

$$\langle \psi_n | \psi_m \rangle = \delta_{nm}. \tag{2.57}$$

The parallel-transport gauge [107] imposes an orthonormalisation with respect to first-order wavefunctions and yields that

$$\langle \psi_n | \psi_m^{(1)} \rangle = 0. \tag{2.58}$$

Applying $\left(-\hat{P}_{unocc}\right)$ onto $\hat{H}^{(1)} |\psi_m\rangle$:

$$(-1 + \hat{P}_{occ})\hat{H}^{(1)} |\psi_m\rangle = -\hat{H}^{(1)} |\psi_m\rangle + \sum_{n \in occ} |\psi_n\rangle \langle \psi_n| \hat{H}^{(1)} |\psi_m\rangle . \tag{2.59}$$

It can be shown that the summation term on the right-hand side refers to the first-order eigenvalues by the closure relation. To show this, the factored perturbed Schrodinger equation (2.53) is multiplied through by $\langle \psi_m|$:

$$(\langle \psi_m|)(\hat{H} - \varepsilon_n) |\psi_n^{(1)}\rangle = (\langle \psi_m|)(-\hat{H}^{(1)} + \varepsilon_n^{(1)}) |\psi_n\rangle . \tag{2.60}$$

From the gauge-freedom of the first-order wavefunction using condition (2.58), the left-hand side of equation (2.60) is zero, simplifying the right:

$$0 = -\langle \psi_m| \hat{H}^{(1)} |\psi_m\rangle + \varepsilon_n^{(1)} \langle \psi_n | \psi_m \rangle , \tag{2.61}$$

and using the orthonormalisation condition in (2.57):

$$\varepsilon_n^{(1)} = \langle \psi_n| \hat{H}^{(1)} |\psi_n\rangle . \tag{2.62}$$

The first-order eigenvalues are placed instead of the summation term on the right-hand side of equation (2.59) which is now given as

$$(-1+\hat{P}_{occ})\hat{H}^{(1)}\,|\psi_m\rangle = -\hat{H}^{(1)}\,|\psi_m\rangle + \sum_{n\in occ}\varepsilon_m^{(1)}\,|\psi_n\rangle\,\delta_{nm}. \tag{2.63}$$

Simplifying:

$$(-1+\hat{P}_{occ})\hat{H}^{(1)}\,|\psi_n\rangle = -(\hat{H}^{(1)}-\varepsilon_n^{(1)})\,|\psi_n\rangle\,, \tag{2.64}$$

where the right-hand side of equation (2.53) has been formulated. Now it is asserted that $\hat{H}^{(1)} = \hat{V}_{\text{ext}}$:

$$(\hat{H}-\varepsilon_n)\,|\psi_n^{(1)}\rangle = (-1+\hat{P}_{occ})\hat{V}_{\text{ext}}\,|\psi_n\rangle\,. \tag{2.65}$$

In order to account for time-dependent perturbations, the following ansatz is proposed [108]:

$$\psi_n^{(1)}(\boldsymbol{r}) \rightarrow e^{\pm i\omega t}\,\psi_n^{(1)}(\boldsymbol{r},\pm\omega), \tag{2.66}$$

$$\hat{V}_{ext} \rightarrow \hat{V}_{ext}(\boldsymbol{r},\pm\omega). \tag{2.67}$$

Now if the equation is time-dependent:

$$i\frac{\partial\psi_n}{\partial t} = \hat{H}\psi_n. \tag{2.68}$$

The Sternheimer method which was initially developed to compute polarisabilities [64] can now be formulated:

$$(\hat{H}-\varepsilon_n\pm\omega)\,|\psi_n^{(1)}(\boldsymbol{r},\pm\omega)\rangle = -(1-\hat{P}_{occ})\hat{V}_{ext}(\boldsymbol{r},\pm\omega)\,|\psi_n(\boldsymbol{r})\rangle\,. \tag{2.69}$$

The exact form of the wavefunction has been kept ambiguous, in practice the wavefunctions here correspond to KS states in which a plane-wave basis set is utilised. The property of orthonormality is required, which plane waves possess [109]. In addition to this, an adequate description of both occupied and (some) unoccupied states is needed to properly define the projection operators, with a suitable choice of basis set parameters this can be accomplished.

Whilst all of the above concerns the development of applying linear perturbation theory to the true (interacting) many-body wavefunction. The same treatment holds for the Kohn-Sham system of equations. Providing that an accurate ground-state density can be determined, all the theorems previously discussed allow for a perturbative treatment of DFT [110]. This approach is aptly named *Density Functional Perturbation Theory* and this thesis aims to present implementations of computing response functions with this approach.

2.3 The CASTEP package

The development of DFPT techniques in this thesis will be carried out in the CASTEP package. The (CA)mbridge (S)erial (T)otal (E)nergy (P)ackage was originally programmed in FORTRAN 77 and has since then been completely redesigned using modern FORTRAN [111]. The package makes use of efficient implementations of Linear Algebra [29] and Fast Fourier Transform libraries [41]. It can be run in parallel with systematic data distribution through a number of schemes [112, 113]. Whilst this section will introduce the theories employed in CASTEP, these are relevant to other DFT packages such as Quantum ESPRESSO and ABINIT [114, 115].

2.3.1 Bloch's Theorem and Plane Waves

The KS method previously discussed is an approach to solving the many-body electron problem of quantum mechanics. A set of single-particle equations that include the effective KS potential is proposed to describe the correlated nature of electrons. However, the issue still remains that the number of electrons is on the order of 10^{23} per mole of atoms [116]. One can recognise that many condensed matter systems such as crystalline solids are periodic in structure, this periodicity can be exploited to drastically reduce computational cost and render such calculations feasible [9]. It is quite reasonable to argue that a repeating structure of nuclei and electrons in a crystal structure consists of an electronic charge density which is also periodic [9]. If $\boldsymbol{R}$ is one of the real space lattice vectors that define the structure, $\boldsymbol{r}$ is an arbitrary vector in space, then the density has the condition:

$$n(\boldsymbol{r}+\boldsymbol{R}) = n(\boldsymbol{r}). \tag{2.70}$$

This means that the KS orbitals from equation (2.15) satisfy:

$$|\phi_j(\boldsymbol{r}+\boldsymbol{R})|^2 = |\phi_j(\boldsymbol{r})|^2, \tag{2.71}$$

where there is an implicit sum over all unique KS eigenstates, indexed now by j. This implies that

$$\phi_j(\boldsymbol{r}+\boldsymbol{R}) = \boldsymbol{C}\cdot\phi_j(\boldsymbol{r}), \tag{2.72}$$

where $\boldsymbol{C}$ has the condition:

$$|\boldsymbol{C}|^2 = 1. \tag{2.73}$$

The dimensionless quantity $\boldsymbol{C}$ can be expressed as

$$\boldsymbol{C} = e^{i\cdot\boldsymbol{k}\cdot\boldsymbol{R}}, \tag{2.74}$$

where at this point, $\boldsymbol{k}$ is defined to be an arbitrary parameter with dimension proportional to the inverse of space. The expression for $\boldsymbol{C}$ (2.74) meets the condition of (2.73). The KS orbital of equation (2.72) is

$$\phi_j(\boldsymbol{r}+\boldsymbol{R}) = e^{i\cdot\boldsymbol{k}\cdot\boldsymbol{R}}\cdot\phi_j(\boldsymbol{r}). \tag{2.75}$$

Whilst there is no mathematical rigour here in determining the form of $\boldsymbol{C}$, the index $\boldsymbol{k}$ and the form of the KS orbital. It can be shown using symmetry and periodicity of the crystal structure with respect to $\boldsymbol{R}$, that the KS orbitals can be written in the form of (2.75).

Bloch's theorem [116] states that the electronic wavefunction with band index j, subject to a periodic potential may be written as

$$\psi_{j,\boldsymbol{k}}(\boldsymbol{r}) = e^{i\boldsymbol{k}\cdot\boldsymbol{r}}u_j(\boldsymbol{r}). \tag{2.76}$$

The function $u_j(\boldsymbol{r})$ possesses the periodicity of the potential, $u_j(\boldsymbol{r}+\boldsymbol{R}) = u_j(\boldsymbol{r})$, where now $\boldsymbol{R}$ is a vector that spans the length of the smallest possible structure needed to represent the periodic system, *i. e.* the unit cell. The band index is denoted by j to differentiate from the imaginary unit of i present in the exponential. The generalised version of the theorem states that $\boldsymbol{R}$ can correspond to any translation vector of the lattice. The wave vector $\boldsymbol{k}$ will be

discussed in due course. This formulation naturally leads to the choice of a plane-wave basis set to describe the wavefunction within the unit cell. The periodic part of the wavefunction of (2.76) can be expressed in a Fourier series as

$$u_j(\boldsymbol{r}) = \sum_{\boldsymbol{G}} c_{j,\boldsymbol{G}} e^{i\boldsymbol{G}\cdot\boldsymbol{r}}, \tag{2.77}$$

where the $c_{j,\boldsymbol{G}}$ are plane-wave coefficients and $\boldsymbol{G}$ are the reciprocal lattice vectors which satisfy the relation $\boldsymbol{G}\cdot\boldsymbol{R} = 2\pi n$, where n is an integer. The basis set employed by the CASTEP package is to utilise plane waves in order to describe the KS states:

$$\psi_{j,\boldsymbol{k}}(\boldsymbol{r}) = \sum_{\boldsymbol{G}} c_{j,\boldsymbol{k}+\boldsymbol{G}} e^{i(\boldsymbol{k}+\boldsymbol{G})\cdot\boldsymbol{r}}. \tag{2.78}$$

2.3.2 Reciprocal Space Sampling and Basis Set

The quantity $\boldsymbol{k}$ in Bloch's theorem of (2.76) is a component of the arbitrary phase factor and is defined to have a dimension which is inverse to that of the lattice vector. This object $\boldsymbol{k}$ is known as the wave vector and it is useful to consider this as a quantum number characteristic of the translational symmetry present in the periodic potential [116]. That is, every KS state is indexed by its unique crystal momentum proportional to $\hbar\boldsymbol{k}$. Since there is consideration of only the unit cell, the wave vector $\boldsymbol{k}$ can always be confined to the first Brillouin zone (BZ). Any wave vector such as $\boldsymbol{k}'$ that is not in the first BZ can be written as

$$\boldsymbol{k}' = \boldsymbol{k} + \boldsymbol{G}, \tag{2.79}$$

where $\boldsymbol{G}$ is a reciprocal lattice vector and $\boldsymbol{k}$ lies in the 1st BZ. Since $e^{i\boldsymbol{G}\cdot\boldsymbol{R}} = e^{i2\pi n} = 1$ for any $\boldsymbol{G}$, Bloch's theorem holds for $\boldsymbol{k}$ and $\boldsymbol{k}'$. Whilst (2.78) allows one to consider a finite number of electrons present within the unit cell, each KS state now has an infinite number of k-points to occupy [116]. In practice, one only needs to sample reciprocal space since the electronic wavefunction at k-points that are sufficiently close together will be nearly identical [9, 117]. To this aim, a function can be written as an integral over the BZ:

$$\frac{\Omega}{(2\pi)^3}\int_{\mathrm{BZ}} f(\boldsymbol{k})d\boldsymbol{k} = \sum_j w_j F(\boldsymbol{k}_j), \tag{2.80}$$

where Ω is the cell volume, $F(\boldsymbol{k})$ is the Fourier transform of the function integrated over the BZ and w_j are weighting factors [118]. The choice of k-points ($\boldsymbol{k}_j$) used to sample reciprocal space in the CASTEP package was developed by Monkhorst and Pack (MP) [119, 120]. The k-points are linear combinations of three reciprocal lattice vectors ($\boldsymbol{b}_{1\ldots3}$) distributed uniformly through space as [118]:

$$\boldsymbol{k}_j = x_{1j}\boldsymbol{b}_1 + x_{2j}\boldsymbol{b}_2 + x_{3j}\boldsymbol{b}_3, \tag{2.81}$$

where,

$$x_{ij} = \frac{l_i}{n_j}, \tag{2.82}$$

where l_i are the lengths of reciprocal lattice vectors. The number of k-points in the j-th set is denoted by n_j and the index j runs from 1 to n_j. Practically, the MP k-point set is specified by an evenly spaced 3-dimensional grid as an input parameter for the computation with the form $n \times n \times n$, where a larger n results in a finer MP grid as shown in (2.82). The importance of sampling the BZ with the MP grid will be made apparent within the context of linear response calculations. Computational savings can be made by utilising the point group symmetry of the lattice, this will be discussed in due course.

In addition to k-points, (2.78) contains an infinite series with respect to $\boldsymbol{G}$, the reciprocal lattice vector. The Fourier plane-wave coefficients have a kinetic energy proportional to $|\boldsymbol{k}+\boldsymbol{G}|^2$ [45]. For most wavefunctions, there will be a limit to which the states can be described as smoothly varying. This in turn means that the coefficients $c_{j,\boldsymbol{k}+\boldsymbol{G}}$ become small for large $|\boldsymbol{k}+\boldsymbol{G}|$ [117]. Thus, one can truncate the Fourier series in (2.78) by introducing a plane-wave energy cutoff:

$$E_{cut} = \frac{|\boldsymbol{k}+\boldsymbol{G}_{max}|^2}{2}. \tag{2.83}$$

Which fixes the highest reciprocal lattice vector used in the Fourier expansion ($\boldsymbol{G}_{max}$). Any $|\boldsymbol{k}+\boldsymbol{G}|$ vectors which are larger and therefore lie outside the cutoff are not considered. This corresponds to a sphere in reciprocal space and fixes a practical finite basis set.

$$\psi_{j,\boldsymbol{k}}(\boldsymbol{r}) = \sum_{G}^{|\boldsymbol{G}|<\boldsymbol{G}_{max}} c_{j,\boldsymbol{k}+\boldsymbol{G}} e^{i[(\boldsymbol{k}+\boldsymbol{G})\cdot\boldsymbol{r}]}, \tag{2.84}$$

where the limit to the Fourier series becomes $|\boldsymbol{k}+\boldsymbol{G}|^2 \leq E_{cut}$. In a similar fashion to k-point sampling, it will be shown that the accuracy of linear response calculations is dependent on the choice of plane-wave energy cutoff. In practice, one must converge both the k-point MP grid and plane-wave cutoff in efforts to adequately describe the wavefunction and carry out response computations whilst balancing computational resources. The consideration of more k-points and Fourier components would directly result in an increased number of operations.

2.3.3 Optimisations in CASTEP

Leading DFT codes such as the CASTEP package take efforts to reduce computational demand and maintain optimal memory consumption. This section will not be comprehensive in the discussion of the numerous optimisations which comprise the CASTEP DFT package. The interested reader can consult [40, 45, 111, 112, 113, 121, 122] and references therein.

Fourier Transforms

The choice of a plane-wave basis set has an advantage in that only a single parameter (E_{cut}) is required to systematically improve the description of the electronic wavefunction. Expanding the wavefunctions in terms of plane waves using (2.84) into (2.14) gives the KS equations in plane-wave form [45]:

$$\sum_{\boldsymbol{G}'}\left[\frac{1}{2}|\boldsymbol{k}+\boldsymbol{G}|^2\delta_{\boldsymbol{G}\boldsymbol{G}'}+V_{ext}(\boldsymbol{G}-\boldsymbol{G}')+V_{xc}(\boldsymbol{G}-\boldsymbol{G}')+V_H(\boldsymbol{G}-\boldsymbol{G}')\right]\times c_{j,\boldsymbol{k}+\boldsymbol{G}'}=\varepsilon_j c_{j,\boldsymbol{k}+\boldsymbol{G}}. \quad (2.85)$$

The KS Hamiltonian is the left-hand bracketed term of (2.85). This corresponds to a matrix of size $N_{\boldsymbol{G}} \times N_{\boldsymbol{G}}$, where $N_{\boldsymbol{G}}$ is the number of plane waves. The Hamiltonian is not only expensive to construct but impractical to explicitly store its entire array in memory. In the reciprocal space representation, the kinetic energy is shown to be diagonal, whilst the potentials are described in terms of Fourier components and are diagonal in real space. It is therefore optimal to employ both real and reciprocal space grids to compute the aforementioned terms and this can be done for each KS eigenstate indexed by band, k-point and spin (if applicable). The CASTEP package utilises robust, Fast Fourier Transform libraries such as FFTW to compute these transformations between real and reciprocal space [41]. These libraries have

also been developed to be parallel-capable with respect to the electronic band, k-point and plane waves [30]. In particular, k-point parallelism will be exploited in this work, there is no dependency that exists on an eigenstate at one k-point with respect to another eigenstate at a different $\boldsymbol{k}$. Thus one can leverage the power of HPC systems to split up the workload into k-point sets, each of which the Hamiltonian is constructed as needed and applied to a wavefunction [113].

Symmetry for K-Point Reduction

A finer sampling of the Brillouin zone corresponds to a larger MP grid with more k-points included in the set [120]. This discrete set of k-points may be reduced by considering the symmetry of the crystal structure. Thus, one can write the integral over the BZ in (2.80) as

$$\frac{\Omega}{(2\pi)^3}\int_{\mathrm{BZ}} f(\boldsymbol{k})d\boldsymbol{k} = \sum_{j=1}^{P(n_j)\in IBZ} w_j F(\boldsymbol{k}_j), \tag{2.86}$$

where $P(n_j)$ is the number of symmetry-dependent points located in the irreducible wedge of the Brillouin zone (*IBZ*). If two or more k-points in the MP set are related by a symmetry operation, the contribution of these points to the electronic density is identical. These special k-points can be sorted into a set in which a single k-point is chosen and assigned a weight (w_j). This weight is a measure of the number of symmetry-related equivalent k-points that this single k-point represents with respect to the full MP grid. Reducing the full MP grid to this *irreducible* set of nonequivalent weighted k-points allows for the determination of the wavefunction and density using fewer operations, reducing computational expense [112, 113].

2.3.4 Fermi Level

The statistical mechanical approach to defining the Fermi level is to determine the highest occupied state the electron occupies at zero temperature. The electrons will occupy all available energy states, constrained by the Pauli exclusion principle, up to the Fermi energy. The Fermi-Dirac distribution function is written as

$$f_{j,\boldsymbol{k}} = \left[\exp\left(\frac{\varepsilon_{j,\boldsymbol{k}} - \mu}{k_B T}\right) + 1\right]^{-1}, \tag{2.87}$$

where k_B is the Boltzmann constant, T is the temperature, μ is the Fermi level and $\varepsilon_{j,\boldsymbol{k}}$ is the energy of the j-th eigenstate at $\boldsymbol{k}$. Taking the zero temperature limit, the distribution function takes on the form of a step function:

$$\lim_{T\to 0} \; f_{j,\boldsymbol{k}} = \begin{cases} 0 & \text{if } \varepsilon_{j,\boldsymbol{k}} > \mu \\ 1 & \text{if } \varepsilon_{j,\boldsymbol{k}} < \mu. \end{cases} \tag{2.88}$$

Determination of the Fermi level requires knowledge of the ground-state KS orbitals in order to determine the single particle energy eigenvalues. The KS orbitals can be determined upon solving the system of equations in (2.14) which is subject to the KS potential. The KS potential in (2.13) contains terms which involve the functional derivative of the density. The density is constructed of occupied KS states, integrated over reciprocal space:

$$n(\boldsymbol{r}) = \sum_j \int_{\mathrm{BZ}} f_{j,\boldsymbol{k}} |\psi_{j,\boldsymbol{k}}|^2 d\boldsymbol{k}. \tag{2.89}$$

This inter-dependency of terms calls for a process that accounts for electron behaviour and ensures that the electronic density is consistent with the KS wavefunction and vice-versa. The procedure is known as *self-consistency* and the CASTEP package implements this to obtain a ground-state description.

In order to determine the Fermi energy, a trial energy is used to initialise an iterative search. The self-consistent process is used to determine the ground-state and thus the Fermi energy to within a user-defined tolerance. The importance of reciprocal space sampling in constructing the density is shown in equation (2.89). If the sampling of reciprocal space is too coarse to accurately represent the wavefunction, the errors propagate to the ground-state density and KS potential. This work will present graphical representations of energy levels as a function of $\boldsymbol{k}$, this is known as a *band structure* plot. In performing DFT computations, care is taken in the choice of MP grid to sample the BZ and energy cutoff to adequately describe the wavefunction. It is often a balance between the feasibility of the calculation with respect to the level of accuracy required. This work will showcase how the choice of these parameters directly affects the accuracy of response quantities. It is noted here that the Fermi energy computed in this approach corresponds to the highest occupied KS energy value. The validity of using the mathematical construction that is the KS scheme to characterise a system in comparison to experimental data will be highlighted in the discussion of the bandgap.

A finite set of k-points specified by an MP grid is used to discretise the BZ integral of (2.89). By definition, insulating systems have a clear gap between occupied and unoccupied

states. The step function that the Fermi-Dirac distribution takes in (2.88) can handle such systems, defining integer occupation numbers to specify valence (occupied) and conduction (unoccupied) states. For semiconducting systems, the gap in the occupied and unoccupied states is finite, requiring an enhanced sampling of reciprocal space to accurately describe both manifolds. In metallic systems, the occupied bands cross the Fermi level which presents an issue with the use of equation (2.88), with integer occupation numbers. There is now a discontinuity due to fractional occupations which would require a computationally exhaustive set of k-points to describe the electron band dispersion. The integer occupation numbers can be replaced with a function that varies smoothly from 1 to 0 around the Fermi level. The Fermi-Dirac scheme of (2.87) corresponds to a *smearing* scheme that is adjustable by temperature. As the temperature increases, the $T = 0$ step function becomes increasingly smeared allowing for a more gradual transition between the two manifolds. The Fermi-Dirac smearing scheme has a disadvantage due to its long tail present in the occupation probabilities around the Fermi level. This requires the inclusion of many slightly occupied bands above the Fermi level which adds to the computational cost. The response computations developed in this work will employ a different smearing function in an effort to reduce the consideration of extra partially occupied bands.

2.3.5 Pseudopotentials

One of the setbacks of plane-wave basis sets is that it is prohibitively expensive to represent the sharp features of the wavefunction to describe the electrons under the influence of a very strong potential near the nuclei. Conveniently, the core electrons situated close to the nuclei have little contribution to chemical properties and so it is possible to separate the contributions of the core and outer/valence states. Since the core electrons repel the outer electrons, the valence manifold is subjected to a weaker potential from the nuclei. Consequently, all that is required is to reproduce this screening effect of the core electrons/nuclei and in turn, the plane wave description of the core electrons is dropped. The function of a *pseudopotential* is to effectively describe the core and ionic contributions by a potential which acts on a set of pseudo wavefunctions. The computational saving here is significant in that far fewer plane waves are required to consider a reduced system of only valence electrons. However, in practice, the oscillatory nature of the valence electrons necessitates the convergence of the energy cutoff parameter to obtain an accurate description of the electronic wavefunction.

The construction of a pseudopotential requires that no radial nodes are present within the core region. In addition, the pseudopotential and corresponding pseudo wavefunction ϕ_{PS} must be

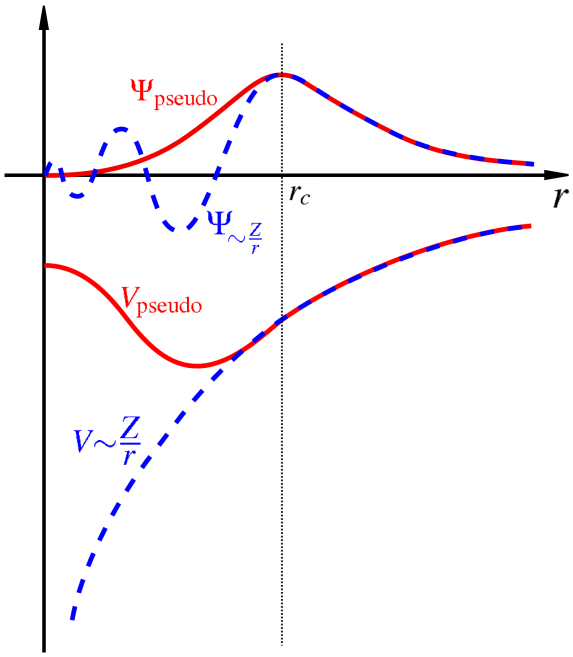

Fig. 2.1 Comparison between the pseudo-wave function and pseudopotential (red) with a Coulomb potential representing the all-electron wave function and potential (blue). Source of image from Wolfram Quester.

identical to the all-electron wavefunction ψ_{AE} outside the cut-off radius r_c, a schematic is shown in figure 2.1.

$$\phi_{PS}(r > r_c) = \psi_{AE}(r > r_c). \tag{2.90}$$

For the DFPT implementations used in this thesis, *norm-conserving* pseudopotentials are used instead of the commonly used ultra-soft pseudopotentials although the latter is able to take advantage of using fewer plane waves. The norm-conserving condition is enforced by ensuring that the all-electron and pseudo wavefunction generate the same charge density within the core radius:

$$\int_0^{r_c} \psi^*_{AE}(\boldsymbol{r})\psi_{AE}(\boldsymbol{r})d\boldsymbol{r} = \int_0^{r_c} \phi^*_{PS}(\boldsymbol{r})\phi_{PS}(\boldsymbol{r})d\boldsymbol{r}. \tag{2.91}$$

The ultra-soft scheme relaxes the norm conservation of the pseudopotential and the resulting missing charge in the core region is accounted for, this requires fewer plane waves. However, the orthonormality of the wavefunctions are affected which introduces complexities in solving the Sternheimer equation. Whilst ultra-soft implementations of DFPT exist [123,

124], extra terms are required to update the augmentation charge. Therefore, the gain in computational savings in using fewer plane waves is diminished due to the extra terms required for computation [118].

2.3.6 Determination of the Ground-State

In order to carry out computations of the linear response, knowledge of the unperturbed quantities which include the ground-state wavefunction and electronic density are required. The theorems of H-K, implemented via the KS scheme provide a practical means of obtaining this information. The self-consistent process to obtain the KS ground-state will now be discussed. This discussion is restricted to the implementation contained in CASTEP, other DFT codes may take a different approach. The start of the DFT calculation involves the reading of user-supplied parameters which define, amongst other things, the plane-wave cutoff energy and k-point mesh used to sample reciprocal space. The relevant pseudopotentials required for the system in question are generated. A trial wavefunction is determined using a one-off relatively cheap computation of the KS state. This involves a lower plane-wave cutoff energy and a less resource-intensive choice of the XC functional compared to the user input. From this trial wavefunction, the electron density can be computed. The KS potential is determined after which the KS equation is solved through some iterative method. From this newly constructed KS state, a new electronic density is calculated. The energy associated with this new density is compared to previous iterations. If a user-defined tolerance is satisfied, the final energy has reached a minimum and the ground-state has been found. A visual representation of the process is shown in figure 2.2.

To speed up convergence in reaching the ground-state, CASTEP employs a density-mixing algorithm [109], in which a density at the current iteration has some input of a density from previous iterations. This, along with iterative minimisation methods will be discussed in later sections, since they are also highly relevant to the DFPT scheme.

It is also mentioned that the CASTEP package offers an alternative choice for electronic minimisation. In the *ensemble density functional theory* scheme, the plane-wave coefficients of the wavefunction are updated such that the energy functional of (2.16) is minimised. The reader is referred to [45] for more information. Whilst this scheme is robust, it is more computationally demanding in comparison to the density mixing scheme. All computations of the ground-state used in this thesis utilise the density mixing scheme.

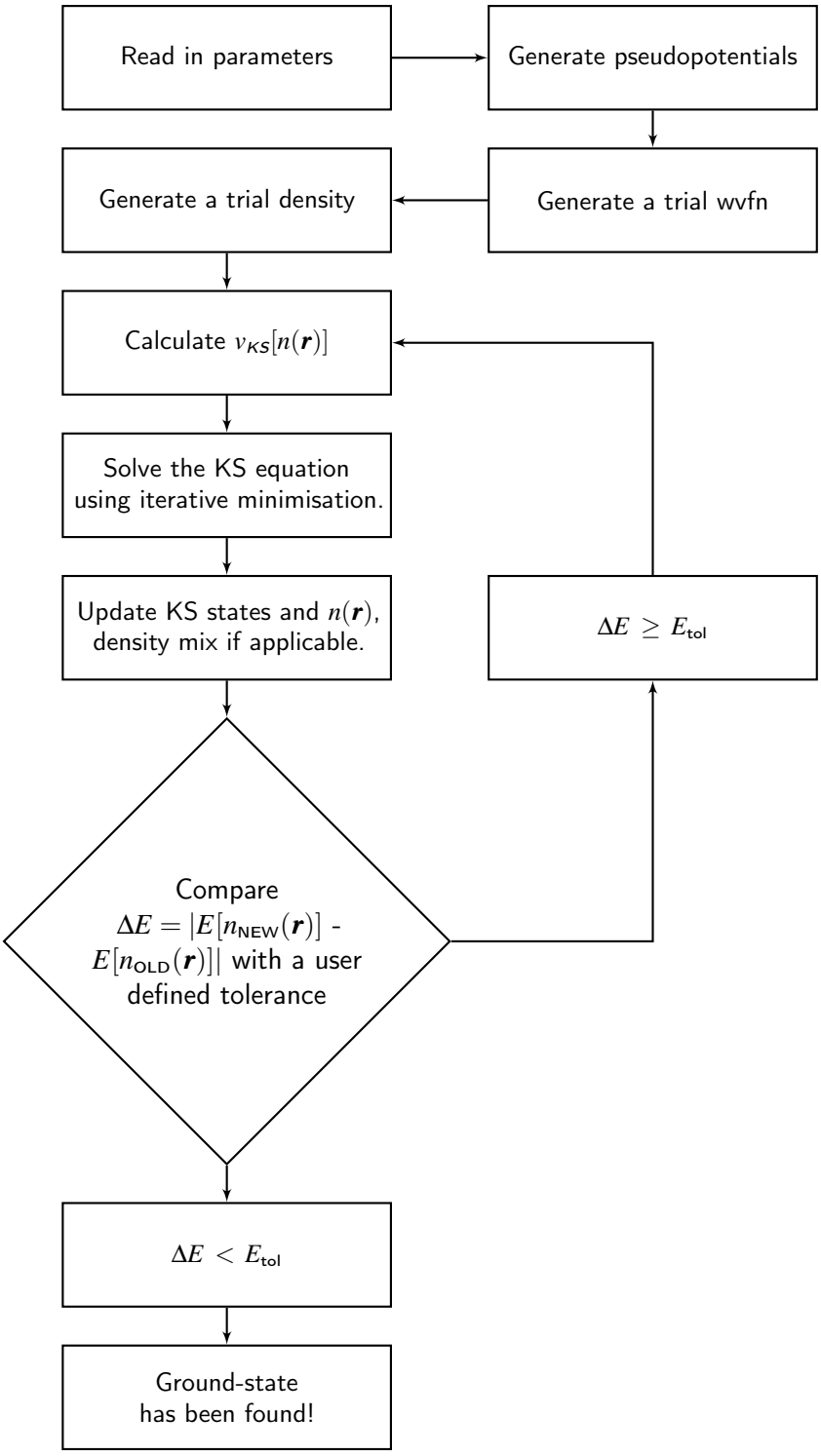

Fig. 2.2 Flow-chart of the self-consistent process in CASTEP used to determine the ground-state.

2.4 Experimental Techniques

This section aims to briefly introduce the experimental techniques that are used to obtain dielectric and spin response spectra. The DFPT implementation of this work can directly be compared to the spectra generated by these techniques.

Spectroscopic ellipsometry is an optical technique that allows for the determination of the dielectric function. This is accomplished by determining the change in the polarisation state of light as it reflects and refracts from a material structure. The complex reflection and refraction coefficients are material-specific parameters and depend directly on the dielectric function. In order to obtain accurate dielectric spectra, external parameters such as the incident angle of light, sample structure and surface roughness are used to fit the experimental data to a model dielectric function. Detailed information can be found in [57, 125].

Investigations of spin-related fluctuations of the electronic density naturally require a probe that is spin-dependent. The neutron has no charge but it does have a magnetic moment. Neutrons can interact with atomic nuclei via very short-range forces and with unpaired electrons through a magnetic dipole interaction. There are numerous experimental methods which allow for the investigation of the magnetic structure. Techniques such as *Inelastic Neutron Scattering* (INS) yield a cross-section that is of similar magnitude to the cross-section of nuclear scattering by the short-ranged nuclear forces. The cross-section is large enough to provide insight into scattering from ordered magnetic structures and electron spin fluctuations. The cross-section measured by INS allows for the determination of the magnetic susceptibility [56, 126]. *Spin-polarised electron-energy loss spectroscopy* (SPEELS) is a technique that is able to measure the dispersion relation of collective excitations. The analysis of the electron's spin state before and after being applied to a magnetic system provides the means to observe spin wave fluctuations [127, 128].

Chapter 3

Dynamical Screening and the Dielectric Response

The first response function of this thesis which will be considered is the dielectric function. To highlight its importance, it will be introduced within the discussion of dynamical screening, which is a constituent of the GW method.

3.1 The Bandgap Problem

Perhaps one of the shortcomings associated most often with DFT is the underestimation of the bandgap with respect to experiment. Figure 3.1 shows this effect is almost universal in wide-gap insulators and semiconductors with a comparison of the computed bandgap using the LDA functional with respect to experimental data [129].

The fundamental bandgap for N electrons is taken to be the difference between the ionisation potential (IP) and electron affinity (EA) [15]:

$$E_{gap}^{N} = IP - EA = [E(N-1) - E(N)] - [E(N) - E(N+1)]\,. \tag{3.1}$$

Instead of the functional $F[n]$ found in equation (2.7), an extension of $\tilde{F}[n]$ is made, which applies to densities that do not necessarily yield an integer number of particles [130]. Two densities are considered:

$$n^{+}(\boldsymbol{r}) = n(\boldsymbol{r}) + \varepsilon(\boldsymbol{r}), \qquad n^{-}(\boldsymbol{r}) = n(\boldsymbol{r}) - \varepsilon(\boldsymbol{r}), \tag{3.2}$$

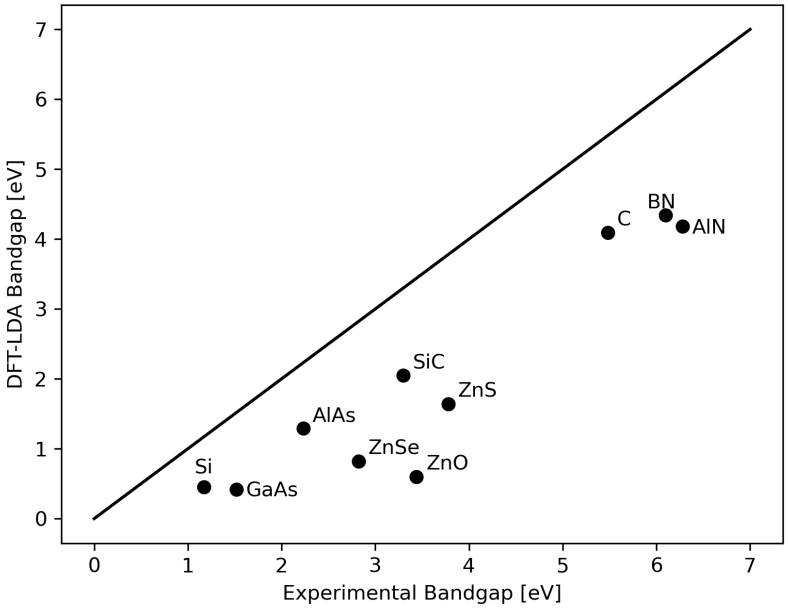

Fig. 3.1 Bandgaps calculated using the DFT-LDA compared to the experimental bandgap. Data taken from Johnson *et al* [129].

where $\varepsilon(\boldsymbol{r})$ is an infinitesimal positive distribution which changes the particle number by an infinitesimal amount, $\int \varepsilon(\boldsymbol{r})d\boldsymbol{r} = \varepsilon \ll 1$. Work in the 80's by Perdew *et al* [131, 132], showed that the derivative discontinuity associated with the $\tilde{F}[n]$ functional at any densities which yield an integer particle number N is expressed:

$$\frac{\delta \tilde{F}[n]}{\delta n(\boldsymbol{r})}|_{n^+(\boldsymbol{r})} - \frac{\delta \tilde{F}[n]}{\delta n(\boldsymbol{r})}|_{n^-(\boldsymbol{r})} = E^N_{gap}. \tag{3.3}$$

Considering the non-interacting kinetic energy functional shown in equation (2.9) extended to apply to non-integer particle numbers, this is denoted as $\tilde{T}_0$. The discontinuity is

$$\frac{\delta \tilde{T}_0[n]}{\delta n(\boldsymbol{r})}|_{n^+(\boldsymbol{r})} - \frac{\delta \tilde{T}_0[n]}{\delta n(\boldsymbol{r})}|_{n^-(\boldsymbol{r})} = E^N_{gap,\,KS}. \tag{3.4}$$

Since $\tilde{F}$ and $\tilde{T}_0$ are two independent functionals of the density, the associated derivative discontinuities cannot be expected to have the same value. Thus, there is a discrepancy between the true bandgap and the KS bandgap. The derivative of the Hartree functional is continuous [9], leaving only the exchange-correlation functional to make up the difference:

$$\Delta_{xc} = \frac{\delta \tilde{E}_{xc}[n]}{\delta n(\boldsymbol{r})}|_{n^+(\boldsymbol{r})} - \frac{\delta \tilde{E}_{xc}[n]}{\delta n(\boldsymbol{r})}|_{n^-(\boldsymbol{r})} = E^N_{gap} - E^N_{gap,\,KS}. \tag{3.5}$$

The issue remains that the most popular implementations of the XC functional such as LDA or GGA *do not* feature these derivative discontinuities. This is made apparent in the LDA computed bandgaps of figure 3.1. The error arises due to the discontinuous dependence of the energy functional on particle number.

Another factor which contributes to the bandgap problem is discussed. The KS system, along with XC and Kinetic, involves the Hartree (Coulomb) term,

$$E_H[n] = \frac{1}{2}\sum_{i,j}\int\int \frac{n_i(\boldsymbol{r})n_j(\boldsymbol{r'})}{|\boldsymbol{r}-\boldsymbol{r'}|}d\boldsymbol{r}d\boldsymbol{r'}. \tag{3.6}$$

This sum includes a self-interaction:

$$E_{self}[n] = \frac{1}{2}\sum_{i}\int\int \frac{n_i(\boldsymbol{r})n_i(\boldsymbol{r'})}{|\boldsymbol{r}-\boldsymbol{r'}|}d\boldsymbol{r}d\boldsymbol{r'}. \tag{3.7}$$

In Hartree-Fock (HF) theory, this term is exactly cancelled by

$$E_X[n] = -\frac{1}{2}\sum_{i,j}\int\int \frac{n_i(\boldsymbol{r})n_j(\boldsymbol{r'})\delta_{ij}}{|\boldsymbol{r}-\boldsymbol{r'}|}d\boldsymbol{r}d\boldsymbol{r'}. \tag{3.8}$$

However in the LDA (and other non-local functionals) there is no exact cancellation which means that an electron is subjected to some extra Coulomb repulsion which originates from itself. The result of this effect can reduce the energy due to a nonphysical delocalisation which closes the bandgap.

An additional component not considered in HF and DFT is the issue of screening. Consider fig 3.2, which illustrates the effect of an electron/hole with respect to the many-body system. The presence of an electron at $\boldsymbol{r}$ interacts with another electron at $\boldsymbol{r'}$ through the usual Coulomb interaction $v(\boldsymbol{r},\boldsymbol{r'})$. In a many-body system, the other electrons collectively interact and rearrange themselves slightly (the noted term for this is polarisation cloud). This induced change in the electronic charge density is denoted by $\delta\rho(\boldsymbol{r''})$. In turn, this induced charge density subjects the electron at point $\boldsymbol{r'}$ to a Coulomb interaction. The screened interaction is therefore a measure of the initial Coulomb potential between the two electrons and the collective polarisation cloud.

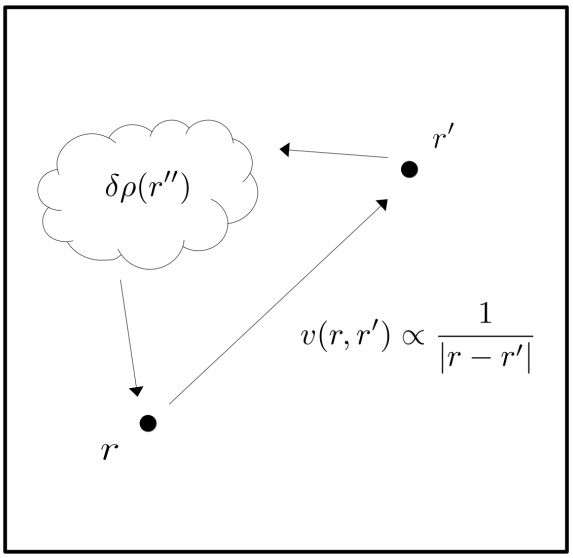

Fig. 3.2 Sketch of the bare Coulomb interaction between two electrons and the induced Polarisation cloud.

$$W(\boldsymbol{r},\boldsymbol{r'}) = v(\boldsymbol{r},\boldsymbol{r'}) + \int d\boldsymbol{r''} v(\boldsymbol{r'},\boldsymbol{r''}) \delta\rho_{\boldsymbol{r}}(\boldsymbol{r''}). \tag{3.9}$$

To rectify the bandgap problem in DFT, work has been done to develop various functionals, some of which include taking into account screening. Clark *et al* replaced the LDA functional with a short-ranged Thomas-Fermi screened Coulomb potential [133], this is shown to improve the bandgap in semiconductors such as Si and GaAs. The next chapter will discuss the quantities that make up the screened interaction.

3.2 The GW Method

This section will aim to introduce the *GW* method and quantities involved. It follows that these quantities constitute the formulation of the dielectric response. The link between the dielectric response and the screened interaction is then made.

At approximately the same period as when the HK and KS ideas in DFT were established, Hedin published the *GW* method [134]. Unlike DFT however, it did not gain notability swiftly, primarily due to the relatively expensive computational requirements. The method has seen much use in addressing the deficiencies found in DFT such as the bandgap problem [135].

Aptly named, the *GW* method consists of two quantities, the G is in reference to the Green's function used to describe the propagation of a quasiparticle. In quantum mechanical terms, this is the probability amplitude:

$$G(\boldsymbol{r},t,\boldsymbol{r'},t') = -i\langle N|\hat{T}\{\hat{c}(\boldsymbol{r},t)\hat{c}^{\dagger}(\boldsymbol{r'},t')\}|N\rangle. \tag{3.10}$$

This single-particle Green's function acts on the N-th electron state in which the order of either an addition or removal of an electron can be described by the use of the time ordering operator $\hat{T}$. The field operators $\hat{c}$ and $\hat{c}^{\dagger}$ specify the annihilation/creation of an electron. The Lehmann representation involves taking the Fourier transform of the Green's function from the time to the energy axis.

$$G(\boldsymbol{r},\boldsymbol{r'},\omega) = \sum_a \frac{\Psi_{N+1,a}(\boldsymbol{r})\Psi^*_{N+1,a}(\boldsymbol{r'})}{\omega + (E_N - E_{N+1,a}) + i\eta} + \sum_j \frac{\Psi_{N-1,j}(\boldsymbol{r})\Psi^*_{N-1,j}(\boldsymbol{r'})}{\omega + (E_{N-1,j} - E_N) - i\eta}. \tag{3.11}$$

This sum runs over all $N+1$ excited states in which an electron has been added and $N-1$ states in which an electron has been removed, the infinitesimal η is included for convergence purposes. $E_{N+1,a}$ and $E_{N-1,j}$ are the energies of the a-th $(N+1)$ electron state and j-th $(N-1)$ electron state respectively. Note that the poles of the interacting Green's function are linked to the quasiparticle energies. The function Ψ corresponds to the many-body wavefunction which is impractical to obtain. Practically, a more attainable quantity to work with is the non-interacting Green's function (G_0) as the KS orbitals and eigenvalues from DFT can be used. The Lehmann representation of G_0 has a similar form:

$$G_0(\boldsymbol{r},\boldsymbol{r'},\omega) = \sum_n^{occ} \frac{\psi_n(\boldsymbol{r})\psi^*_n(\boldsymbol{r'})}{\omega - \varepsilon_n + i\eta} + \sum_n^{unocc} \frac{\psi_n(\boldsymbol{r})\psi^*_n(\boldsymbol{r'})}{\omega - \varepsilon_n - i\eta}. \tag{3.12}$$

The summation includes all occupied and empty states. The poles are related to the noninteracting quasiparticle energies which are $\varepsilon_n = E(N) - E(N-1)$ for ε_n below the Fermi energy and $\varepsilon_n = E(N+1) - E(N)$ for ε_n above the Fermi energy.

The W refers to the screened Coulomb interaction. These two make up the central quantity of the *GW* method which is termed the *self-energy*. This quantity encodes all information with respect to the mutual interactions of an electron with its environment:

$$\Sigma = iGW. \tag{3.13}$$

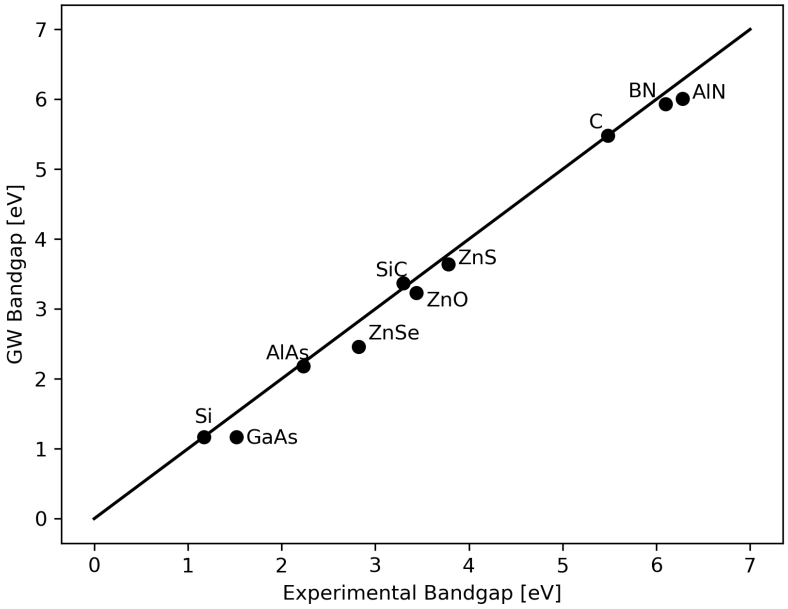

Fig. 3.3 Bandgaps calculated using the GW correction compared to experiment. Data taken from Johnson *et al* [129].

The self-energy is a non-local, energy-dependent potential $\Sigma_{GW}(\boldsymbol{r},\boldsymbol{r'},E)$ which replaces the KS potential. It is often used to provide a correction to the KS eigenvalues [135]. Like the KS scheme, the dependency of terms requires self-consistency in order to determine the corresponding GW eigenvalues:

$$\varepsilon_{GW} = \varepsilon_{DFT} + \langle \psi_{KS} | \Sigma_{GW}(\varepsilon_{GW}) - v_{xc} | \psi_{KS} \rangle \,. \tag{3.14}$$

This correction to the DFT KS eigenvalues is highly effective. Figure 3.3 illustrates the effect of the GW correction onto the bandgap [129]. The correction effectively closes the bandgap which is underestimated in DFT for most systems, highlighting the importance of the screened interaction.

To better understand the origin of the screened interaction in the many-body picture and to book-keep variables more efficiently, the diagrammatic representation of Feynman diagrams will be employed. The bare Coulomb $v(\boldsymbol{r},t)$, interacting G and non-interacting G_0 Green's functions are represented in the following form:

v :

G can be expressed diagrammatically in the following, the diagrams shown here are topologically distinct, (see [134, 135] for more information) and contain up to $n = 1$ Coulomb interaction (v)-lines with up to $2n+1 = 3$ non-interacting greens function (G_0)-lines:

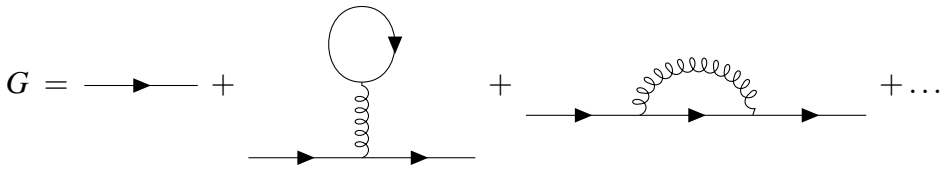

The first diagram with no Coulomb interaction ($n = 0$) is simply G_0, and the second diagram with $n = 1$ refers to the Hartree interaction, this represents the Coulombic repulsion energy of two charge densities. The last $n = 1$ diagram represents the Fock exchange, in the quantum picture this provides a correction to the self-interaction. The complicated $n \geq 2$ diagrams are not shown here but contain some combination of G, G_0 and v. Formally, the Green's function has the following structure:

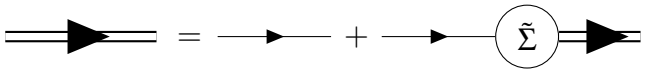

The self-energy ($\tilde{\Sigma}$) above is termed *reducible* and consists of diagrams with no external G_0 lines. In practice, the useful quantity is the *irreducible* self-energy (Σ) [135, 136]. These diagrams follow the rule that no G_0 line can be cut to separate the diagram into smaller pieces with the same structure. The full (irreducible) self-energy can therefore be expressed as

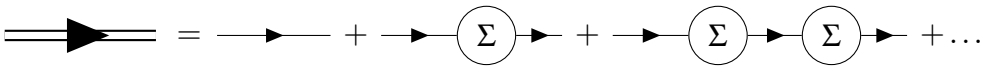

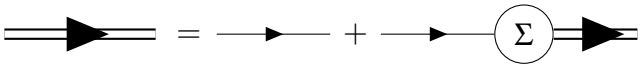

In which G again is found, this series expansion for G is known as the Dyson series [135], the Dyson equation is now presented with the parameters in space-time dropped for readability:

$$G = G_0 + G_0 \Sigma G. \tag{3.15}$$

In the KS method, HF is used along with XC to make up the KS potential. A poor approximation for the self-energy would be to only use HF:

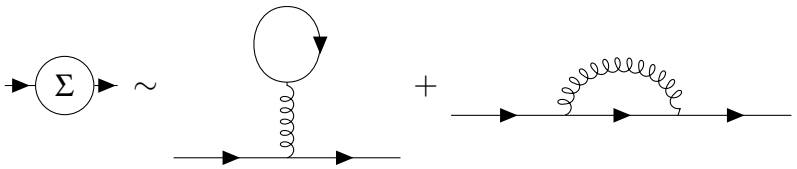

There is no consideration of screening here and the use of only HF has been shown to qualitatively fail in describing the bandgap [137]. An infinite series of HF interactions are considered to represent the screened interaction. The *Random Phase Approximation* (RPA) [138, 139], asserts that the screening is determined by a series of repeated interactions with electron/electron or hole/hole pairs:

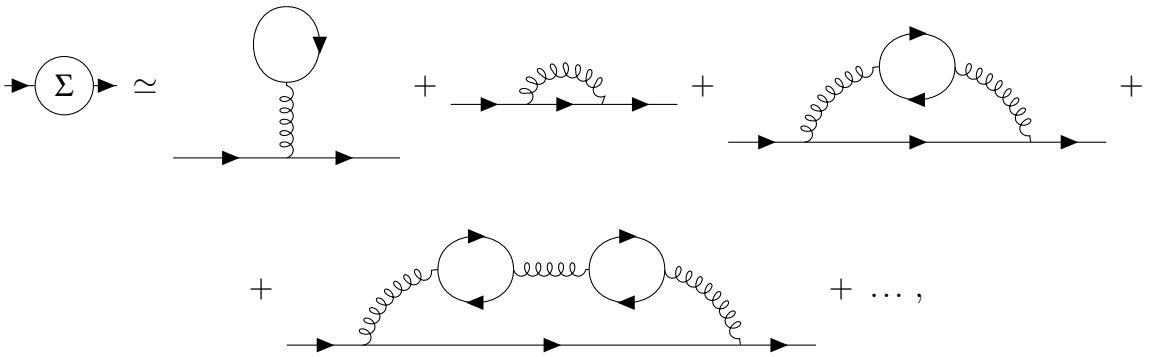

where the screened interaction in the RPA is this sum of interactions:

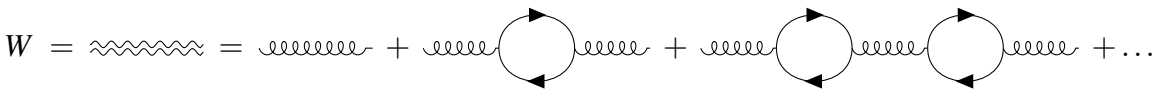

In a similar fashion to which G was treated previously, the screened Coulomb interaction is found again on the right-hand side:

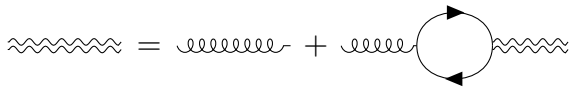

The screened interaction presented here is written in terms of the bare Coulomb interaction and the non-interacting Green's function, again the parameters are dropped for now:

$$W = v + vG_0G_0W. \tag{3.16}$$

Including space-time parameters, the screened interaction diagram is formally expressed as

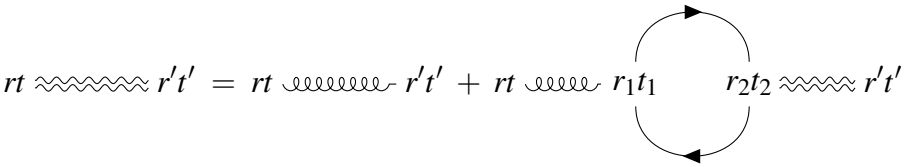

The corresponding equation is

$$W(\boldsymbol{r},\boldsymbol{r'},t,t') = v(\boldsymbol{r},\boldsymbol{r'},t,t') + \int d\boldsymbol{r}_1 \int dt_1 \int d\boldsymbol{r}_2 \int dt_2\, v(\boldsymbol{r},\boldsymbol{r}_1,t,t_1)G_0(\boldsymbol{r}_1,t_1,\boldsymbol{r}_2,t_2) \\ G_0(\boldsymbol{r}_2,t_2,\boldsymbol{r}_1,t_1)W(\boldsymbol{r}_2,\boldsymbol{r'},t_2,t'). \tag{3.17}$$

Hedin's [134] approximation defined a quantity which represents the bubble corresponding to the two G_0 lines:

$$\chi_0(\boldsymbol{r}_1\boldsymbol{r}_2,t_1,t_2) = -i \int d\boldsymbol{r}_1 \int dt_1 \int d\boldsymbol{r}_2 \int dt_2 G_0(\boldsymbol{r}_1,\boldsymbol{r}_2,t_2-t_1)G_0(\boldsymbol{r}_1,\boldsymbol{r}_2,t_1-t_2). \tag{3.18}$$

This is known as the *irreducible polarisability*, Adler-Wiser took expression (3.18), utilised the Fourier transform and rewrote χ_0 in terms of KS orbitals and energies [140, 141]. The resultant expression:

$$\chi_0(\boldsymbol{r}_1,\boldsymbol{r}_2,\omega) = \sum_{j}^{occ}\sum_{a}^{unocc}\left[\frac{\psi_j^*(\boldsymbol{r})\psi_a(\boldsymbol{r})\psi_a^*(\boldsymbol{r'})\psi_j(\boldsymbol{r'})}{\omega-(\varepsilon_a-\varepsilon_j)+i\eta} - \frac{\psi_j(\boldsymbol{r})\psi_a^*(\boldsymbol{r})\psi_a(\boldsymbol{r'})\psi_j^*(\boldsymbol{r'})}{\omega+(\varepsilon_a-\varepsilon_j)-i\eta}\right]. \tag{3.19}$$

The spin-dependency of the KS orbitals is not shown explicitly, for the dielectric response it is proposed that the spins are degenerate. χ_0 is also known as the *non-interacting density response function* if there was no frequency dependence ($\omega = 0$). An equivalent formulation of the Adler-Wiser expression [140, 141]:

$$\chi_0(\boldsymbol{r}_1, \boldsymbol{r}_2, \omega) = 2\sum_{nm} \frac{f_n - f_m}{\varepsilon_n - \varepsilon_m \pm \omega + i\eta} \psi_m^*(\boldsymbol{r}_1)\psi_n(\boldsymbol{r}_1)\psi_m(\boldsymbol{r}_2)\psi_n^*(\boldsymbol{r}_2), \tag{3.20}$$

where f_n and f_m are occupation factors and correspond to either 1 if occupied or 0 if unoccupied. This runs over all occupied and unoccupied states (nm) and the factor of 2 arises due to spin degeneracy.

Taking the Fourier transform of (3.17) and noting that the bare Coulomb interaction is solely space-dependent:

$$W(\boldsymbol{r}, \boldsymbol{r'}, \omega) = v(\boldsymbol{r}, \boldsymbol{r'}) + \int d\boldsymbol{r}_1 \; v(\boldsymbol{r}, \boldsymbol{r}_1) \int d\boldsymbol{r}_2 \; \chi_0(\boldsymbol{r}_1, \boldsymbol{r}_2, \omega) W(\boldsymbol{r}_2, \boldsymbol{r'}, \omega). \tag{3.21}$$

The upcoming sections will discuss the practicalities of obtaining the polarisability with the plane-wave pseudopotential method implementation of CASTEP. At this point, what can be proposed is that the functions involved in equation (3.17) can be regarded as matrices with dimensions proportional to the size of the real space (or reciprocal grid) involved in the computation. Expressing equation (3.21) in matrix form:

$$\underline{W}(\omega) = \underline{v} + \underline{v} \; \underline{\chi_0}(\omega) \; \underline{W}(\omega), \tag{3.22}$$

where these matrices hold for a representation in real space or reciprocal space and so parameters other than the frequency are dropped. Collecting the screened interaction on the left and the bare Coulomb interaction on the right, equation (3.22) is written as

$$\underline{W}(\omega) = \left[\underline{\boldsymbol{I}} - \underline{v} \; \underline{\chi_0}(\omega)\right]^{-1} \underline{v}, \tag{3.23}$$

where $\underline{\boldsymbol{I}}$ refers to the identity matrix. The frequency-dependent dielectric matrix is defined to be:

$$\varepsilon(\omega) = \underline{\boldsymbol{I}} - \underline{v} \; \underline{\chi_0}(\omega). \tag{3.24}$$

Which gives:

$$\underline{W}(\omega) = \underline{\varepsilon}^{-1}(\omega)\underline{v}. \tag{3.25}$$

The dielectric function provides the relation between the initial bare Coulomb potential and the resultant screened Coulomb potential. The dielectric response is termed to be the response of a system from a bare Coulomb perturbation, which is why it is closely related to the polarisability [9, 140]. The screened Coulomb interaction in integral form is

$$W(\boldsymbol{r},\boldsymbol{r}',\omega) = \int d\boldsymbol{r}''\varepsilon^{-1}(\boldsymbol{r}'',\boldsymbol{r}',\omega)v(\boldsymbol{r},\boldsymbol{r}''). \tag{3.26}$$

Whilst most readers are familiar with the dielectric constant which in this formulation is just the $\omega = 0$ (static) case. This thesis is concerned with computing the frequency-dependent dielectric response. Equation (3.26) shows that this is required in order to obtain the screened interaction.

Recall that the formulation of the KS potential of DFT is to reduce the many-body/interacting picture and instead impose a non-interacting potential to study its behaviour. Similarly, the dielectric response encodes the collective behaviour of a system by computation of the non-interacting density response function.

3.3 Sternheimer and Sum-Over-States

This section aims to map the sum-over-states representation used in the definition of χ_0 to the previously discussed Sternheimer approach.

The expression for the Adler-Wiser polarisability (3.19) contains two sums over occupied and unoccupied KS states, formally, an infinite number of unoccupied states are required [142]:

$$\chi_0(\boldsymbol{r},\boldsymbol{r}',\omega) = \sum_{i}^{N_e}\sum_{a=N_e+1}^{\infty}\left[\frac{\psi_a(\boldsymbol{r})\psi_i(\boldsymbol{r}')\psi_i^*(\boldsymbol{r})\psi_a^*(\boldsymbol{r}')}{\omega-(\varepsilon_a-\varepsilon_i)+i\eta} - \frac{\psi_i(\boldsymbol{r})\psi_a(\boldsymbol{r}')\psi_a^*(\boldsymbol{r})\psi_i^*(\boldsymbol{r}')}{\omega+(\varepsilon_a-\varepsilon_i)-i\eta}\right]. \tag{3.27}$$

The occupied sum runs from 1 to the total number of electrons N_e and the unoccupied sum runs from N_e+1 to infinity. The frequency-dependent density response is

$$\delta\rho(\boldsymbol{r},\omega) = \int d\boldsymbol{r} \int d\boldsymbol{r}' \chi_0(\boldsymbol{r},\boldsymbol{r}',\omega)\delta v_{ext}(\boldsymbol{r}'). \tag{3.28}$$

Where linear response theory allows us to connect the induced density response to an external perturbing potential through the density-density response function. The density response in terms of KS states is expressed in the following:

$$\begin{aligned}\delta\rho(\boldsymbol{r},\omega) = \sum_{i=1}^{N_e} \Bigg[\int d\boldsymbol{r}\ \psi_i^*(\boldsymbol{r}) \int d\boldsymbol{r}' \sum_{N_e+1}^{\infty} \frac{\psi_a(\boldsymbol{r})\psi_a^*(\boldsymbol{r}')\psi_i(\boldsymbol{r}')}{\omega-(\varepsilon_a-\varepsilon_i)+i\eta}\delta v_{ext}(\boldsymbol{r}') \\ - \int d\boldsymbol{r}\ \psi_i(\boldsymbol{r}) \int d\boldsymbol{r}' \sum_{N_e+1}^{\infty} \frac{\psi_a(\boldsymbol{r})\psi_a^*(\boldsymbol{r}')\psi_i^*(\boldsymbol{r}')}{\omega+(\varepsilon_a-\varepsilon_i)-i\eta}\delta v_{ext}(\boldsymbol{r}') \Bigg].\end{aligned} \tag{3.29}$$

The second term (line 2) of equation (3.29) is considered and the i-th first order response is taken to be defined as

$$\delta\psi_i(\boldsymbol{r},\omega) = -\int d\boldsymbol{r}' \sum_{a=N_e+1}^{\infty} \frac{\psi_a(\boldsymbol{r})\psi_a^*(\boldsymbol{r}')\psi_i(\boldsymbol{r}')}{\omega+(\varepsilon_a-\varepsilon_i)-i\eta}\delta v_{ext}(\boldsymbol{r}'). \tag{3.30}$$

Multiplying both sides of the first order response by $\left(\hat{H}-\varepsilon_i+\omega-i\eta\right)$:

$$\left(\hat{H}-\varepsilon_i+\omega-i\eta\right)\delta\psi_i(\boldsymbol{r},\omega) = -\int d\boldsymbol{r}' \sum_{a=N_e+1}^{\infty} \left(\hat{H}-\varepsilon_i+\omega-i\eta\right) \frac{\psi_a(\boldsymbol{r})\psi_a^*(\boldsymbol{r}')\psi_i(\boldsymbol{r}')}{\omega+(\varepsilon_a-\varepsilon_i)-i\eta}\delta v_{ext}(\boldsymbol{r}'). \tag{3.31}$$

Using $\hat{H}\psi_a = \varepsilon_a\psi_a$, the numerator and denominator simplify leaving:

$$\left(\hat{H}-\varepsilon_i+\omega-i\eta\right)\delta\psi_i(\boldsymbol{r},\omega) \;=\; -\int d\boldsymbol{r}' \sum_{a=N_e+1}^{\infty} (1)\psi_a(\boldsymbol{r})\psi_a^*(\boldsymbol{r}')\psi_i(\boldsymbol{r}')\delta v_{ext}(\boldsymbol{r}'). \tag{3.32}$$

The completeness of the KS states defines:

$$\sum_{l=1}^{\infty} = \psi_l(\boldsymbol{r})\psi_l^*(\boldsymbol{r}') = \delta(\boldsymbol{r}-\boldsymbol{r}'). \tag{3.33}$$

The summation over the unoccupied KS states from (N_e+1) to ∞ can be replaced by

$$\sum_{l=N_e+1}^{\infty} \psi_l(\boldsymbol{r})\psi_l^*(\boldsymbol{r'}) = \delta(\boldsymbol{r}-\boldsymbol{r'}) - \sum_{i=1}^{N_e} \psi_i(\boldsymbol{r})\psi_i^*(\boldsymbol{r'}). \tag{3.34}$$

Substituting this replacement back into equation (3.32):

$$\left(\hat{H} - \varepsilon_i + \omega - i\eta\right) \delta\psi_i(\boldsymbol{r},\omega) = -\int d\boldsymbol{r'} \left(\delta(\boldsymbol{r}-\boldsymbol{r'}) - \sum_{i=1}^{N_e} \psi_i(\boldsymbol{r})\psi_i^*(\boldsymbol{r'}) \right) \psi_i(\boldsymbol{r'})\delta v_{ext}(\boldsymbol{r'}). \tag{3.35}$$

It is now recognised that the summation in the bracketed term on the right-hand side over the i occupied KS states corresponds to the projection operator over occupied states ($\hat{P}_{occ}$). Taking $\boldsymbol{r} = \boldsymbol{r'}$, the Kronecker delta simplifies:

$$\left(\hat{H} - \varepsilon_i + \omega - i\eta\right) \delta\psi_i(\boldsymbol{r},\omega) = -\left(1 - \hat{P}_{occ}\right) \delta v_{ext}(\boldsymbol{r})\psi_i(\boldsymbol{r}), \tag{3.36}$$

where the Sternheimer equation from equation (2.69) is found yet again. The first term (line 1) of equation (3.29) can be treated in the same fashion by defining a similar-looking first-order response:

$$\widetilde{\delta\psi}_i(\boldsymbol{r},\omega) = \int d\boldsymbol{r'} \sum_{a=N_e+1}^{\infty} \frac{\psi_a(\boldsymbol{r})\psi_a^*(\boldsymbol{r'})\psi_i(\boldsymbol{r'})}{\omega - (\varepsilon_a - \varepsilon_i) + i\eta} \delta v_{ext}(\boldsymbol{r'}). \tag{3.37}$$

The density response can now be rewritten more compactly in terms of these first-order response functions:

$$\delta\rho(\boldsymbol{r},\omega) = \sum_{i=1}^{N_e} \left[\psi_i^*(\boldsymbol{r})\widetilde{\delta\psi}_i(\boldsymbol{r},\omega) + \psi_i(\boldsymbol{r}) \left[\delta\psi_i(\boldsymbol{r},\omega)\right]^* \right]. \tag{3.38}$$

What has been shown here is the connection between the sum-over-states and the Sternheimer method. Through the definition of the first-order response wavefunction, the two are shown to be formally equivalent. A significant advantage highlighted in (3.34) is that the Sternheimer method only requires knowledge of occupied states [76]. The requirements for the wavefunctions used in the formulation of the Sternheimer equation in section 2.2.3 are also present here, such as orthonormality as shown in equation (3.33). Equation (3.34) necessitates that the plane-wave basis set is able to provide an adequate description of the

occupied states. If not, then the projection operators become ill-defined, complicating the solution to the Sternheimer equation.

To summarise, the calculation of the complicated polarisability involving an impractical sum over virtual orbitals is avoided by the calculation of the formally equivalent induced charge density which involves the first-order response KS orbitals.

3.4 Frequency Dependent Dielectric Matrix

The specifics of solving the Sternheimer equation with respect to a Coulomb perturbation will now be discussed instead of generalising to some external potential. Giustino *et al* [143, 144] have derived the Sternheimer equation using the Bloch representation first shown in section 2.3.1. This is over occupied states ψ_n in which both positive and negative frequency components are considered with respect to the first-order response orbitals ($\Delta\psi_n^{\pm}$). More details of this formulation may be found in [136]:

$$\left(\hat{H} - \varepsilon_n \pm \omega + i\eta\right) \Delta\psi^{\pm}_{n\boldsymbol{k}[\boldsymbol{r},\omega]}(\boldsymbol{r}') = -\left(1 - \hat{P}_{occ}\right) \Delta V_{[\boldsymbol{r},\omega]}(\boldsymbol{r}')\psi_n(\boldsymbol{r}'). \tag{3.39}$$

From (3.24), the dielectric matrix [136] is defined as

$$\varepsilon(\boldsymbol{r},t,\boldsymbol{r}',t') = \delta(\boldsymbol{r}-\boldsymbol{r}')\delta(t-t') - \int d\boldsymbol{r}'' v(\boldsymbol{r},\boldsymbol{r}'')\chi_0(\boldsymbol{r}'',t,\boldsymbol{r}',t'). \tag{3.40}$$

Performing a Fourier transform to the frequency domain and using (3.20):

$$\varepsilon(\boldsymbol{r},\boldsymbol{r}',\omega) = \delta(\boldsymbol{r}-\boldsymbol{r}') - 2\int v(\boldsymbol{r},\boldsymbol{r}'') \sum_{nm} \frac{(f_n - f_m)\psi_m^*(\boldsymbol{r}_1)\psi_n(\boldsymbol{r}_1)\psi_m(\boldsymbol{r}_2)\psi_n^*(\boldsymbol{r}_2)}{\varepsilon_n - \varepsilon_m \pm \omega + i\eta}. \tag{3.41}$$

Defining the first-order variations with respect to the sign of the frequency:

$$\Delta\psi_n^{\pm} = \sum_m \frac{\langle\psi_m|\,\Delta V_{[\boldsymbol{r},\omega]}\,|\psi_n\rangle}{\varepsilon_n - \varepsilon_m \pm \omega + i\eta}\psi_m. \tag{3.42}$$

Section 3.3 showed how the impractical sum-over-states summation in (3.41) is eliminated by the usage of the first-order wavefunctions which make up the induced charge density. By restricting n to the occupied manifold in equation (3.41) and noticing that the occupation factors contribute only if they reference opposing manifolds, the dielectric response is

$$\varepsilon(\boldsymbol{r},\boldsymbol{r'},\omega) = \delta(\boldsymbol{r},\boldsymbol{r'}) - 2\sum_{n\in occ}\psi_n^*(\boldsymbol{r'})\left(\Delta\psi^+_{n[\boldsymbol{r},\omega]}(\boldsymbol{r'}) + \Delta\psi^-_{n[\boldsymbol{r},\omega]}(\boldsymbol{r'})\right). \tag{3.43}$$

The induced charge density oscillates in frequency and requires knowledge of both ground-state and first-order response wavefunctions:

$$\Delta n_{[\boldsymbol{r},\omega]}(\boldsymbol{r'}) = 2\sum_{n\in occ}\psi_n^*(\boldsymbol{r'})\left(\Delta\psi^+_{n[\boldsymbol{r},\omega]}(\boldsymbol{r'}) + \Delta\psi^-_{n[\boldsymbol{r},\omega]}(\boldsymbol{r'})\right). \tag{3.44}$$

Directly relating the dielectric response to the induced charge density:

$$\varepsilon(\boldsymbol{r},\boldsymbol{r'},\omega) = \delta(\boldsymbol{r},\boldsymbol{r'}) - \Delta n_{[\boldsymbol{r},\omega]}(\boldsymbol{r'}). \tag{3.45}$$

The frequency dependence of the screened Coulomb potential ($\Delta V_{[\boldsymbol{r},\omega]}$) is due to the screened Hartree potential associated with the induced charge:

$$\Delta V_{[\boldsymbol{r},\omega]}(\boldsymbol{r'}) = v(\boldsymbol{r},\boldsymbol{r'}) + \Delta V^{\mathrm{H}}_{[\boldsymbol{r},\omega]}(\boldsymbol{r'}) = v(\boldsymbol{r},\boldsymbol{r'}) + \int d\boldsymbol{r''}\Delta n_{[\boldsymbol{r},\omega]}(\boldsymbol{r''})v(\boldsymbol{r''},\boldsymbol{r'}). \tag{3.46}$$

This work implements the *non-self-consistent* (NSCF) [136, 143] Sternheimer method which fixes the external potential on the right-hand side of equation (3.39) to the bare Coulomb interaction. A plane-wave perturbation is applied via the bare Coulomb potential $v(\boldsymbol{r},\boldsymbol{r'})$. The Sternheimer equations for $\pm\omega$ are solved for the first-order response wavefunctions and then the induced charge density can be calculated. This gives the frequency-dependent dielectric response. Whilst the first-order response variables are determined in an NSCF manner, this method still requires a self-consistent ground-state. The NSCF Sternheimer equation is written as

$$\left(\hat{H} - \varepsilon_n \pm \omega + i\eta\right)\Delta\psi^{\pm}_{n\boldsymbol{k}[\boldsymbol{r},\omega]}(\boldsymbol{r'}) = -\left(1-\hat{P}_{occ}\right)v_{[\boldsymbol{r}]}\psi_n(\boldsymbol{r'}). \tag{3.47}$$

Intuitively the calculation of the dielectric response is likened to the picture presented earlier in figure 3.2. An external perturbation causes the electrons in the system to respond by rearranging into a polarisation cloud. It is this polarisability in the *RPA* which is directly related to the dielectric response. In order to obtain the screened Coulomb interaction with the NSCF method, the dielectric matrix in (3.45) must be solved for all $\boldsymbol{r},\boldsymbol{r'}$ and then inverted (3.25).

It is also mentioned in passing that the *self-consistent* approach of the Sternheimer method shown in (3.39) involves setting the external potential to the screened Coulomb interaction [143]. For the first iteration, this is the bare Coulomb interaction since no induced charge exists and therefore the induced Hartree screening in (3.46) is zero. For all subsequent iterations, the screened Coulomb interaction is calculated at every iteration from the induced charge density using equation (3.46). Self-consistency is reached when the energy associated with the induced charge density is (within some tolerance) comparable to values from previous iterations. Once the screened interaction is known, the inverse dielectric matrix is known by (3.26).

The practicalities of obtaining the solution to these two Sternheimer equations ($\Delta\psi_n^{\pm}$) are now to be discussed. The formal definition of the first-order response as shown in various representations with equations (3.37), (3.30) and (3.42) all involve summations over the occupied manifold. Unlike the case of the Harmonic Oscillator in which an analytic expression is used to determine the response, here the electronic density cannot be determined by such a simplistic expression due to the complicated Hamiltonian. Making only a numerical approach viable to determine the response to the KS system.

Equation (3.47) involves a system of linear equations. For a given k-point, each KS eigenstate (or band) corresponds to an array with dimension proportional to the number of plane waves N_G. The Hamiltonian operator is a matrix of size $N_G \times N_G$ and is not explicitly stored in its entirety for the purpose of computational efficiency. From section 2.3.1, it is reminded that each band is defined by plane-wave coefficients and that the KS wavefunction requires knowledge of each band for all k-points. Hence, equation (3.47) involves arrays of real or reciprocal space which must be solved for each electronic band and k-point of the KS system. For a single band and k-point, the linear system of the Sternheimer equation can be represented as

$$\boldsymbol{A}\boldsymbol{x} = \boldsymbol{b}, \tag{3.48}$$

where $\boldsymbol{A}$ is a $N \times N$ symmetric positive-definite matrix, $\boldsymbol{x}$ and $\boldsymbol{b}$ are vectors of size N. Such a system of linear equations falls under the Krylov subspace [145], where numerical methods such as the iterative conjugate gradient algorithm can be employed to solve for $\boldsymbol{x}$ (the first-order response) given a known $\boldsymbol{b}$ (the bare Coulomb potential applied to the projected KS ground-state). One requirement for the usage of a conjugate gradient algorithm is for $\boldsymbol{A}$ to be hermitian. The Hamiltonian is constructed in steps, the arrays corresponding to the Kinetic energy operator have a diagonal presentation in reciprocal space. The Hartree and

Exchange-Correlation contribution is diagonal in real space. The CASTEP package makes use of Fast Fourier Transform libraries to efficiently switch back and forth [41]. The KS eigenvalues of the Hamiltonian are real and do not affect hermicity, indeed conjugate gradient is readily utilised for ground-state calculations [45]. The implications of the perturbing frequency being either real or imaginary will be discussed in later sections, but for now, ω is proposed to be real. It is the imaginary infinitesimal $i\eta$ that prohibits the use of conjugate gradient and now prompts the discussion of solvers which can be generalised to deal with non-hermitian arrays.

3.5 Numerical methods

This section aims to briefly introduce the iterative numerical methods used to obtain the first-order response required for the computation of the dielectric matrix. The expression in (3.48) belongs to the Krylov subspace [145, 146] and is equivalently expressed as

$$\sum_{ij} A_{ij} x_j = \sum_i b_i. \tag{3.49}$$

Consider the quadratic form in which each array element is expressed:

$$f(x_i) = \frac{1}{2}\sum_{ij} x_j A_{ij} x_i - \sum_i b_i x_i + c. \tag{3.50}$$

Taking the derivative with respect to the k-th index:

$$\frac{\partial f(x_i)}{\partial x_k} = \frac{1}{2}\sum_j \frac{dx_j}{dx_k}\sum_i A_{ij} x_i + \frac{1}{2}\sum_j x_j \sum_i A_{ij}\frac{dx_i}{dx_k} - \sum_i b_i \frac{dx_i}{dx_k} + \frac{d}{dx_k}c, \tag{3.51}$$

$$f'(x_k) = \frac{1}{2}\sum_{ik} x_k A_{ik} x_i + \frac{1}{2}\sum_{jk} x_j A_{kj} x_k - \sum_i b_i + 0. \tag{3.52}$$

If $\boldsymbol{A}$ is indeed symmetric, the equation reduces to

$$f'(x) = \frac{1}{2}\boldsymbol{A}^T\boldsymbol{x} + \frac{1}{2}\boldsymbol{A}\boldsymbol{x} - \boldsymbol{b} = \boldsymbol{A}\boldsymbol{x} - \boldsymbol{b}. \tag{3.53}$$

Therefore, all x_k's which result in the gradient going to zero ($f'(x_k) = 0$) provide a solution to the linear system of (3.48). The following numerical methods provide the means of obtaining these solutions.

3.5.1 Steepest Descent Method

The method of Steepest Descent (SD) initialises by starting at some arbitrary point $x_{(k)}$ and taking a specific step to $x_{(k+1)}$ in which f decreases. The Steepest Descent, otherwise known as Gradient Descent [147], relies on the presumption that the step direction is opposite to that of the gradient ($-f'(x_{(k)})$):

$$x_{(k+1)} = x_{(k)} + \alpha_{(k)} p_{(k)}. \tag{3.54}$$

Here $p_{(k)}$ is the step direction and $\alpha_{(k)}$ is a scalar denoting how far the step is along the direction. An important definition is given here to denote the negative of the gradient at $x_{(k)}$. The *residual* is written as

$$r_{(k)} = b - Ax_{(k)}, \tag{3.55}$$

where the residual is equal to the negative of the gradient from (3.53). The steepest descent method sets the step direction equivalent to the residual ($p_{(k)} = r_{(k)}$), this means equation (3.54) is now:

$$x_{(k+1)} = x_{(k)} + \alpha r_{(k)}. \tag{3.56}$$

In order to determine the step size (α), a *line search* is used whereby an α is chosen such as to minimise f along a line [148]. Using calculus and the orthogonality property:

$$\alpha_{(k)} = \frac{r_{(k)}^T r_{(k)}}{r_{(k)}^T A r_{(k)}}. \tag{3.57}$$

The update to the residual, using (3.56) and (3.55):

$$r_{(k+1)} = r_{(k)} - \alpha_{(k)} A r_{(k)}. \tag{3.58}$$

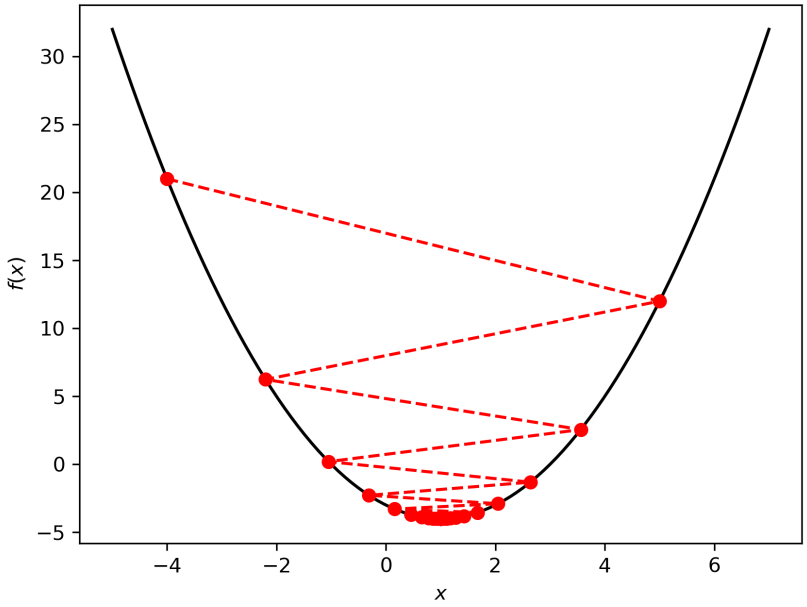

Fig. 3.4 SD search for the quadratic function $f(x) = x^2 - 2x - 3$, starting point at $x = -4$.

Equations (3.55), (3.57), (3.56) and (3.58) are run in an iterative manner until the residual meets a certain criterion. By definition of (3.55), this is to make the residual satisfactorily close to zero for a solution of $x_{(k)}$. The convergence of the SD method has been studied in great detail [149, 150, 151]. However, the practical applications of this method prove to be too slow. The assumption that the direction of the negative gradient is guaranteed to be the direction of minimisation can be misleading. A particular situation to consider is an ill-conditioned long valley as present in for example the Rosenbrock function, the zig-zag nature of the SD method as it tries to find minimum results in slow convergence. The reader is referred to [44] which demonstrates this behaviour. Figure 3.4 illustrates the application of SD to a simple quadratic function of $f(x) = x^2 - 2x - 3$, the oscillatory/zig-zag nature of the SD method is made apparent.

3.5.2 Conjugate Gradient Method

The Conjugate Gradient (CG) method aims to improve upon the step directions previously offered by the SD method. The search directions are now developed to be conjugate or A-orthogonal, two vectors $p_{(i)}$ and $p_{(j)}$ meet this requirement if

$$p_{(i)}^T A p_{(j)} = 0. \tag{3.59}$$

Usually the first iteration of any CG method begins with an SD step, that is the first search direction is set to the residual:

$$p_{(0)} = r_{(0)} = b - A x_{(0)}. \tag{3.60}$$

The scalar for the solution update α is

$$\alpha_{(k)} = \frac{r_{(k)}^T r_{(k)}}{p_{(k)}^T A p_{(k)}}. \tag{3.61}$$

The first iteration of this is equivalent to the SD scalar in equation (3.57). The solution vector is updated similarly as in (3.56):

$$x_{(k+1)} = x_{(k)} + \alpha p_{(k)}. \tag{3.62}$$

The step direction explicitly is given here for the update instead of just using the residual as in SD. The residual in CG is updated as

$$r_{(k+1)} = r_{(k)} - \alpha_{(k)} A p_{(k)}. \tag{3.63}$$

The search vector for CG has been developed to be conjugate to previous search directions using the Gram-Schmidt process, this avoids the tendency found in SD in which a step can be taken in the same direction as earlier steps. The scalar required for this new search vector is defined to be

$$\beta_{(k+1)} = \frac{r_{(k+1)}^T r_{(k+1)}}{r_{(k)}^T r_{(k)}}. \tag{3.64}$$

The search vector is updated using this scalar:

$$p_{(k+1)} = r_{(k+1)} + \beta_{(k+1)} p_{(k)}. \tag{3.65}$$

The CG method, like SD, is iterative and stops when the residual has met certain criteria. The convergence behaviour of CG has largely been understood for a number of problems [152, 153]. CG is perhaps one of the most commonly used iterative Krylov subspace methods, utilised in a diverse range of applications such as machine learning and engineering design [44].

3.5.3 Preconditioning

Before introducing preconditioning, the concept of the condition number is discussed. In general, the term condition number is associated with a measure of difficulty in solving the problem. A problem is termed to be *well conditioned* if the condition number is small and *ill conditioned* if the condition number is large. The condition number can be defined [154]:

$$\kappa(\boldsymbol{A}) = \frac{|\lambda_{\max}(\boldsymbol{A})|}{|\lambda_{\min}(\boldsymbol{A})|}, \tag{3.66}$$

where $\lambda_{\max}$ and $\lambda_{\min}$ are the maximum and minimum eigenvalues of $\boldsymbol{A}$. Within the context of the linear response Sternheimer scheme, the matrix $\boldsymbol{A}$ is the left-hand bracketed term of the Sternheimer equation shown in (3.47). Note that this includes the KS Hamiltonian, KS eigenvalues and the frequency ω. The complexities of the KS Hamiltonian are such that the condition number is not possible to directly evaluate in practice [155]. However, statistics such as the number of iterations taken to compute a solution ($\boldsymbol{x}$) can provide insight into how ill/well-conditioned the problem is.

Now the motivation behind preconditioning will be introduced. Preconditioning is a technique used to improve the condition number of a matrix. If $\boldsymbol{M}$ is also a symmetric, positive-definite matrix which approximates $\boldsymbol{A}$, then the linear system becomes:

$$\boldsymbol{M}^{-1}\boldsymbol{A}\boldsymbol{x} = \boldsymbol{M}^{-1}b, \tag{3.67}$$

where the choice of $\boldsymbol{M}$ is chosen so that it is easier to invert. The condition number changes from $\kappa(\boldsymbol{A})$ to $\kappa(\boldsymbol{M}^{-1}\boldsymbol{A})$. If the eigenvalues of $\boldsymbol{M}^{-1}\boldsymbol{A}$ are better clustered than $\boldsymbol{A}$ this speeds up the convergence of the CG method. The preconditioned conjugate gradient scheme is now presented. The first step is made in the direction of SD, for all further $(k+1)$ iterations, the residual is preconditioned as

$$z_{(k+1)} = M^{-1} r_{(k+1)}. \tag{3.68}$$

The update of α from (3.61) is now:

$$\alpha_{(k)} = \frac{r_{(k)}^T z_{(k)}}{p_{(k)}^T A p_{(k)}}. \tag{3.69}$$

The solution and residual are updated in the same manner as from (3.62) and (3.63). The search direction scalar:

$$\beta_{(k+1)} = \frac{r_{(k+1)}^T z_{(k+1)}}{r_{(k)}^T z_{(k)}}, \tag{3.70}$$

uses the preconditioned residual instead of $r_{(k+1)}$ as in (3.64). The new search direction is

$$p_{(k+1)} = z_{(k+1)} + \beta_{(k+1)} p_{(k)}. \tag{3.71}$$

The choice of $\boldsymbol{M}$ is non-trivial, in the case of the KS Hamiltonian present in the Sternheimer equation, preconditioning schemes developed by Teter *et al* [45, 156] are employed in the CASTEP package which aims to speed up convergence. The preconditioned matrix in the RTPA/TPA scheme involves the inverse kinetic energy operator. High-energy eigenstates of the Hamiltonian contain kinetic energies which lie close to the eigenvalues. By applying the inverse matrix, fewer iterations are required to converge the high kinetic energy states. Note that the iterative minimisation which was alluded to in section 2.3.6 is the preconditioned CG process. The CG method is one of the core routines in the CASTEP code used to find the electronic ground-state.

3.5.4 BiConjugate Gradient Method

The next two methods are of particular importance to the development of DFPT in this thesis. Since the KS Hamiltonian involved in the Sternheimer equation is symmetric but not hermitian (due to the $i\eta$ term), the CG method cannot be used. The BiConjugate Gradient Method (BiCG) resolves this by considering the original linear system of $\boldsymbol{Ax} = \boldsymbol{b}$ but also an adjoint linear system:

$$\hat{\boldsymbol{A}}\hat{\boldsymbol{x}} = \hat{\boldsymbol{b}}. \tag{3.72}$$

It follows now that each quantity observed in the preconditioned CG now has two sequences. The solution update for each system is expressed as

$$x_{(k+1)} = x_{(k)} + \alpha_{(k)} p_{(k)}. \tag{3.73}$$

Its adjoint:

$$\hat{x}_{(k+1)} = \hat{x}_{(k)} + \alpha^*_{(k)} \hat{p}_{(k)}. \tag{3.74}$$

The corresponding search direction for the system and its adjoint:

$$p_{(k+1)} = z_{(k+1)} + \beta_{(k)} p_{(k)}, \tag{3.75}$$

$$\hat{p}_{(k+1)} = \hat{z}_{(k+1)} + \beta^*_{(k)} \hat{p}_{(k)}, \tag{3.76}$$

where z is the preconditioned residual, again both sets are required:

$$z_{(k+1)} = M^{-1} r_{(k+1)}, \tag{3.77}$$

$$\hat{z}_{(k+1)} = M^{-1} \hat{r}_{(k+1)}. \tag{3.78}$$

The residuals for both sets are updated as

$$r_{(k+1)} = r_{(k)} - \alpha_{(k)} A p_{(k)}, \tag{3.79}$$

$$\hat{r}_{(k+1)} = \hat{r}_{(k)} - \alpha^*_{(k)} \hat{A} \hat{p}_{(k)}. \tag{3.80}$$

The systems are connected through the definition of the scalars used to update the residuals and solution vectors. The scalar for the solution vector α:

$$\alpha_{(k)} = \frac{\hat{r}^T_{(k)} z_{(k)}}{\hat{p}^T_{(k)} A p_{(k)}}. \tag{3.81}$$

The scalar used to update the residuals, β:

$$\beta_{(k+1)} = \frac{\hat{r}^T_{(k+1)} z_{(k+1)}}{\hat{r}^T_{(k)} z_{(k)}}. \tag{3.82}$$

For arrays involving complex numbers, the usage of α^* and β^* denote the complex conjugate. The BiCG method allows for the consideration of matrices that are not necessarily symmetric or hermitian (as in the case of the dielectric response). The consideration of two sequences results in double the number of matrix computations involved in the algorithm compared to the CG method.

3.5.5 BiConjugate Gradient Stabilised Method

A practical discussion will be made later regarding the convergence of the BiCG method, here, the last iterative method which will be presented is the BiConjugate Gradient Stabilised Method (BiCGStab). The motivation behind the usage of this method will become apparent in later sections regarding the dielectric response computation.

The underlying idea behind BiCGStab is to take the BiCG method and apply certain procedures to ensure the minimisation of the residual. Instead of the usual update of the residual as in the preconditioned BiCG, a vector s is now defined at every iteration:

$$s_{(k)} = r_{(k)} - \alpha_{(k)} A p_{(k)}. \tag{3.83}$$

Applying preconditioning:

$$\tilde{s}_{(k)} = M^{-1} s_{(k)}. \tag{3.84}$$

The scalar

$$w_{(k)} = \frac{(A s_{(k)})^T s_{(k)}}{(A s_{(k)})^T (A s_{(k)})}. \tag{3.85}$$

Minimises the norm of s and therefore the residual. The residual is updated as

$$r_{(k)} = s_{(k)} - w_{(k)} A \tilde{s}_{(k)}. \tag{3.86}$$

These additional variables are involved with the update of all the BiCG variables which include the residual, solution vector, search direction vector, and scalars α and β. If either the norm of s or the residual is sufficiently minimised then a solution is found. This extra step of locally minimising the residual is taken from the Generalised Minimal Residual Method (GMRES) [157]. The BiCGStab method is essentially one step of BiCG followed by one GMRES, which requires two further inner products for every iteration compared to BiCG [158]. Practical computations of the dielectric response will highlight the smoothing effect of the stabilising scalar (w) on the BiCGStab residual.

Chapter 4

Dielectric Response Spectra for Real Materials

4.1 Head of the Frequency Dependent Dielectric Matrix

Previous sections have discussed the relationship between the dielectric response and the non-interacting density function. The computation of the induced electronic density at a certain ω in the Sternheimer scheme allows for the determination of the frequency-dependent dielectric response. In order to understand the main quantity of interest in this thesis, the reciprocal space formulation is required. The wavefunction from section 2.3.1 is expressed in reciprocal space [143]:

$$\psi_{n\boldsymbol{k}}(\boldsymbol{r'}) = \sum_{\boldsymbol{G'}} e^{i(\boldsymbol{k}+\boldsymbol{G'})\cdot\boldsymbol{r'}} u_{n\boldsymbol{k}}(\boldsymbol{G'}). \tag{4.1}$$

The first-order response wavefunctions can be expressed in terms of the periodic Bloch wavevectors [136]:

$$\Delta\psi^{\pm}_{v\boldsymbol{k}[\boldsymbol{r},\omega]}(\boldsymbol{r'}) = \frac{1}{N_{\boldsymbol{q}}} \sum_{\boldsymbol{q}\boldsymbol{G}\boldsymbol{G'}} e^{-i(\boldsymbol{q}+\boldsymbol{G})\cdot\boldsymbol{r}} e^{-i(\boldsymbol{k}+\boldsymbol{q}+\boldsymbol{G'})\cdot\boldsymbol{r'}} \Delta u^{\pm}_{v\boldsymbol{k}[\boldsymbol{q},\boldsymbol{G},\omega]}(\boldsymbol{G'}). \tag{4.2}$$

The $\boldsymbol{k}$ and $\boldsymbol{k}+\boldsymbol{q}$ present in the exponential terms are due to the conservation of crystal momentum present in the Sternheimer equation [110, 136]. The reciprocal space formulation of the Sternheimer equation is

$$(\hat{H}_{\boldsymbol{k}+\boldsymbol{q}} - \varepsilon_{v\boldsymbol{k}} \pm \omega + i\eta)\Delta u^{\pm}_{v\boldsymbol{k}[\boldsymbol{q},\boldsymbol{G}]} = -(1 - \hat{P}^{\boldsymbol{k}+\boldsymbol{q}}_{occ})v_{[\boldsymbol{q},\boldsymbol{G},\omega]}u_{v\boldsymbol{k}}, \tag{4.3}$$

where $\hat{H}_{\boldsymbol{k}} = e^{-i\boldsymbol{k}\cdot\boldsymbol{r}}\hat{H}e^{i\boldsymbol{k}\cdot\boldsymbol{r}}$, the projected single-particle Hamiltonian and $\hat{P}^{\boldsymbol{k}}_{occ} = \sum_v |u_{v\boldsymbol{k}}\rangle \langle u_{v\boldsymbol{k}}|$ is the projector over occupied states. The Sternheimer equation is solved for every $\boldsymbol{k}, \boldsymbol{q}, \boldsymbol{G}$ and ω utilising the iterative numerical methods discussed previously. The solutions at $\pm\omega$ are used to construct the induced density matrix:

$$\Delta n_{[\boldsymbol{q},\boldsymbol{G},\omega]}(\boldsymbol{G}') = \frac{2}{N_{\boldsymbol{k}}}\sum_{v\boldsymbol{k}} u^{*}_{v\boldsymbol{k}}(\boldsymbol{G}')\left(\Delta u^{+}_{v[\boldsymbol{k}+\boldsymbol{q},\boldsymbol{G},\omega]}(\boldsymbol{G}') + \Delta u^{-}_{v[\boldsymbol{k}+\boldsymbol{q},\boldsymbol{G},\omega]}(\boldsymbol{G}')\right). \tag{4.4}$$

The dielectric response in reciprocal space:

$$\varepsilon_{[\boldsymbol{q},\boldsymbol{G},\omega]}(\boldsymbol{G}') = \delta_{\boldsymbol{G},\boldsymbol{G}'} - \Delta n_{[\boldsymbol{q},\boldsymbol{G},\omega]}(\boldsymbol{G}'). \tag{4.5}$$

The induced density matrix computed at a perturbing $\boldsymbol{q}$, $\boldsymbol{G}$ and ω yield a row in $\boldsymbol{G}'$ of the frequency-dependent dielectric matrix. The dielectric response implementation developed in this thesis involves calculating the frequency (ω) along the *real* axis with a small imaginary component ($i\eta$). Work by Andrade and co-workers has shown that this imaginary component is required in order to reach a stable solution in the Sternheimer scheme [76, 80]. In section 3.3, the infinitesimal included in the definition of the first-order response orbitals gives some Lorentzian width to the otherwise delta function pole, avoiding numerical issues arising from a singular matrix [63].

It is also mentioned briefly that another approach commonly seen in GW implementations where the screened Coulomb interaction is of principal interest is to calculate the response for a frequency along the imaginary axis and then analytically continue to the real axis. Here, no η is required, avoiding the ill-conditioning of the $\boldsymbol{A}$ matrix which would occur due to the singularities if $\omega = \varepsilon_v$. The analytic continuation requires the use of further approximations in order to correctly reproduce the shape of the dielectric response. Work by Giustino and others have discussed the benefits of this approach with respect to speed and numerical stability in the self-consistent Sternheimer scheme [136, 143, 144].

A perturbing $\boldsymbol{q}$-vector and $\boldsymbol{G}$ defines the bare Coulomb interaction v in (4.3). The solution in the Sternheimer scheme yields the first row in $\boldsymbol{G}'$ of the dielectric matrix:

$$\varepsilon_{\boldsymbol{G},\boldsymbol{G}'} = \begin{pmatrix} \varepsilon_{\boldsymbol{G}=0,\boldsymbol{G}'=0} & \cdots & \varepsilon_{\boldsymbol{G}=0,\boldsymbol{G}'} \\ \vdots & \ddots & \vdots \\ \varepsilon_{\boldsymbol{G},\boldsymbol{G}'=0} & \cdots & \varepsilon_{\boldsymbol{G},\boldsymbol{G}'} \end{pmatrix}. \tag{4.6}$$

The computation of the screened Coulomb potential would require computations for all $\boldsymbol{G}$ perturbing potentials. The resulting matrix is then inverted and the screened interaction is computed from equation (3.25).

All results presented in this thesis correspond to the *head* of the frequency-dependent dielectric matrix at *long-wavelength*. The *head* denotes that the perturbing reciprocal lattice vector and the reciprocal component of the dielectric matrix which is extracted are the same and equal to zero ($\boldsymbol{G} = \boldsymbol{G}' = 0$). The *long-wavelength* denotes that $\boldsymbol{q} \to 0$, in practice, all computations of the dielectric response presented in this thesis use the following (expressed in fractional coordinates): $[\boldsymbol{q} = (0.01,\ 0.0,\ 0.0)]$. The bare Coulomb interaction in (4.3) has the following representation in reciprocal space:

$$v(\boldsymbol{r},\boldsymbol{r}') = \frac{1}{N_{\boldsymbol{q}}} \sum_{\boldsymbol{q}\boldsymbol{G}} v(\boldsymbol{q}+\boldsymbol{G}) e^{i(\boldsymbol{q}+\boldsymbol{G})\cdot(\boldsymbol{r}'-\boldsymbol{r})}, \tag{4.7}$$

where,

$$v(\boldsymbol{q}+\boldsymbol{G}) = \frac{4\pi}{|\boldsymbol{q}+\boldsymbol{G}|^2}. \tag{4.8}$$

The parameters involved in the computation of the *head* of the dielectric matrix would result in a singularity in the term in (4.8). Instead, a plane-wave perturbation is considered:

$$v(\boldsymbol{G}')_{[\boldsymbol{G}]} = \delta_{\boldsymbol{G}\boldsymbol{G}'}. \tag{4.9}$$

4.2 Dielectric Response Implementation

The implementation for the dielectric response implemented in the CASTEP package will now be discussed. The first step requires the computation of the self-consistent ground-state (GS) electronic density. The plane-wave coefficients at both $\boldsymbol{k}$ and $\boldsymbol{k}+\boldsymbol{q}$ are then required for the GS $u_{\boldsymbol{k}}, u_{\boldsymbol{k}+\boldsymbol{q}}$ terms present in the Sternheimer scheme. The BiCG/BiCGStab algorithms are used to determine the two first-order response wavefunctions at a *real* $\pm\omega$ with a small

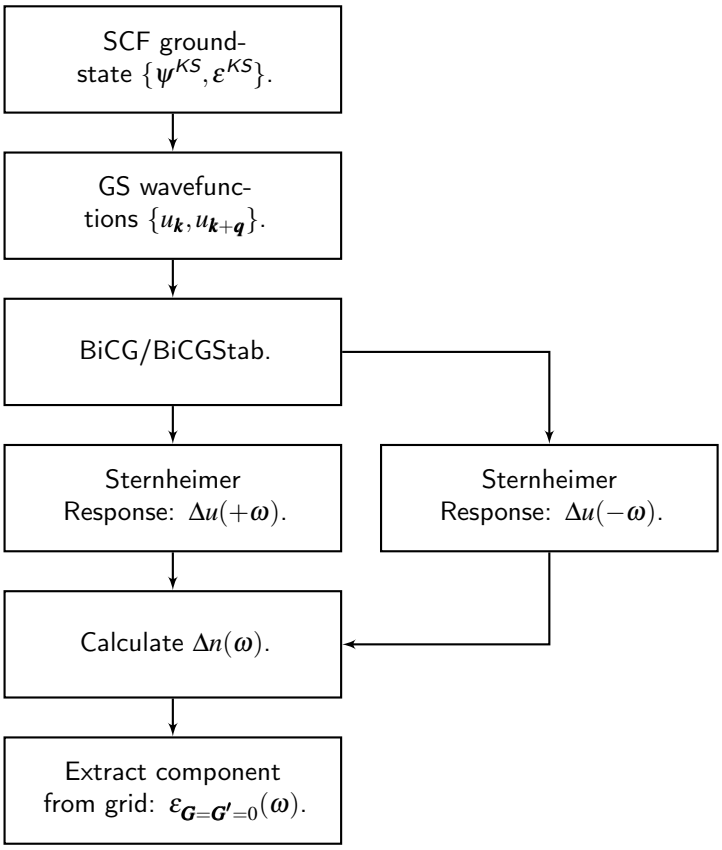

Fig. 4.1 Flow-chart of the implementation developed in CASTEP used to determine the dielectric response.

imaginary η component. The response density is then computed after which the head ($\boldsymbol{G} = \boldsymbol{G}' = 0$) of the dielectric matrix can be extracted. The flowchart of 4.1 presents the implementation.

The degree of convergence of the GS electronic density must be achieved to a fine tolerance. Practical DFPT implementations of other properties such as phonons have shown that errors in the GS propagate approximately in a quadratic manner to the response quantities [159, 160]. This can be seen by the definition of the first-order response density in (4.4) and by the projection operator. If a suitably converged GS density is not found, the errors in the GS wavefunctions not only propagate to the solution of the first-order response wavefunctions but by definition, also to the induced response density which directly affects the dielectric response.

Further attention will now be taken into the usage of iterative Krylov Subspace solvers. Both BiCG and BiCGStab methods will be discussed.

4.3 Method for the Sternheimer Solver

This section will focus on the Sternheimer solver used to obtain the first-order response wavefunctions that constitute the dielectric response.

4.3.1 Breakdown of BiCG

This section will discuss the usage of the BiConjugate Gradient (BiCG) algorithm in obtaining the first-order response wavefunctions. The preconditioned BiCG algorithm is presented in algorithm 1:

Algorithm 1 The Preconditioned BiConjugate Gradient Method

for $k = 1, 2, \cdots$ **do**
  $z_{(k-1)} = M^{-1} r_{(k-1)}$
  $\hat{z}_{(k-1)} = M^{-1} \hat{r}_{(k-1)}$
  $\rho_{(k-1)} = z_{(k-1)} \hat{r}_{(k-1)}$
  if $k = 1$ **then**
    $p_{(k)} = z_{(k)}$
    $\hat{p}_{(k)} = \hat{z}_{(k)}$
  else
    $\beta_{(k-1)} = \rho_{(k-1)} / \rho_{(k-2)}$
    $p_{(k)} = z_{(k-1)} + \beta_{(k-1)} p_{(k-1)}$
    $\hat{p}_{(k)} = \hat{z}_{(k-1)} + \beta^*_{(k-1)} \hat{p}_{(k-1)}$
  end if
  $\alpha_{(k)} = \rho_{(k-1)} / \hat{p}_{(k)} A p_{(k)}$
  $x_{(k)} = x_{(k-1)} + \alpha_{(k)} p_{(k)}$
  $r_{(k)} = r_{(k-1)} - \alpha_{(k)} A p_{(k)}$
  $\hat{r}_{(k)} = \hat{r}_{(k-1)} - \alpha_{(k)} \hat{A} \hat{p}_{(k)}$
  ▷ Check convergence of the residual, continue if necessary
end for

Recall that the requirement for the algorithm to exit is if the residual is sufficiently close to zero. In CASTEP, the residual is defined as an object that contains an array of plane-wave coefficients for a group of electronic bands at a single k-point. The term used to denote this in the CASTEP package is a *wavefunction slice*. The dot product of the residual with itself is taken to provide a single macroscopic measure which is termed as the *residual norm* or *r_norm*. It is shown in section 4.4.3 that a sufficient tolerance factor must be used in order to obtain accurate dielectric spectra. During each iteration, the residual norm of each electronic band is evaluated against the predefined tolerance. The computation of the

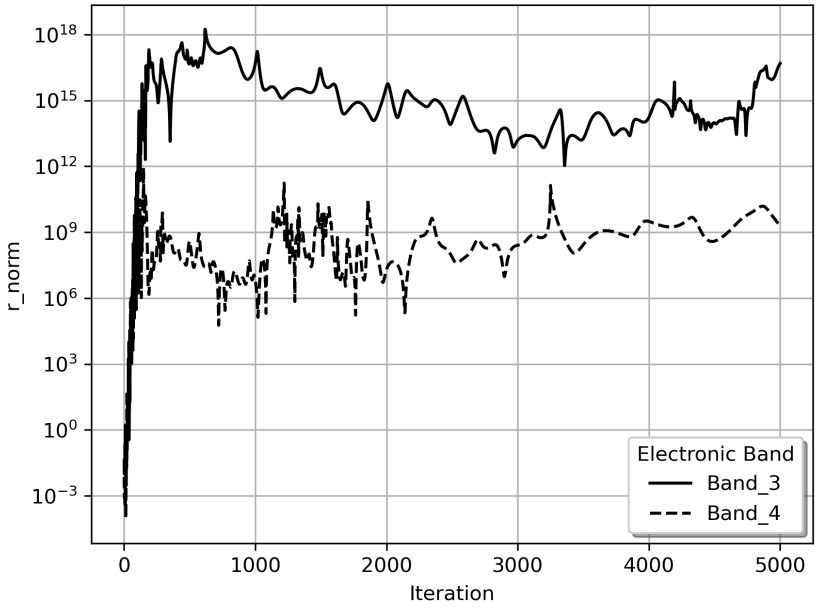

Fig. 4.2 Plot of the residual norm against iteration number using the BiCG method.

response wavefunction is triggered only when this residual norm reaches the user-defined tolerance for *all* electronic bands. Figure 4.2 presents the values of the residual norm for two of the electronic bands present in the prototypical Si calculation. The other 2 bands (not shown) meet the residual norm criteria for convergence. A logarithmic scale is used for the $y-$scale to plot the residual norm at every iteration. The residual is shown to explode, resulting in a failure in computing the dielectric response.

Looking more closely at the first 30 iterations in figure 4.3, it shows that although there is some fluctuation, the overall behaviour of r_norm for both bands is to increase. The tolerance factor used for this calculation is $1e-2$, it is observed that although band_3 satisfies the criteria, band_4 does not. At iteration 16, the r_norm of band_4 meets the threshold however now band_3 does not.

In order to attempt to resolve this issue, it was explored to forgo the band_blocking of the solver to instead minimise the residual band-by-band. However this was only able to provide a solution for some k-points, the inconsistent behaviour was found to persist in computations at other k-points and a tolerance factor of $1e-2$ was not met (see section 4.4.3 for this implication). Furthermore, forgoing band_blocking was shown to provide an inefficient use of computational resources. This is because now for every iteration, the Hamiltonian is

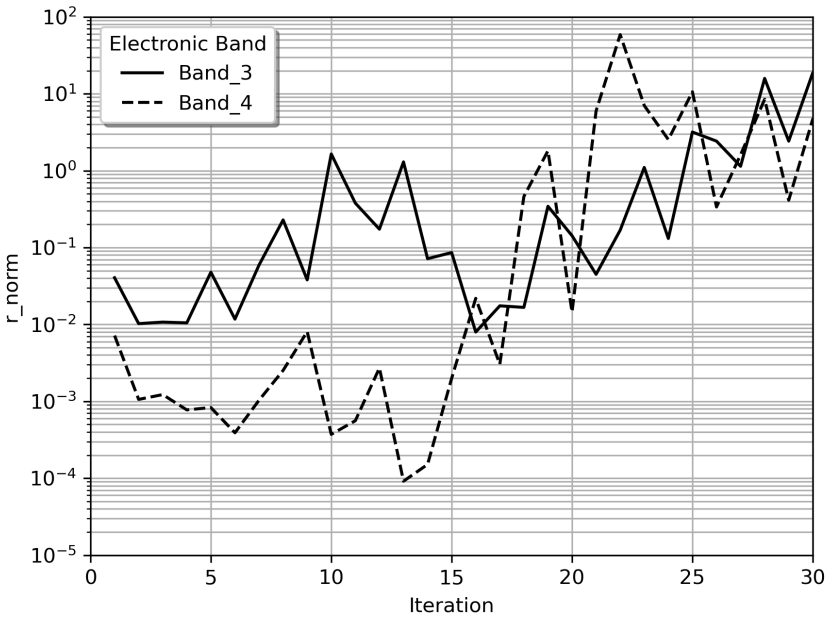

Fig. 4.3 Plot of the residual norm for the first 30 iterations using the BiCG method.

initialised and applied (band-by-band) to a single component of the wavefunction slice. This would also mean there would be no potential to make use of band parallelism [161].

The BiCG algorithm breaks down if $\hat{p}_{(k)}Ap_{(k)} = 0$, this is known as *pivotal breakdown* [162]. The condition of $\rho_k = 0$ leads to a breakdown in the process used to determine the subspace of orthogonal bases necessary for the BiCG procedure. This is referred to in the literature as a breakdown in the underlying Lanczos process [163]. The variables associated with these breakdown conditions are now investigated.

Figures 4.4 and 4.5 illustrate the components of the scalars; ρ_k and $\hat{p}_{(k)}Ap_{(k)}$. It is shown that the pivot breakdown condition is indeed met which manifests in the erratic convergence behaviour. Multiple tests of the preconditioned BiCG procedure for Si and other systems at different k-points have been carried out. All have resulted in the erratic behaviour of the residual as shown in figure 4.2.

This erratic convergence behaviour of the residual has been seen before in literature, and several procedures have been developed to avoid breakdown. The pivot breakdown of ($\hat{p}_{(k)}Ap_{(k)} = 0$), results in $\alpha_{(k)}$ becoming numerically questionable which in turn would make the solution vector inaccurate. A common technique is to instead restart the iterative loop with a Steepest Descent step in which $p_{(k)} = z_{(k)}$ and $\hat{p}_{(k)} = \hat{z}_{(k)}$. This did not improve the

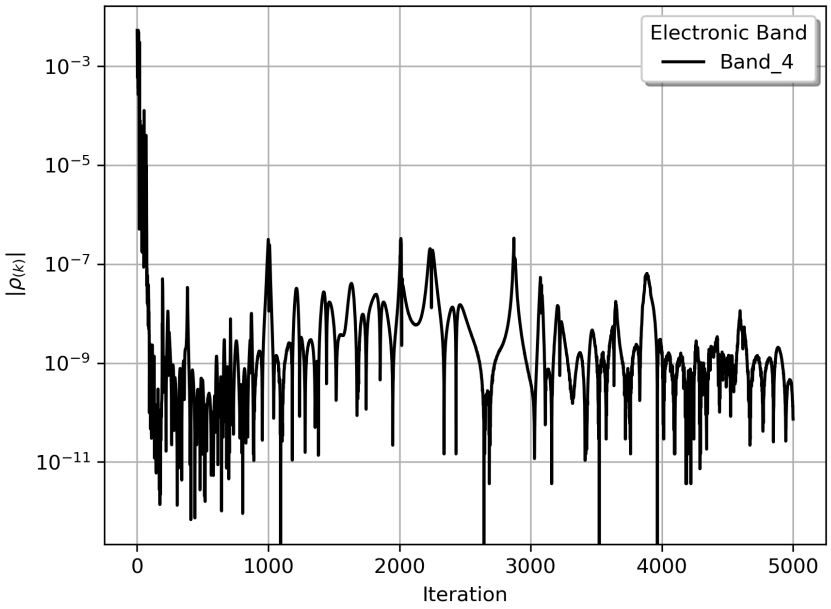

Fig. 4.4 Plot of $\rho_{(k)}$ using the BiCG method.

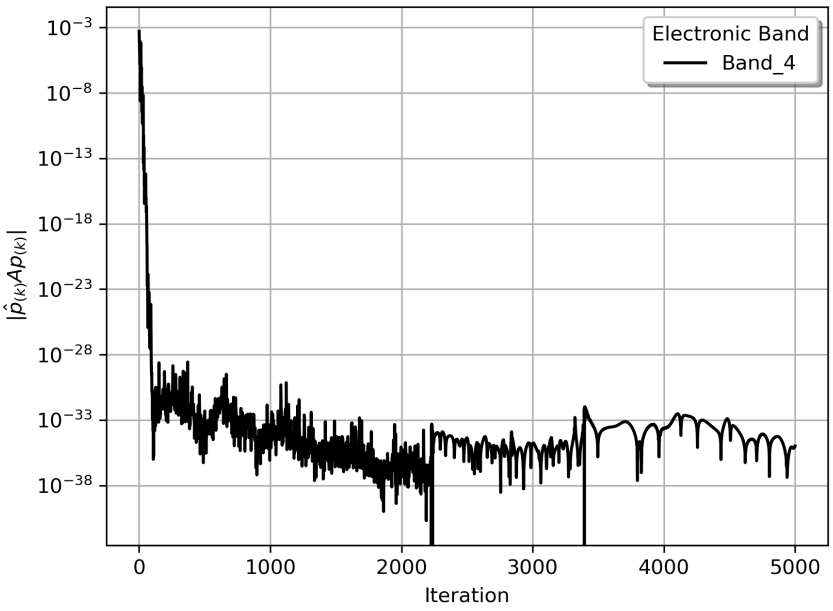

Fig. 4.5 Plot of $\hat{p}_{(k)}Ap_{(k)}$ using the BiCG method. In comparison to figure 4.4, the component is effectively zero.

convergence behaviour for this DFPT implementation but has shown success in conjugate gradient ground-state computations [45, 164].

Addressing the breakdown in the Lanczos process has led to the development of 'look-ahead' strategies [165]. The idea is to skip steps in which breakdown or near-breakdown would occur in the standard process. This is beyond the scope of work considered here, however, the reader is referred to [157, 165, 166, 167].

It is now prudent to consider alternative methods that offer a balance of numerical stability and fast convergence. The *conjugate gradient square* (CGS) method was considered for its fast convergence properties [168], however, it inherits the breakdown conditions of BiCG. The GMRES scheme mentioned in section 3.5.4 requires the storage of all previous vectors and hence demands unfeasible memory and computational resources. The route taken in this work is to employ the BiCGStab scheme, considered to be a hybrid of BiCG and GMRES [158].

4.3.2 BiCGStab

In order to address the erratic behaviour of the residual a more robust method is employed. The BiCGStab scheme of Van der Vorst provides the means for smoother convergence behaviour [158]. The method is presented in algorithm 2.

The parameter of interest to be highlighted here is $w_{(k)}$, which is known as the stabilising parameter. The choice of $w_{(k)}$ is defined such that the Euclidean norm of the residual is minimised. The k-th residual from the BiCG method ($r_{(k)}^{\mathrm{BiCG}}$) and the residual from the BiCGStab scheme ($r_{(k)}^{\mathrm{BiCGStab}}$) are compared:

$$r_{(k)}^{\mathrm{BiCGStab}} = (I - w_{(i)}A) r_{(k)}^{\mathrm{BiCG}}, \tag{4.10}$$

where if $r_{(k)}^{\mathrm{BiCGStab}} = 0$ and $r_{(k)}^{\mathrm{BiCG}} = 0$ would indicate that both methods converged to an exact solution. It is the multiplicative term of the stabilising parameter which ensures the convergence in minimising the residual.

The smooth convergence properties of the method are highlighted here. The residual norm is plotted for the same test case of Si. The two figures of 4.6 and 4.7 illustrate the minimisation for two tolerance factors of $1e-6$ and $1e-9$ respectively. It is shown that every subsequent iterative step routinely results in a lower residual norm and this is shown to hold true for all electronic bands.

Algorithm 2 The Preconditioned BiConjugate Gradient Stabilised Method

for $k = 1, 2, \cdots$ **do**
  $\rho_{(k-1)} = \hat{r}_{(k-1)} r_{(k-1)}$
  if $k = 1$ **then**
    $p_{(k)} = r_{(k-1)}$
  else
    $\beta_{(k-1)} = \left(\rho_{(k-1)} / \rho_{(k-2)}\right) \left(\alpha_{(k-1)} / w_{(k-1)}\right)$
    $p_{(k)} = r_{(k-1)} + \beta_{(k-1)} \left(p_{(k-1)} - w_{(k-1)} v_{(k-1)}\right)$
  end if
  $\alpha_{(k)} = \rho_{(k-1)} / \hat{r}_{(k)} A (M^{-1} p_{(k)})$
  $s_{(k)} = r_{(k-1)} - \alpha_{(k)} A \hat{p}_{(k)}$
  if Norm of s is small enough **then**
    $x_{(k)} = x_{(k-1)} + \alpha_{(k)} \hat{p}_{(k)}$ and **stop**
  else
    $w_{(k)} = A(M^{-1} s_{(k)}) s_{(k)} / A(M^{-1} s_{(k)}) A(M^{-1} s_{(k)})$
    $x_{(k)} = x_{(k-1)} + \alpha_{(k)} (M^{-1} p_{(k)}) + w_{(k)} (M^{-1} s_{(k)})$
    $r_{(k)} = s_{(k)} - w_{(k)} A (M^{-1} s_{(k)})$
    ▷ Check convergence of the residual, continue if necessary
  end if
end for

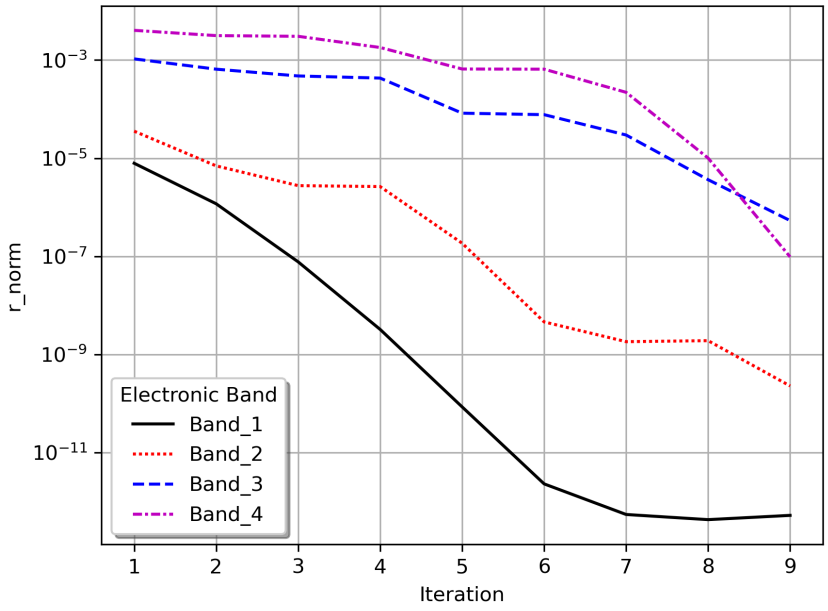

Fig. 4.6 Plot of the residual norm with a tolerance factor of $1e-6$ for all bands using the BiCGStab method.

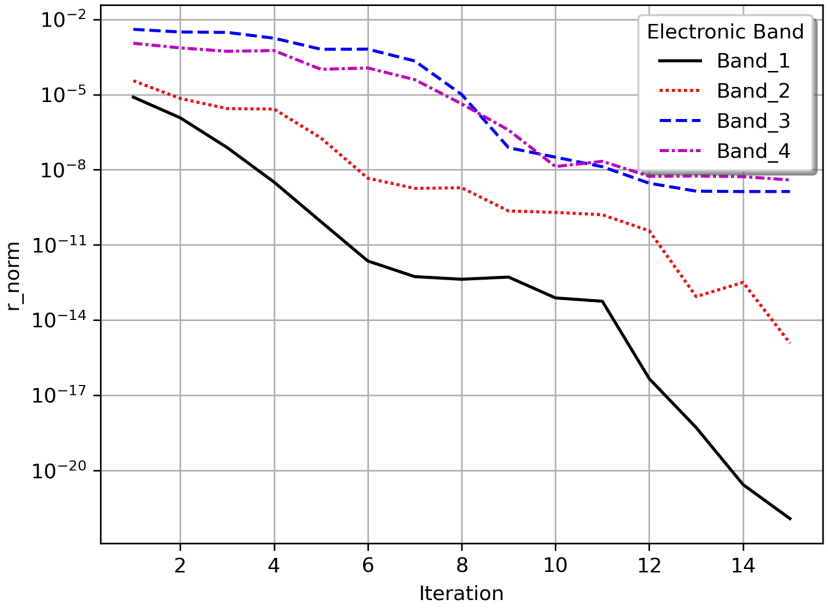

Fig. 4.7 Plot of the residual norm with a tolerance factor of $1e-9$ for all bands using the BiCGStab method.

All computational results shown in this thesis utilise the preconditioned BiCGStab method of algorithm 2 for its robustness in solving the frequency-dependent Sternheimer equation.

The table of 4.1 presents the percentage of time taken during various routines for the prototypical Si calculation using BiCGStab. As expected, the majority of time taken for the DFPT calculation ($\sim 95\%$) is with respect to the Sternheimer solver to generate the first-order response wavefunctions. Other minor routines include the self-consistent process used to obtain the ground-state electronic density and the procurement of the GS wavefunction for $\{\boldsymbol{k}, \boldsymbol{k}+\boldsymbol{q}\}$. The computation of the first-order response density shown in equation (3.44) and the application of the external potential are also relatively minor routines. Calculations for other systems show approximately the same distribution of resources, the numerical solution to the Sternheimer scheme is by far the most resource-intensive.

The dielectric response implementation has been developed to take advantage of CASTEP's parallel distribution strategy. In particular, k-point parallelism is utilised in which each processor is assigned a subset of k-points. Each processor computes the first-order response wavefunction for all electronic bands for its unique k-point subset. Equation (4.4) indicates a summation over all k-points which means that the distributed first-order plane-wave coefficients require summation in order to compute the response. Figure 4.8 shows the

Table 4.1 Time taken during various routines in the DFPT dielectric response computation of bulk-Si

Routine	% of time taken
Sternheimer Solver	95
First-Order Density	2.8
GS wavefunction $\{\boldsymbol{k}, \boldsymbol{k}+\boldsymbol{q}\}$	1
External Potential Apply	0.7
SCF GS	0.5

speedup of k-point parallelism developed within the DFPT dielectric response code. The prototypical system of Si is used with an MP grid of $\{12 \times 12 \times 12\}$ which corresponds to 864 individual k-points. The solid black line represents perfect speedup with respect to the number of CPUs.

It is also mentioned that the solver makes use of *band_blocking*. A single wavefunction slice is handled at a time which effectively means that a group of electronic bands are subjected to the BiCGStab iterative process at one time. This makes efficient use of computational resources with respect to the application of the Hamiltonian required for the $\boldsymbol{A}$ matrix.

One drawback of the BiCGStab method is the requirement to initialise and compute both $Ap_{(k)}$ and $As_{(k)}$ for every iteration. Note that this is in contrast to BiCG where only $Ap_{(k)}$ is needed. The size and complexity of the Hamiltonian make it unfeasible to store the entire array explicitly. The number of calls made to initialise, diagonalise and then apply the Hamiltonian is effectively doubled.

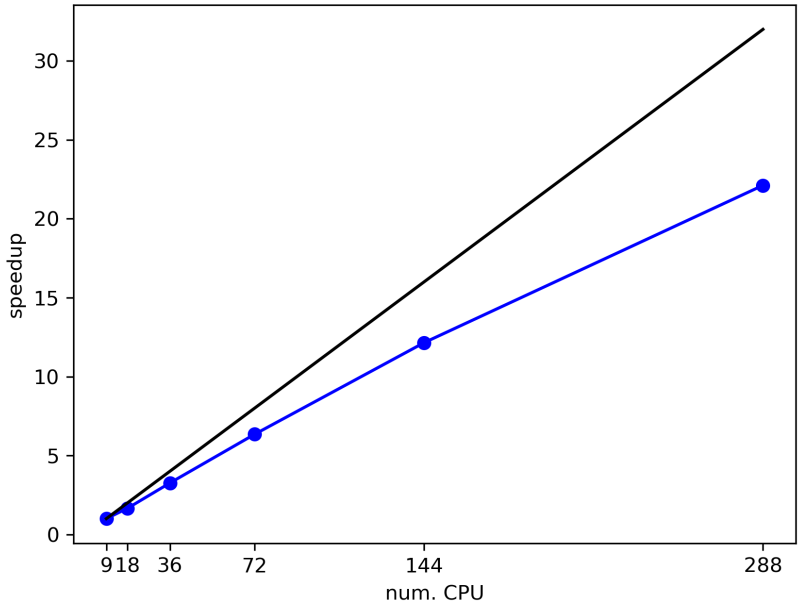

Fig. 4.8 K-point parallelism speedup of the dielectric response implementation of CASTEP.

4.4 Calculation Parameters for Dielectric Response Spectra

4.4.1 Brillouin Zone Sampling

Section 2.3.3 discussed the use of crystal symmetry to reduce the number of k-points needed to obtain an electronic density. In the DFPT dielectric response scheme, from the flowchart of 4.1, it is shown that knowledge of the wavefunction at both $\boldsymbol{k}$ and $\boldsymbol{k}+\boldsymbol{q}$ is required. The determination of the ground-state involves determining the electronic wavefunction for $\boldsymbol{k}$, in which all k-points can be restricted to the irreducible Brillouin zone. If the plane wave coefficients at some $\boldsymbol{k}+\boldsymbol{q}$ have already been determined in the ground-state calculation, then no further work is required and one can progress onto the iterative BiCG/BiCGStab method in order to determine first-order orbitals of the Sternheimer equation. The effectiveness in this reuse of ground-state plane wave coefficients is dependent on the $\boldsymbol{q}$ wavevector and k-point MP mesh employed. In this work, the response is determined specifically for a small, finite, long wavelength wavevector of $[\boldsymbol{q} = (0.01,\ 0.0,\ 0.0)]$ (expressed in fractional coordinates). Therefore, in order to use the ground-state wavefunction for the doubled kpoint set, the spacing in k-points of the MP grid must be *commensurate* with $\boldsymbol{q}$. In practice, this would require an extremely fine k-point spacing, exhausting computational resources. As such,

the implementation developed in this work does not reuse the ground-state wavefunction to determine the plane wave coefficients at $\boldsymbol{k}+\boldsymbol{q}$. This is instead done as an explicit calculation after determining the ground-state electronic density. The inclusion of high symmetry k-points such as $[\Gamma = (0,0,0)]$ may be important if the maximum or minimum of the conduction or valence band coincides with that specific point. This in turn affects the numerical precision of the KS bandgap. However, the property of interest is the dielectric response. Even if a given k-point MP set does not explicitly contain all the relevant high symmetry points affecting the bandgap, like in the forthcoming Silicon calculation, a suitably densely sampled mesh will inherently include k-points near these high symmetry points, thus providing an accurate description of band dispersion. The level of suitability is realised by performing a systematic process of adjusting the MP grid and observing a matching degree of convergence with respect to the dielectric spectra. Calculations for every system presented in this work are subject to this systematic determination and this applies to all DFT parameters.

The choice of DFT parameters used to determine the dielectric response will be analysed. Two key parameters of plane-wave DFT are the cutoff energy and reciprocal space sampling. The prototypical test case of bulk Silicon is used to illustrate the effect of these parameters with respect to the dielectric response. The Monkhorst-Pack (MP) grid is specified by three numbers which specify the number of k-points along each axis in reciprocal space [119, 120]. A finer sampling of the Brillouin zone corresponds to a larger MP grid with more k-points included in the set. This discrete set of k-points may be reduced by considering the symmetry of the crystal structure. If two or more k-points in the MP set are related by a symmetry operation, the contribution of these points to the electronic density is identical. These equivalent k-points can be sorted into a set in which a single k-point is chosen and assigned a weight. This weight is a measure of the number of equivalent k-points this single k-point represents with respect to the full MP grid. Reducing the full MP grid to this *irreducible* set of nonequivalent weighted k-points allows for the determination of the wavefunction and density using fewer operations, directly reducing computational expense.

Figures 4.9 and 4.10 show how the choice of MP grid affects the shape of the dielectric response. The significance of the peaks at certain frequencies will be discussed later, the same cutoff energy and frequency spacing is used for all curves. It is shown that the magnitude of the major peaks found in the $2-4$ eV region varies significantly at a coarse choice of k-point grid. A coarse k-point grid insufficiently describes the GS wavefunction, by definition, the response quantities are also affected resulting in large fluctuations. This can be likened to a band structure calculation in which an inadequate sampling of reciprocal space yields a poor description of the electronic state, usually presented as fluctuations similar to this dielectric picture.

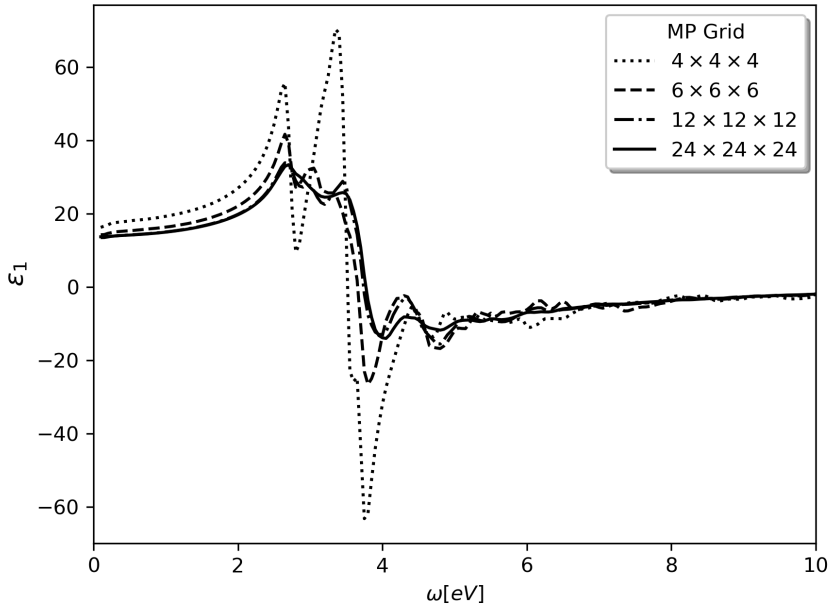

Fig. 4.9 Convergence of the Real part of the dielectric response with respect to Brillouin Zone Sampling.

It is reminded that the Sternheimer scheme in this approach involves a projection operator that includes only *occupied* states. In computing the dielectric response using the sum-over-states method [169], the convergence of the dielectric spectrum depends on the convergence of the integral involving the band dispersion of the *unoccupied* states. The aforementioned Adler-Wise formulation of equation (3.20) requires the inclusion of unoccupied states to achieve converged spectra. The band dispersion of these unoccupied states are typically more nearly-free electron-like and highly disperse, requiring the use of a dense MP grid.

4.4.2 Plane-Wave Cutoff Energy

Figures 4.11 and 4.12 illustrate the choice of the plane-wave cutoff parameter, the same frequency spacing and MP grid are used for all curves. The lower cutoff energies of 100 and 150 eV are unable to capture the magnitude of the dielectric response compared to the higher cutoff. A direct consequence of a lower cutoff is the inability to include Fourier coefficients to accurately describe the GS wavefunction. As a result, the first-order response density is insufficiently determined which in turn manifests in the shape of the dielectric response.

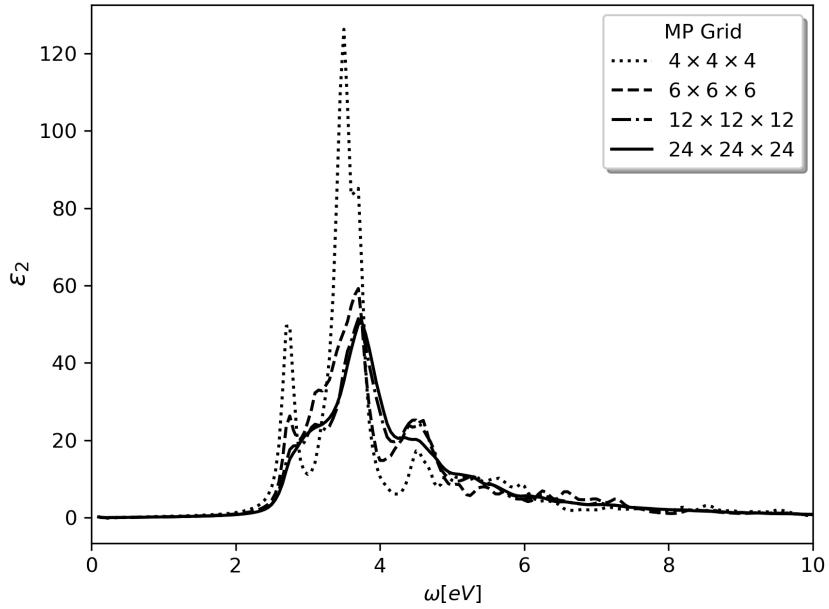

Fig. 4.10 Convergence of the Imaginary part of the dielectric response with respect to Brillouin Zone Sampling.

It is also mentioned here that the CASTEP package makes use of a second finer FFT grid to store higher-order Fourier components. For example, the charge density involves Fourier components twice the order of the wavefunction, this arises due to the product of Fourier coefficients required to obtain the density. Care must be taken to ensure that the fine grid adequately captures the higher components of the charge density. In CASTEP this is controlled by a parameter referred to as the *fine-grid scale* which sets up the fine grid through a multiplicative factor of the standard grid.

4.4.3 Residual Tolerance Factor

Another parameter of interest is the tolerance factor used to specify if the residual is satisfactorily close to zero. This is used within the iterative algorithm of the Sternheimer scheme in which the first-order wavefunction is computed for every $\pm\omega$. Figures 4.13 and 4.14 show how the choice of tolerance affects the shape of the dielectric response. For all curves here a satisfactory cutoff energy of 350 eV and an MP grid of $\{24 \times 24 \times 24\}$ are employed. The condition for the iterative solver to stop is if $[|residual - 0| < tolerance\ factor]$. The consequence of using a higher tolerance is that the stopping condition is met prematurely,

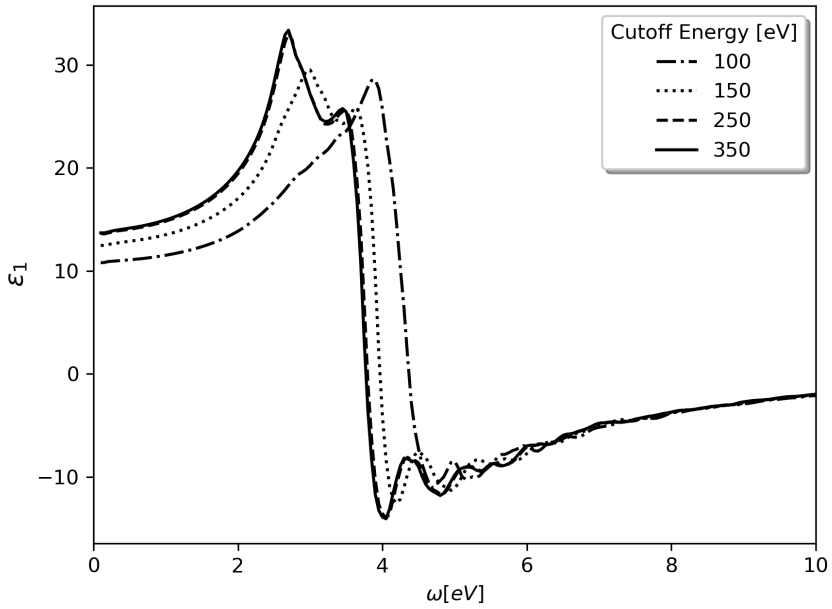

Fig. 4.11 Convergence of the Real part of the dielectric response with respect to the Plane-Wave Cutoff Energy.

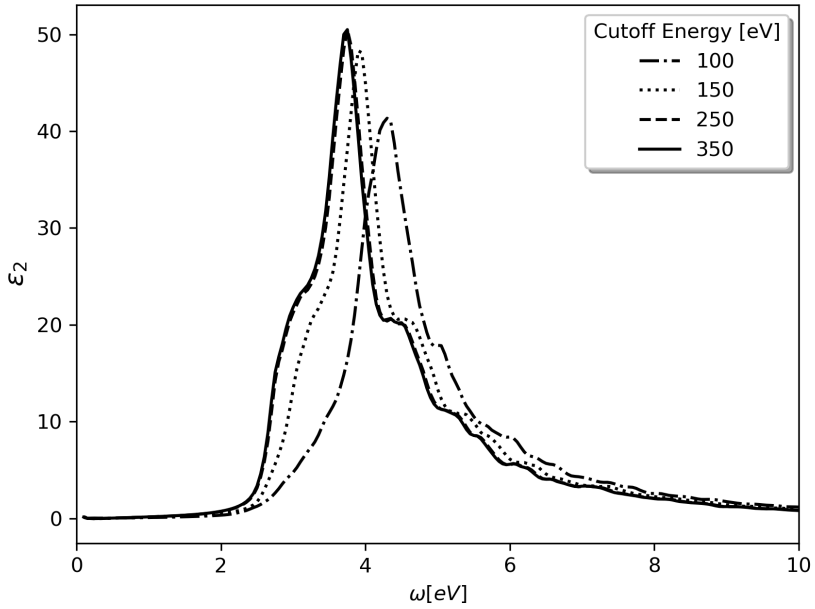

Fig. 4.12 Convergence of the Imaginary part of the dielectric response with respect to Plane-Wave Cutoff Energy.

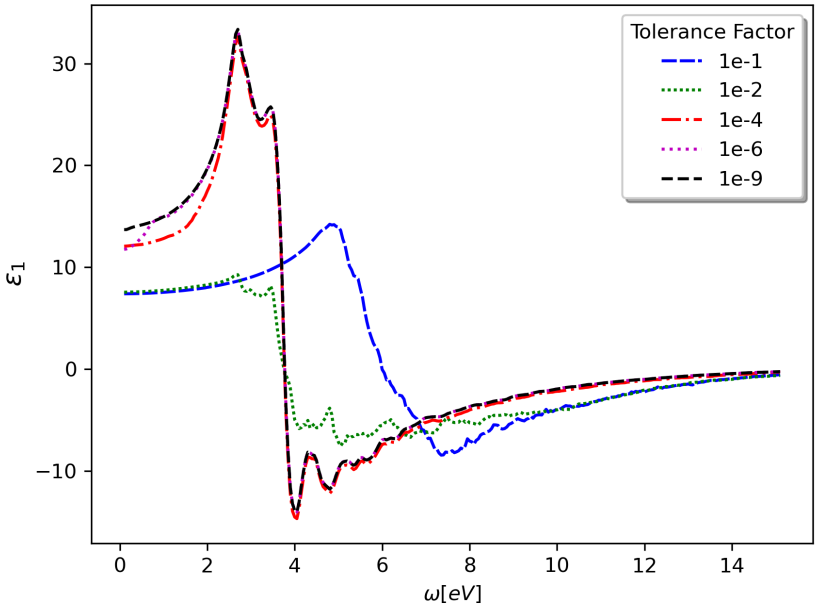

Fig. 4.13 Convergence of the Real part of the dielectric response with respect to the tolerance factor used in the Sternheimer Solver.

resulting in numerically inaccurate plane-wave coefficients for the response wavefunctions. Given that the dielectric response is dependent on the response density, which is itself determined by the multiplicative factor of both the ground-state and response wavefunctions, this has a direct impact. The higher tolerance curves of figures 4.13 and 4.14 in which inaccurate response wavefunctions are computed fail to reproduce an accurate dielectric response shape. Note that this is despite using the DFT parameters which correspond to the well-converged, self-consistent ground-state as shown previously.

4.4.4 Imaginary Component

Figures 4.15 and 4.16 demonstrate how the imaginary component of the frequency affects the dielectric response shape. Higher components of η fail to reproduce the peak of the dielectric response. Expectantly, with increasing values of η, there is increased broadening at the response peaks of the computed spectra. For all computations of the dielectric response, an imaginary η component of 0.1 eV is employed.

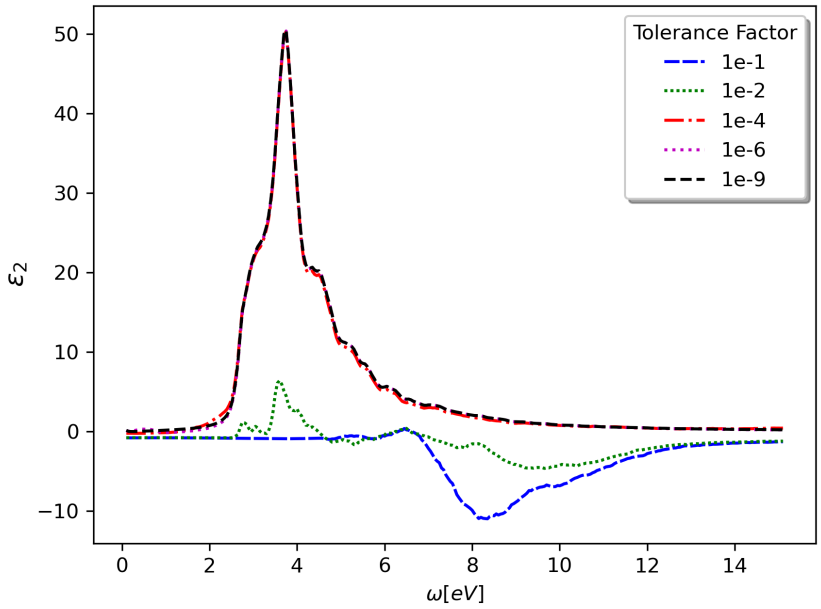

Fig. 4.14 Convergence of the Imaginary part of the dielectric response with respect to the tolerance factor used in the Sternheimer Solver.

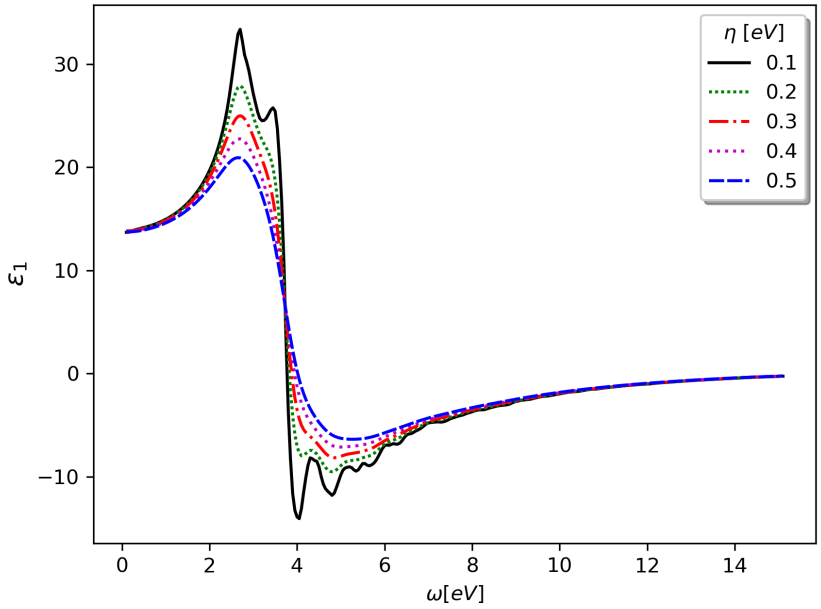

Fig. 4.15 Convergence of the Real part of the dielectric response with respect to the imaginary component η.

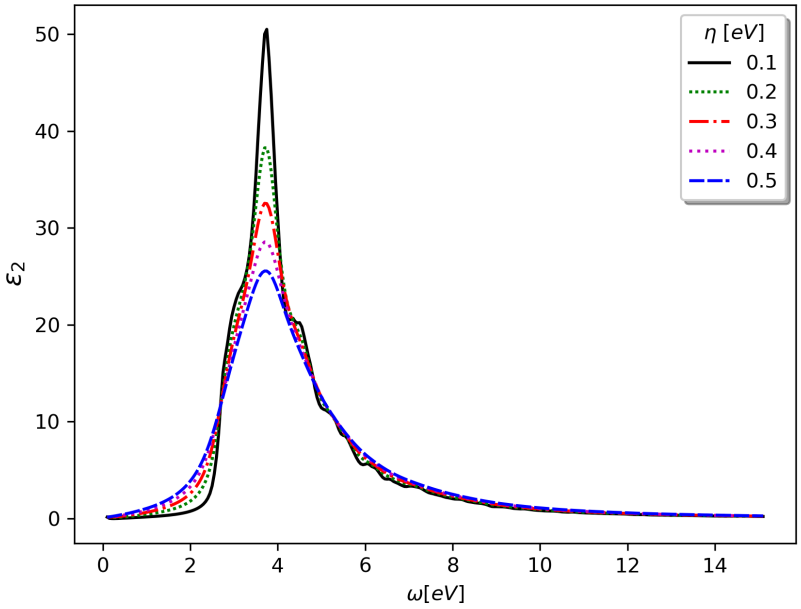

Fig. 4.16 Convergence of the Imaginary part of the dielectric response with respect to the imaginary component η.

4.4.5 Average Number of Iterations

Here, the number of numerical solver iterations with respect to frequency is considered. For the first single k-point at $+\omega$, the number of iterations taken to appropriately minimise the residual for all electronic states is stored and denoted as $\tau(\boldsymbol{k}_1, \omega)$. After completing the loop over k-points and obtaining the response wavefunction at $+\omega$, the iterative steps are averaged by dividing by the total number of k-points N_k. This statistic provides a macroscopic measure of the computational resource utilised. Since the Sternheimer solver must be solved for both $\pm\omega$, the same procedure is done whilst computing the response wavefunction at $-\omega$. The figure plotted is the combined number of average iterations for both $\pm\omega$:

$$\tau(\omega) = \left(\frac{(\tau(\boldsymbol{k}_{(1)}, +\omega) + \cdots + \tau(\boldsymbol{k}_{(N_k-1)}, +\omega)}{N_k}\right) + \left(\frac{(\tau(\boldsymbol{k}_{(1)}, -\omega) + \cdots + \tau(\boldsymbol{k}_{(N_k-1)}, -\omega)}{N_k}\right). \tag{4.11}$$

Figure 4.17 is $\tau(\omega)$ for the prototypical system of Si with $\eta = 0.1$ eV, a cutoff energy of 350 eV and an MP grid of $\{24 \times 24 \times 24\}$. The overall trend shows that with increasing frequency, a higher number of solver iterations are required to adequately minimise the

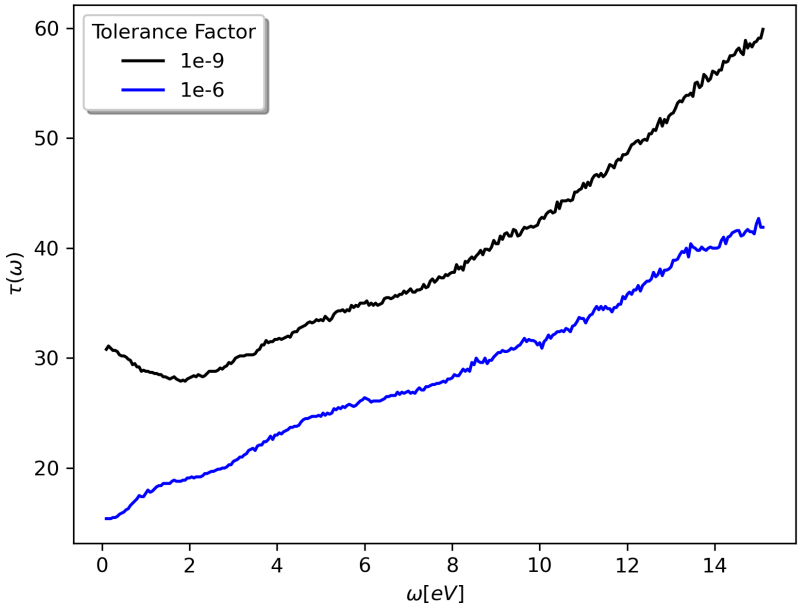

Fig. 4.17 The average number of iterations required to reach a solution, plotted for two tolerance factors, 0.05 eV frequency spacing.

residual. This holds true for both of the tolerance factors tested. Recall that the condition number is not directly accessible for the KS Hamiltonian and the only variable of change is that of the frequency. It could be suggested that higher frequency components have the effect of increasing the condition number of the $\boldsymbol{A}$ matrix, the left-hand side of the Sternheimer equation. This is evidenced by the higher number of iterations needed to obtain the response wavefunction.

4.4.6 XC Kernel

The NSCF implementation for the dielectric response involves a one-off computation of the induced charge density and its associated KS potential. Recall that the KS potential contains an XC contribution in addition to the Hartree and external potentials. The formulation of the induced charge density is within the RPA and thus there is little (if any) consequence on the choice of XC functional on dielectric spectra. It should be noted however that the dielectric response is based on the ground-state (band structure) calculation in which an XC functional is used to determine the ground-state orbitals and KS eigenvalues.

Testing for various systems has shown marginal improvement of dielectric spectra with respect to experiment when using the Generalised Gradient Approximation (GGA) functional of PBE formulated by Perdew *et al* [101] in comparison to the customary LDA. It is noted however that both LDA and PBE functionals suffer from the derivative discontinuity issues which relate to the bandgap. Other than the system of bulk Silicon, the computation of all other spectra make use of the PBE functional, since it yields a slightly better description of the ground-state.

4.5 Silicon

Silicon (Si) is an indirect bandgap semiconductor with an experimental bandgap of 1.17 eV which DFT-LDA underestimates to 0.45 eV [129]. The system used in these calculations consists of two Si atoms within the unit cell with a lattice parameter of 5.4 Angstroms. The band structure is shown in figure 4.18 in which three potential transitions are indicated. Figures 4.19 and 4.20 show the real and imaginary parts of the frequency-dependent dielectric response plotted along with experimental spectroscopic ellipsometry data from Lautenschlager *et al* [169, 170]. The three indications shown in the band structure are directly related to the three peaks (labelled E_1, E_2, E_3) found in the imaginary part of the response. The shift of E_2 and E_3 peaks found here is due to a discrepancy in determining the ground-state which is shown in the underestimation of the bandgap present in DFT-LDA calculations. Since the dielectric response is built upon the KS ground-state wavefunction and eigenvalues, this issue is commonly resolved by implementing an empirical shift of the unoccupied bands. This is known as the *scissor correction* and constitutes an additional level of approximation [171, 172]. This is not implemented here as it strays away from the underlying philosophy of *ab initio* calculations.

The failure to reproduce E_1 is due to electron-hole interactions which the Sternheimer DFPT method does not take into account. The hole left by the electron excitation brings about electrostatic forces responsible for the first peak in the experimental data. To address this problem, computational work in the field has led to the development of solving the Bethe-Salpeter equation (BSE). The BSE formalism involves two-particle Green's function and is able to incorporate excitonic effects. Naturally, the quantities involved in BSE are of higher complexity than that of the non-interacting density response function used to determine the dielectric function. BSE is commonly implemented with GW and has been successful in reproducing the experimental peaks due to electron-hole interactions in semiconductors [169, 173]. The reader is referred to [174] for a more comprehensive review of the subject.

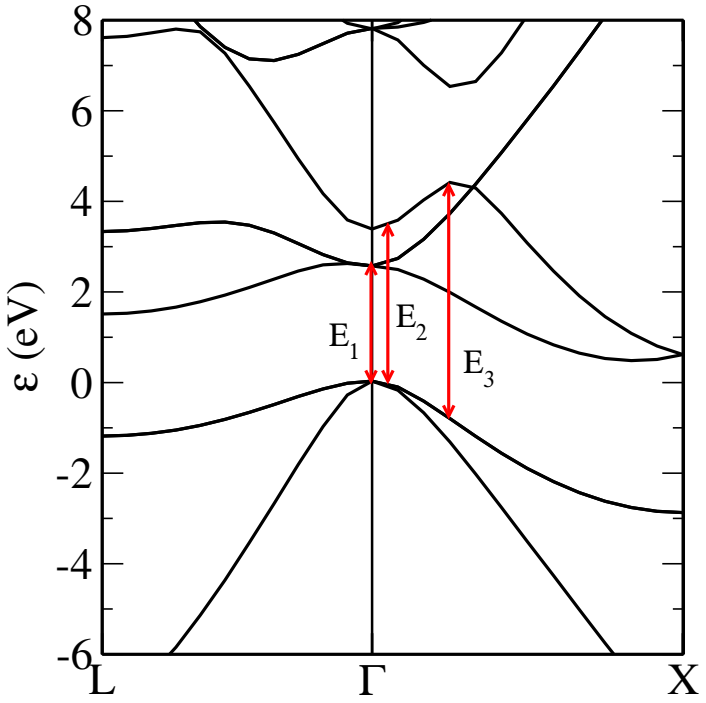

Fig. 4.18 Band structure of Si plotted along high symmetry points.

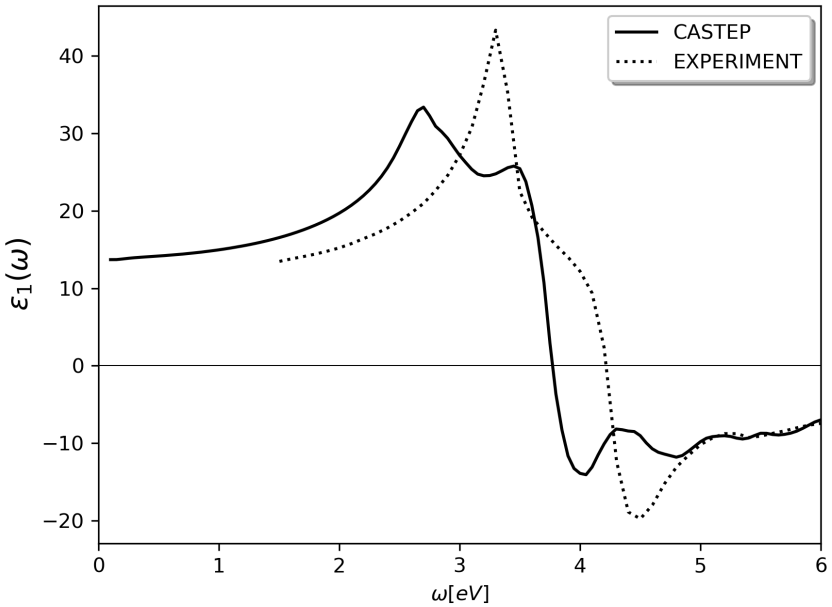

Fig. 4.19 Real component of the dielectric response for Si, spectroscopic ellipsometry data from Lautenschlager *et al* [170] .

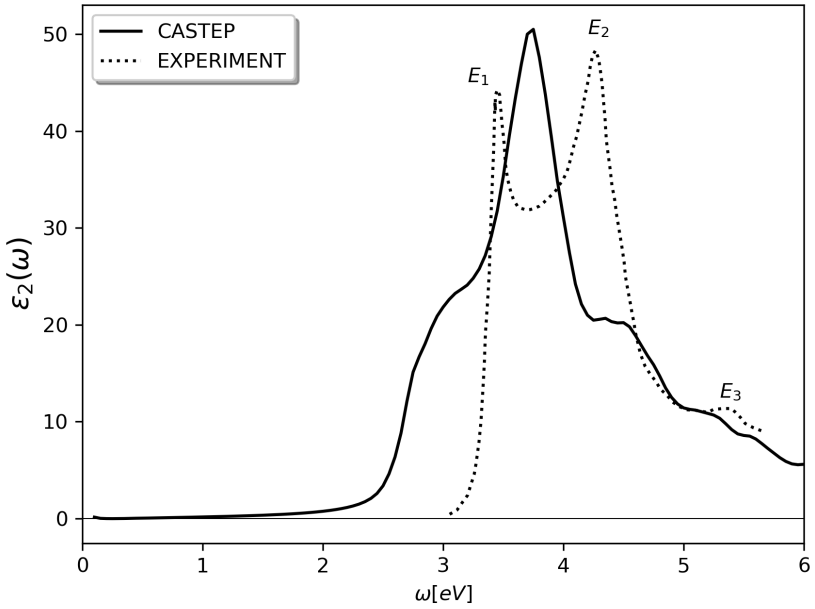

Fig. 4.20 Imaginary component of the dielectric response for Si, spectroscopic ellipsometry data from Lautenschlager *et al* [170].

A similar picture is shown to hold for the other systems, each of which will be discussed in turn. The term used to describe a shift of peaks to the left with respect to ω is *red-shift*. Results for other spectra will show almost a consistent red-shift with respect to experimental data. The term *shoulder* will be used to describe the very slight deviance found before or after a peak.

Figure 4.21 compares the DFPT implementation of this thesis which is developed in CASTEP to that of another plane-wave DFT code in Quantum Espresso's SternheimerGW (SGW) package [175]. The underlying theory is equivalent in that the dielectric response is computed using the NSCF Sternheimer GW method. However, unlike BiCG/BiCGStab the iterative algorithm used in the SGW implementation is the shifted BiCG method [176]. The norm-conserving pseudopotentials are generated by each code's respective libraries. Suitable plane-wave cutoffs and similar samplings of the Brillouin Zone are used as well as the LDA XC functional. The CASTEP implementation used 32000 k-points with SGW utilising 27648, the small fluctuations shown in parts of the response can be attributed to this. Nevertheless, the code implementations are in excellent agreement, for both real and imaginary parts of the response.

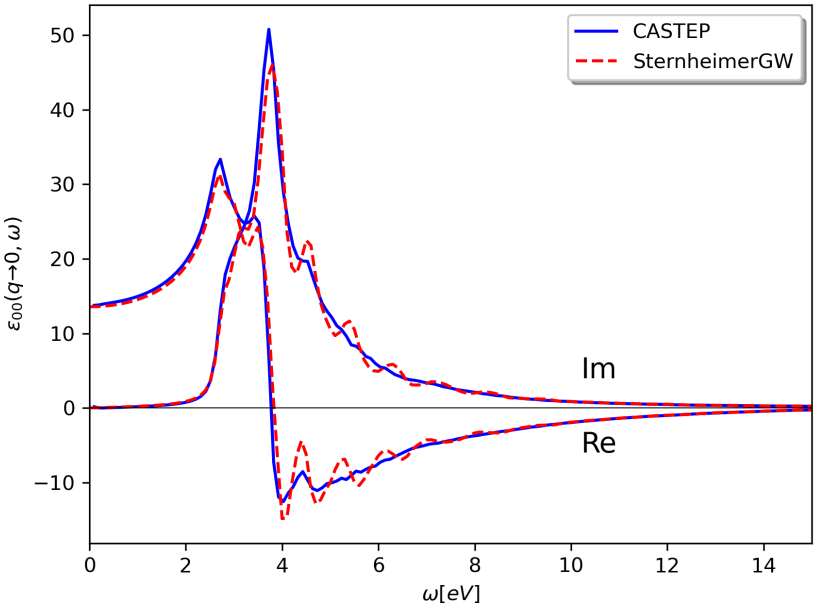

Fig. 4.21 Comparison of the CASTEP implementation with SGW, both real and imaginary parts of the response for Si are plotted.

4.6 Galium Arsenide

Galium Arsenide (GaAs) is a semiconductor that exhibits a direct bandgap, the band structure is shown in figure 4.22. Like Si, GaAs has seen use in a number of technological applications such as opto-electronics [177]. Figure 4.22 indicates several inter-band transitions, each of which is responsible for various features exhibited in the dielectric response.

The DFT computational parameters involve a plane-wave cutoff of 1000 eV and an MP grid of 30 $\times$ 30 $\times$ 30. A dense Brillouin Zone sampling was utilised in order to reduce the noise found at coarser samplings. Convergence tests for this system have shown that qualitatively, coarser MP grids would produce the overall shape of the dielectric response but with some additional noise in the form of small fluctuations, in a similar manner to the figure of 4.21. The norm-conserving pseudopotentials used for the computation have been generated from the Open-source Pseudopotential Interface / Unification Module (OPIUM) package [178]. The real and imaginary parts of the spectra are plotted with experimental data from Lautenschlager *et al* [179].

The direct bandgap transition of E_1 is featured in the imaginary part of the dielectric spectra. From the band structure of figure 4.22, the bandgap is approximately 0.7 eV, consequently,

this frequency marks the onset of the imaginary part of the dielectric spectra ε_2 as shown in figure 4.24.

The transition at E_3 situated along the $\Gamma - L$ line is represented by a peak in ε_2 at $\omega \approx 2.5$ eV after which there is a shoulder. The peak is red-shifted with respect to experimental data which indicates two distinct peaks, this is due to transitions from the light-hole and heavy-hole bands which should be present along the $\Gamma - L$ line. However spin-orbit coupling is not considered here which would require incorporating fully relativistic pseudopotentials. Therefore the splitting of the valence band is not exhibited in the DFT band structure of 4.22. The reader is referred to [180], for more information regarding the band structure of GaAs.

The transitions at E_2 and E_4 are represented by a single sharp peak at $\omega \approx 4.5$ eV. Again there is a red-shift as compared to experimental data. The two transitions take the shape of a shoulder followed by a peak within the experimental approach, the implementation developed in this work does not reproduce this feature. It is also noted that the real part of the dielectric response (figure 4.23) illustrates ε_1 displaying significant structure within the range of the E_2, E_4 transitions ($\sim [4-5]$ eV). Recall the case of the Harmonic Oscillator of figure 1.1a in which the asymptotic-like features at a specific frequency for the real part of the response function corresponded to the maximal values in the imaginary part of the response as shown in figure 1.1b. Likewise, the peak of the highest magnitude in ε_2 is located within the same frequency range ($\omega \approx 4.5$ eV).

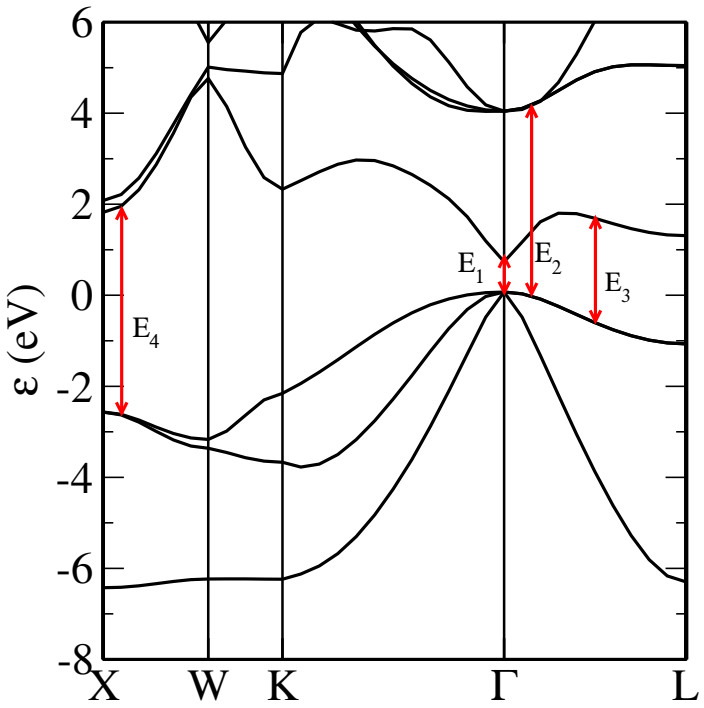

Fig. 4.22 Band structure of GaAs plotted along high symmetry points.

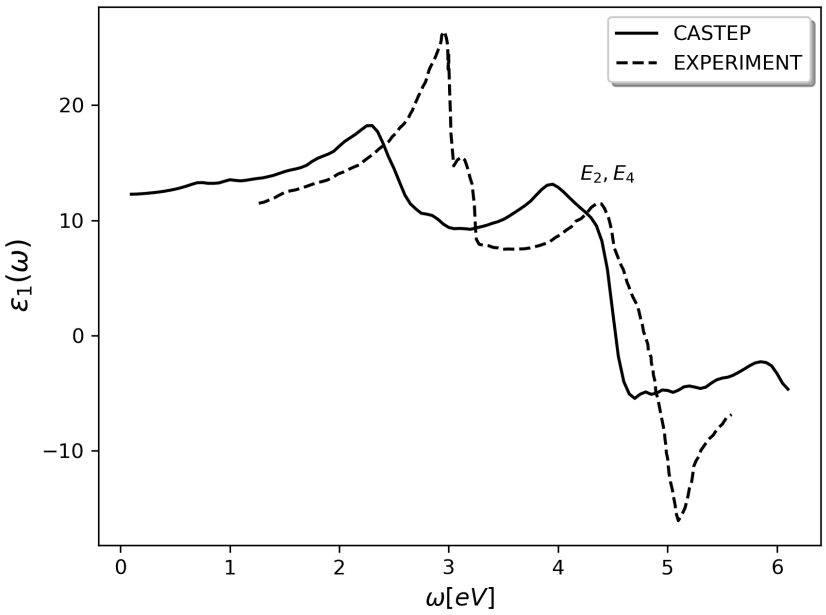

Fig. 4.23 Real component of the dielectric response for GaAs, spectroscopic ellipsometry data from Lautenschlager *et al* [179].

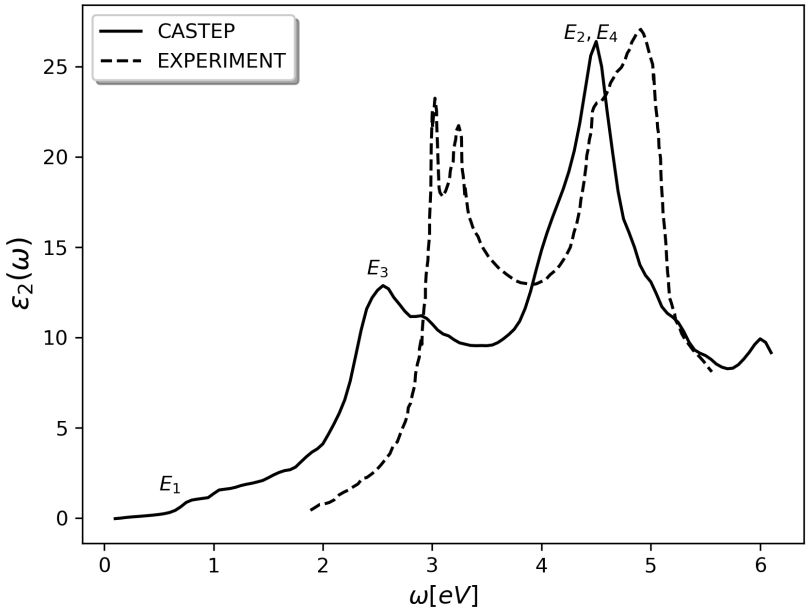

Fig. 4.24 Imaginary component of the dielectric response for GaAs, spectroscopic ellipsometry data from Lautenschlager *et al* [179].

4.7 Zinc Oxide

The electronic and optical properties of Zinc Oxide (ZnO) make it ideal for use in a range of applications such as solar cells, gas sensors and piezoelectric devices [88]. The Hexagonal wurtzite structure of ZnO is known to be the most stable structure under ambient conditions [181] and is used for this computation. The band structure is shown in figure 4.25 in which the valence band minimum and conduction band minimum are located at the Γ point, representing a direct bandgap.

Here, the real and imaginary parts of the dielectric spectra are computed for comparison at the lower frequency range. The computational DFT parameters constitute a plane-wave cutoff energy 800 eV and an MP grid of $30 \times 30 \times 24$. Figure 4.26 illustrates the spectra along with experimental ellipsometry data from Jellison *et al* [182]. The critical point is found to be at $\omega \approx 1.1$ eV which coincides with the band gap located at the Γ point. The red-shift presented here is significant and is due to the discrepancy of DFT in computing the ZnO bandgap.

The spectra of 4.27 and 4.28 represent the response computed for a broader frequency range with ellipsometry data from Rakel *et al* [183]. The noise found in the dielectric response

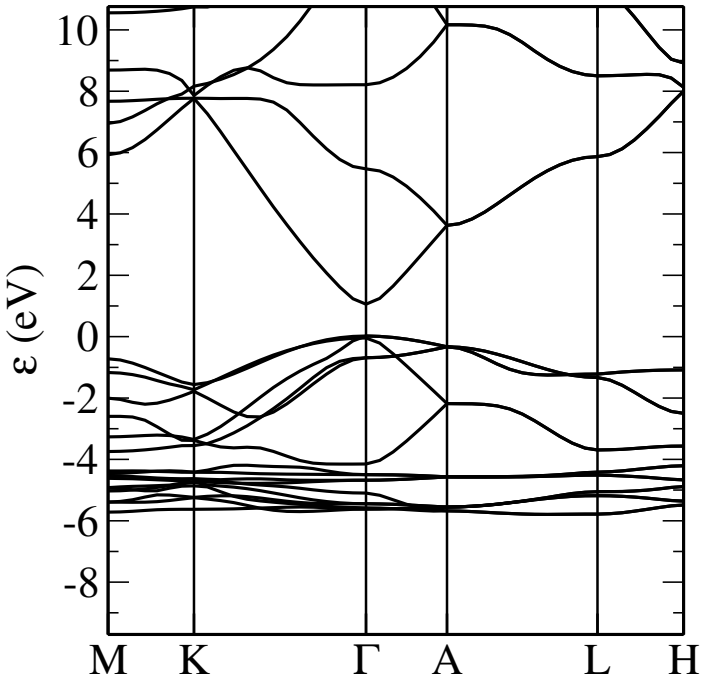

Fig. 4.25 Band structure of ZnO plotted along high symmetry points.

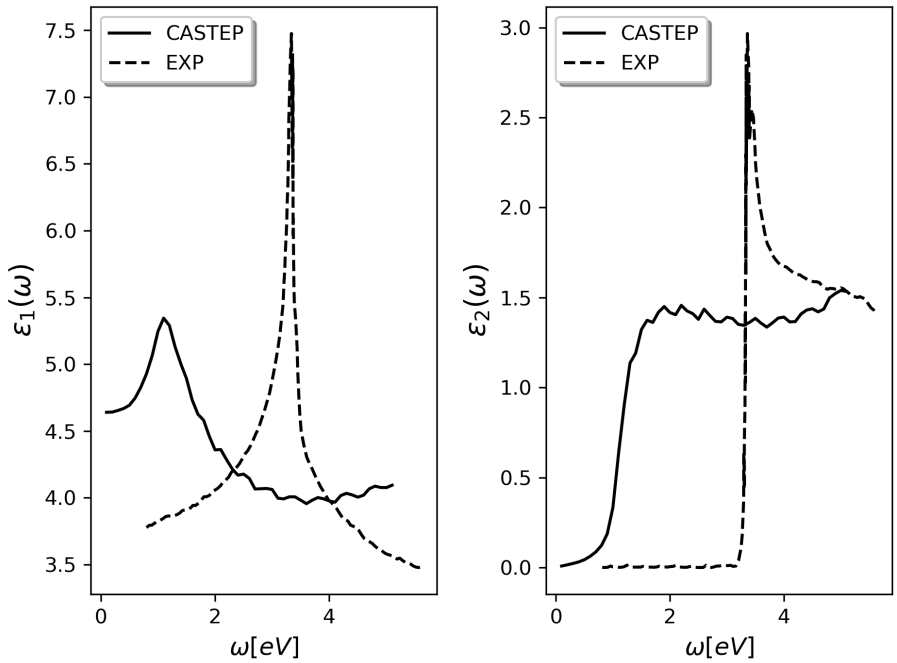

Fig. 4.26 Real and imaginary components of the dielectric response for ZnO displaying the exciton state associated with the bandgap, spectroscopic ellipsometry data from Jellison *et al* [182].

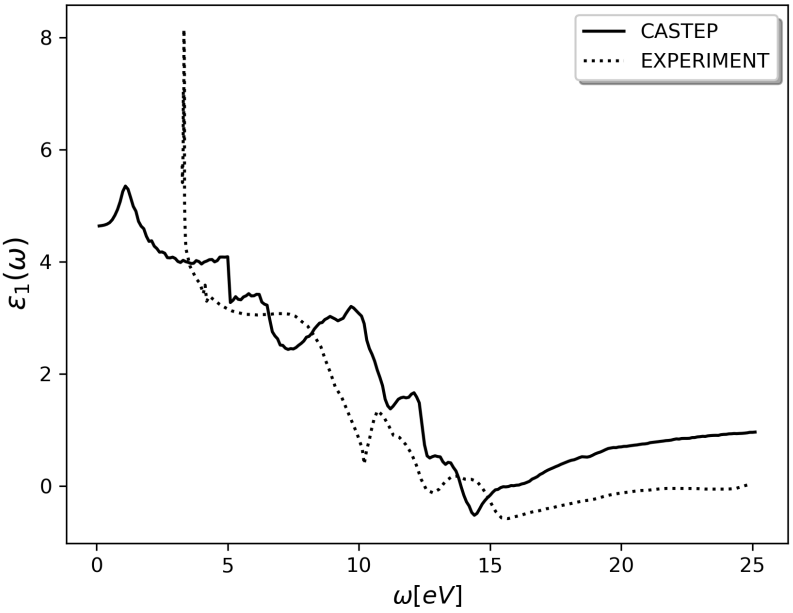

Fig. 4.27 Real component of the dielectric response of ZnO for a broader frequency range, spectroscopic ellipsometry data from Rakel *et al* [183].

can be attributed to a slightly coarse choice of reciprocal space sampling. Nevertheless, the edge associated with transitions at the bandgap (E) and the other three critical points of (A, B, C) found in ε_2 and the overall shape for both parts of the dielectric function are in good agreement with alternative computations of the dielectric matrix found in [184, 185, 186, 187, 188]. The peaks found in the imaginary response are related to transitions between the valence and conduction bands. Further information into the origin of these peaks can be found in [181, 187, 189].

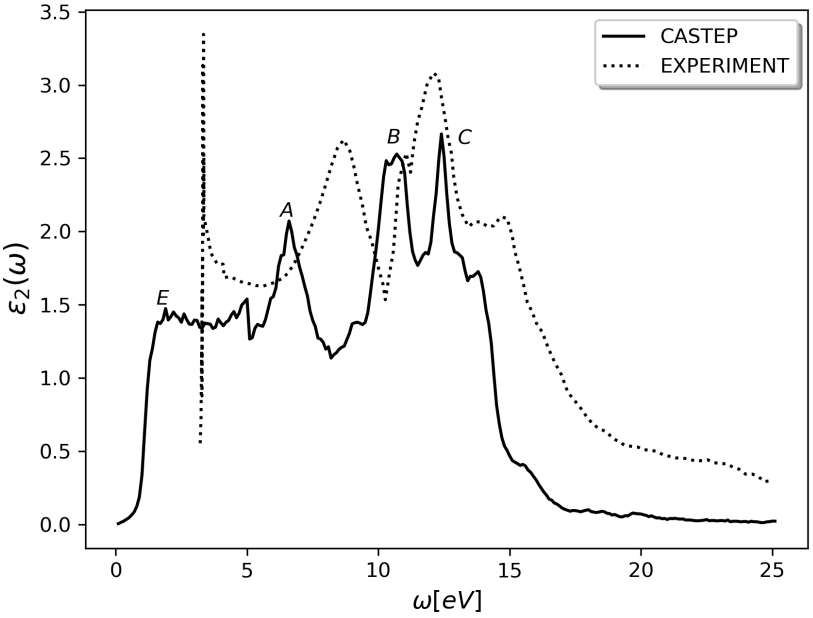

Fig. 4.28 Imaginary component of the dielectric response of ZnO for a broader frequency range, spectroscopic ellipsometry data from Rakel *et al* [183].

4.8 Methylammonium Lead Triiodide

The past decade has seen much development in solar cell technologies. Organic-inorganic hybrid perovskites such as Methylammonium Lead Triiodide (MaPbI3) have high photovoltaic efficiencies and have been employed in thin-film electronic devices, lasing applications and as solar cell absorber materials [125, 190]. The GGA-PBE band structure is shown in figure 4.29, with an approximated bandgap of 1.55 eV.

The importance of reciprocal space sampling is again demonstrated here, figure 4.30 shows the real and imaginary components of the response respectively and are plotted for two choices of MP grid. The coarser MP grid of $12 \times 12 \times 12$ shows a non-zero ε_2 at the low-frequency range of $0-0.5$ eV. This conflicts with experimental data found in [125, 190] and is corrected in the finer MP grid computation. The static dielectric constant given by $\varepsilon_1(\omega = 0)$ for the coarse MP grid is on the order of $(14\% - 16\%)$ larger than the constants computed by El-Ghtami [190] and Löper [125]. This deviation is reduced to the order of $3\% - 5\%$ when utilising the finer MP grid of $20 \times 20 \times 20$.

Figures 4.31 and 4.32 illustrate the real and imaginary components of the dielectric response with an experimental data fit from Löper *et al* [125]. A plane-wave cutoff energy of 2000

eV is used with the aforementioned necessary MP grid of 20 $\times$ 20 $\times$ 20. The overall spectral shape of the response compares somewhat well to the experimental data of Löper. The real part of the response from Löper features 3 kinks of which only the peak at 2.5 eV is reproduced by the Sternheimer implementation (albeit red-shifted). The same is also observed for ε_2, with only the highest peak being shifted by approximately 0.7 eV from the highest peak for Löper which is located at $\omega = 3.5$ eV.

The complex dielectric function is a powerful tool in the optical characterisation of materials. With both components of the dielectric function for a spectrum of ω, quantities such as the complex refractive index of a material $\tilde{n}(\omega)$ can be determined by the following:

$$\tilde{n}(\omega) = n(\omega) + ik(\omega) = (\varepsilon_1 + i\varepsilon_2)^{1/2}. \tag{4.12}$$

Where $n(\omega)$ describes the real component of the refractive index, while $k(\omega)$ is the imaginary component and is also referred to as the *extinction coefficient*. Here, rather than stopping with the computation of the dielectric response, an extra step is made to calculate the absorption coefficient which is given by the following expression:

$$\alpha(\omega) = 2\omega k(\omega) = 2\omega \left[\frac{-\varepsilon_1(\omega)}{2} + \sqrt{\frac{\varepsilon_1^2(\omega) + \varepsilon_2^2(\omega)}{2}} \right]. \tag{4.13}$$

Figure 4.33 compares the shape of the absorption coefficient directly computed from the response data to that of experimental work by Löper. The absorption coefficient is extracted from the experimental refractive index by $\alpha = 4\pi k/\lambda$, hence the units of cm^{-1}. The comparisons with respect to the dielectric spectra are echoed. The spectral feature at $\omega = 2.5$ eV is not found, however, the overall shape of the coefficient is reproduced.

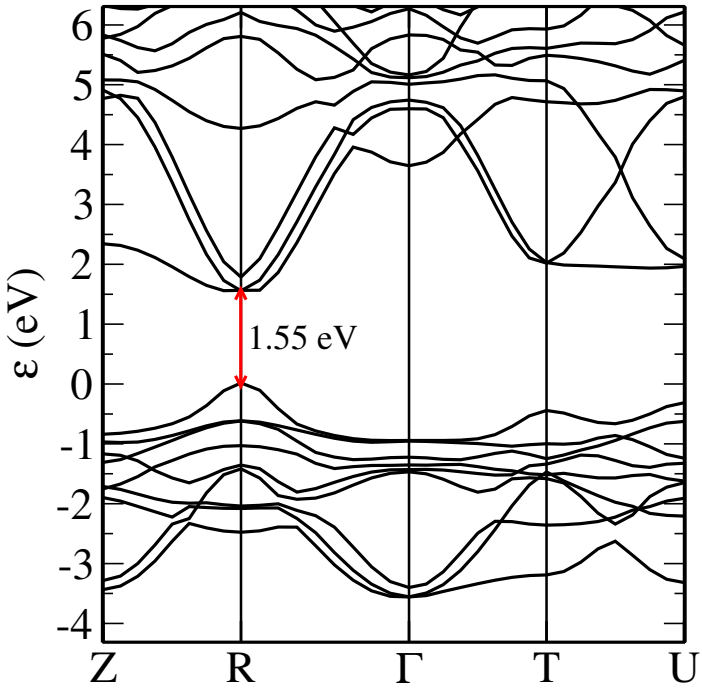

Fig. 4.29 Band structure for MaPbI3, plotted along high symmetry points of the Brillouin Zone.

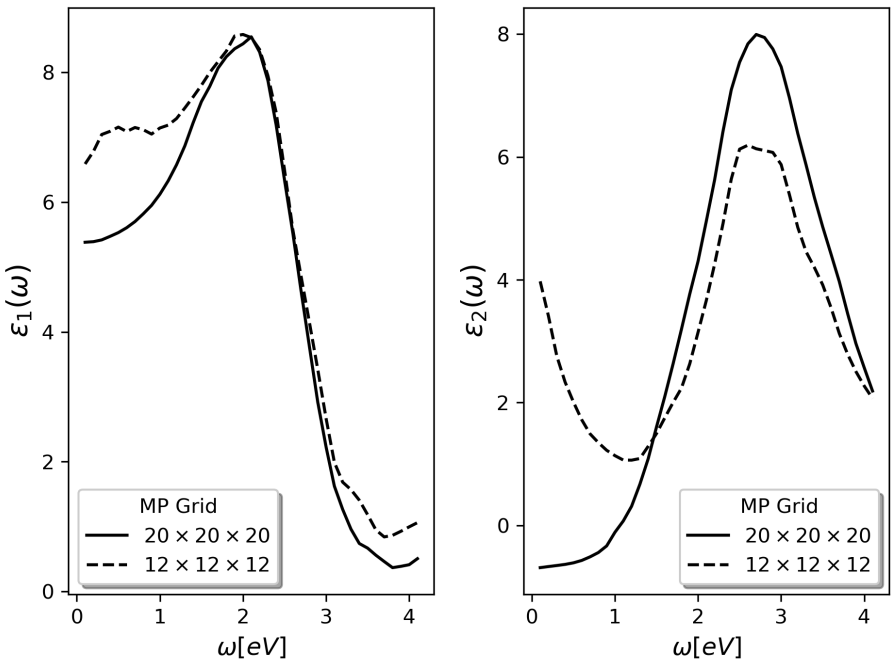

Fig. 4.30 Real and imaginary components of the dielectric response for MaPbI3 plotted for two choices of reciprocal space sampling.

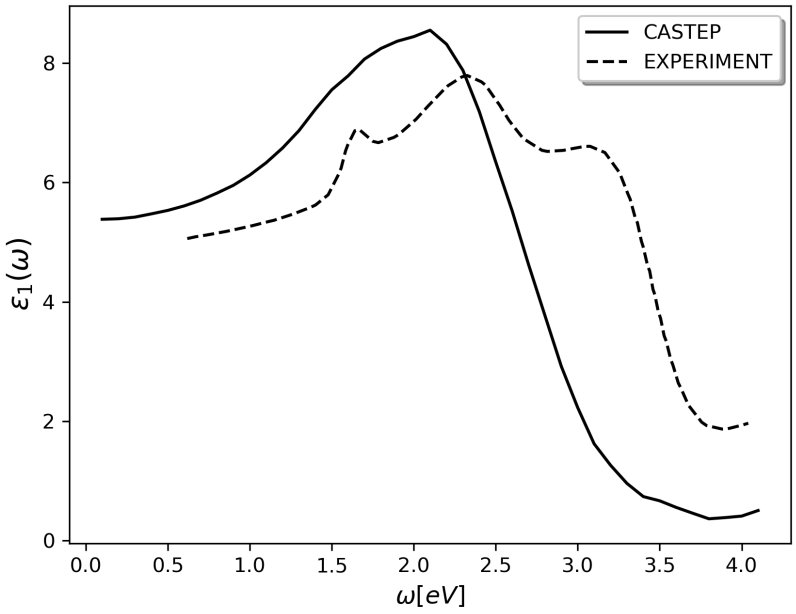

Fig. 4.31 Real component of the dielectric response for MaPbI3, spectroscopic ellipsometry data from Löper *et al* [125].

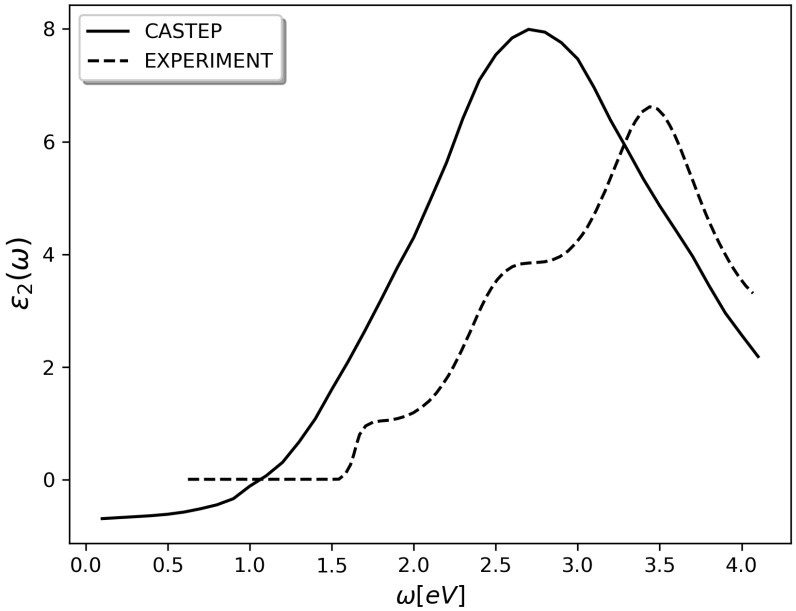

Fig. 4.32 Imaginary component of the dielectric response for MaPbI3, spectroscopic ellipsometry data from Löper *et al* [125].

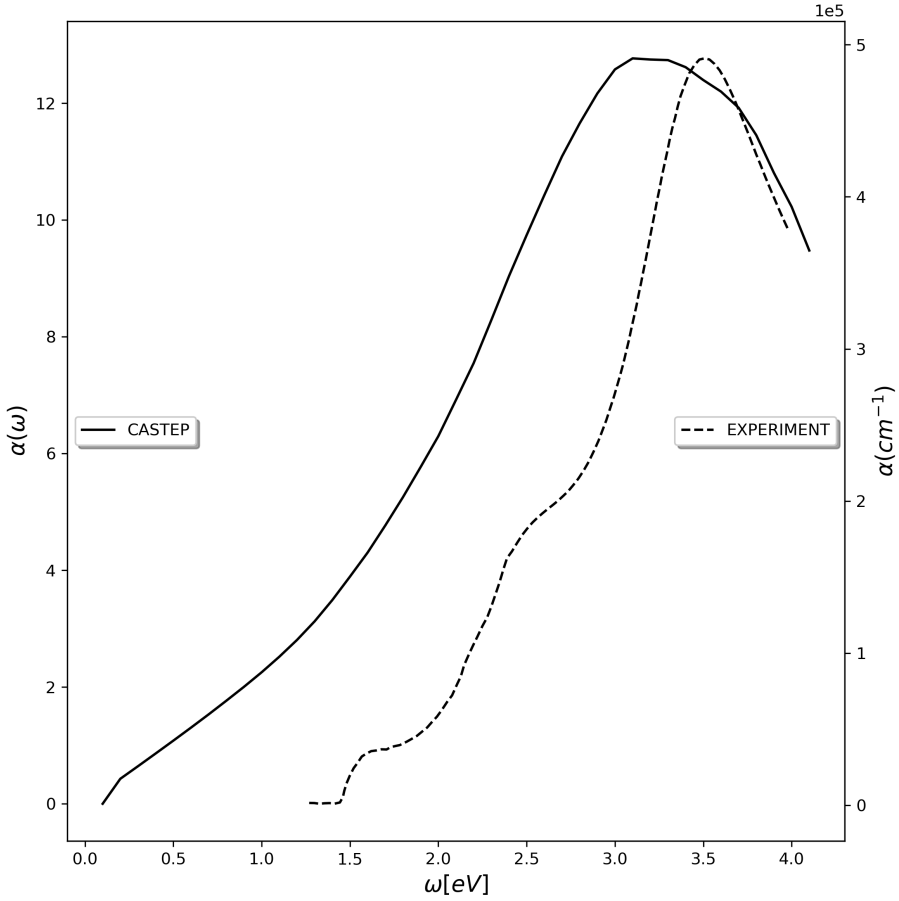

Fig. 4.33 Absorption coefficient for MaPbI3, plotted with the experimental determination of the absorption coefficient from refractive index data obtained from Löper *et al* [125].

Chapter 5

Longitudinal Spin Response

The other response quantity of this thesis is linked to magnetism and therefore spin fluctuations of the density. Spin excitations have been proposed to underpin various properties of itinerant magnetic systems. The mechanism for high-temperature superconductivity [191] and phase transitions at the Curie and Néel temperatures are attributed to such excitations [192]. The field of computing has shown a growing interest in the field of *spintronics* in which the spin degrees of freedom of the electron are exploited for use in logical operations [91].

In order to compute the spin response function, further development of DFPT is needed to encompass spin which was considered degenerate in the previous dielectric response computations.

5.1 Collinear and Noncollinear Representations

The theory outlined in the spin DFT section of 2.1.3 employed the noncollinear representation of the magnetisation and wavefunctions. The magnetisation has the freedom to orient in any/multiple vector direction(s), necessitating the use of all three Pauli matrices and the spinorial wavefunction. Here the spin indices $1,2 = \alpha,\beta$ are now used to indicate the spin up $|1\rangle$ and down $|2\rangle$ states. The general form of the two-component spinor in matrix form is

$$\Psi(\boldsymbol{r}) = \begin{pmatrix} \psi_1(\boldsymbol{r}) \\ \psi_2(\boldsymbol{r}) \end{pmatrix}. \tag{5.1}$$

The electronic density is composed of the spinorial components and the real space parameter of $\boldsymbol{r}$ is assumed:

$$n = (\psi_1^* \psi_1 + \psi_2^* \psi_2)\,. \tag{5.2}$$

The three magnetisation components are written out in full using the Pauli matrices previously shown in section 2.1.3:

$$m_x = (\psi_1^* \psi_2 + \psi_2^* \psi_1)\,, \tag{5.3}$$

$$m_y = i\,(\psi_2^* \psi_1 - \psi_1^* \psi_2)\,, \tag{5.4}$$

$$m_z = (\psi_1^* \psi_1 - \psi_2^* \psi_2)\,. \tag{5.5}$$

The density matrix can now be rewritten in terms of these components and is expressed in matrix form:

$$n = \frac{1}{2} \begin{pmatrix} n + m_z & m_x - i m_y \\ m_x + i m_y & n - m_z \end{pmatrix}. \tag{5.6}$$

Thus, there are four densities one must store in order to compute the density matrix and formulate the KS equations.

Collinear magnetism is defined by having the magnetisation at each point in space being aligned towards a single fixed quantisation axis. For mathematical convenience, the z-axis is chosen. The vector magnetisation components of m_x and m_y are null in this picture leaving only two components needed to represent the density matrix:

$$n = \frac{1}{2} \begin{pmatrix} n + m_z & 0 \\ 0 & n - m_z \end{pmatrix} = \frac{1}{2} \begin{pmatrix} n + m_z \\ n - m_z \end{pmatrix} = \begin{pmatrix} n_\uparrow \\ n_\downarrow \end{pmatrix}. \tag{5.7}$$

The off diagonal elements are ($n_{12} = n_{21} = 0$), which yields a two-component density matrix. Dropping the z subscript, the charge and magnetisation densities in the collinear scheme are given by:

$$n = n_\uparrow + n_\downarrow, \tag{5.8}$$

$$m = n_\uparrow - n_\downarrow. \tag{5.9}$$

The response function investigated here will involve developing DFPT through the framework of collinear magnetism, note as opposed to the noncollinear case, now there are only two densities to deal with. The spinor wavefunction is also now simply composed of two components that are aligned in a parallel or anti-parallel configuration along z.

5.2 Longitudinal Excitations

The spin-polarised KS equations of (2.28) give little intuition as to how magnetism comes into play. It is the exchange interaction contained within the XC functional that takes into account electron-electron interactions beyond the classical Hartree interaction. The XC magnetic field is a functional derivative of the XC energy with respect to magnetisation:

$$B_{xc}(\boldsymbol{r}) = \frac{\delta E_{xc}[n(\boldsymbol{r}), m(\boldsymbol{r})]}{\delta m(\boldsymbol{r})}. \tag{5.10}$$

Unfortunately as with the non-spin case, the exact form of the energy XC functional is not known. Barth and Hedin [26] offer a reasonable approximation for E_{xc}. The external potential is taken to be slowly varying and the electronic system is divided into small boxes. Each box contains the well-known spin-polarised homogeneous electron gas with spin-up and spin-down densities $(n_\uparrow, n_\downarrow)$. If the XC energy per particle of the gas is ε_{xc}, then for an electronic system in which the spin density varies slowly:

$$E_{xc}\{n_{\uparrow,\downarrow}(\boldsymbol{r})\} = \int \{n_\uparrow(\boldsymbol{r}) + n_\downarrow(\boldsymbol{r})\} \varepsilon_{xc}\left(n_\uparrow(\boldsymbol{r}), n_\downarrow(\boldsymbol{r})\right) d\boldsymbol{r}. \tag{5.11}$$

This is known as the *Local Spin Density Approximation* (LSDA) and although the condition of a slowly varying spin density may not seem an appropriate measure for real systems, LSDA has been utilised effectively to describe magnetic systems [193].

Figures 5.1 and 5.2 present sketches featuring two classes of spin excitations. *Transverse* excitations involve fluctuations of the magnetisation vector in both x and y, perpendicular to the z axis. The quasiparticle associated with transverse collective modes is known as

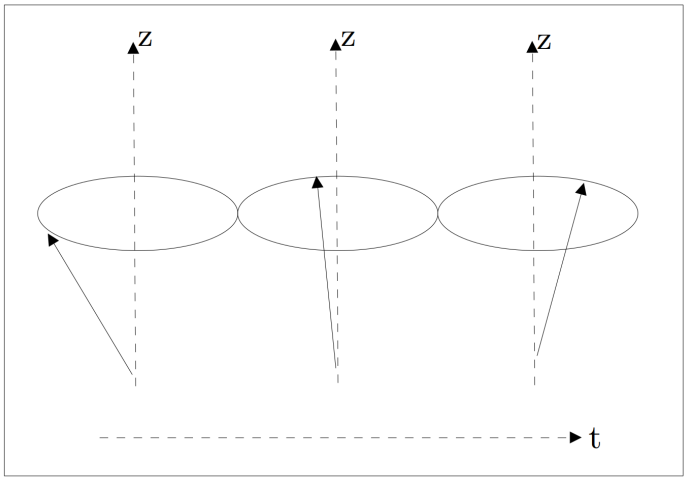

Fig. 5.1 Sketch of transverse excitations which are known as magnons. The spin waves rotate about z and thus involve x and y components of the magnetisation.

a *magnon*. The most common picture is that of precession around the z axis. An *ab initio* approach to modelling magnons requires knowledge of the dynamic transverse spin susceptibility, in which the poles of the response correspond to magnon excitations. The reader is referred to work by Cao *et al* [194] where the Sternheimer formalism is utilised to compute the transverse susceptibility. Such first-principle computations of magnon excitation spectra have been developed using a diverse range of techniques [65, 66, 195, 196]. However, transverse excitations are not the focus of this work.

The other illustration of figure 5.2 involves fluctuations of the spin density along $\pm z$. At $T = 0$ the change in magnetisation along z is known to correspond to a longitudinal spin excitation. Such fluctuations involve particle-hole pairs of the *same spin* as shown by the sketch of 5.2 which shows fluctuations in z of the same spin along either t or t'. From the collinear picture presented earlier, it is expressed in equation (5.5) that the magnetisation is equal to the difference between spin up and down densities. Therefore, the variation of the magnetisation requires knowledge of the spin up and down response (perturbed) densities. The following sections will extend the collinear formalism to DFPT with a discussion of the spin-polarised Sternheimer scheme.

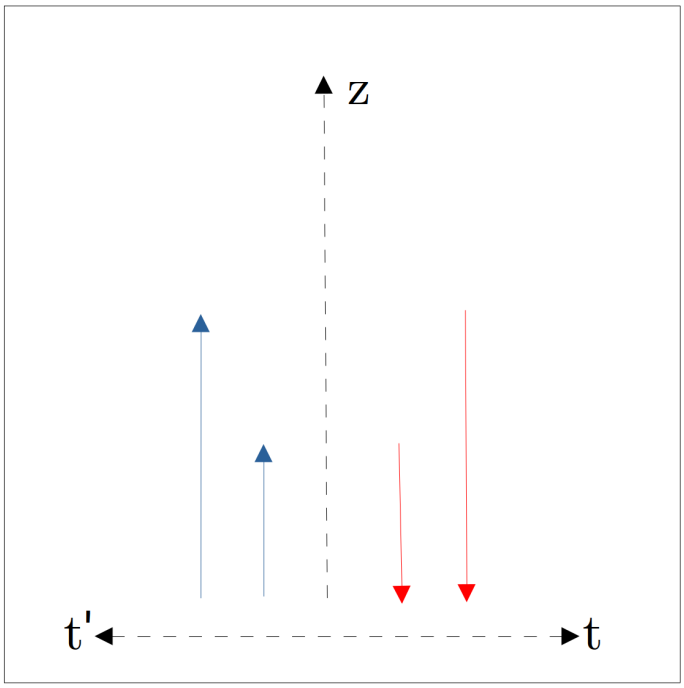

Fig. 5.2 Sketch of longitudinal excitations which involve fluctuations of the spin density along z. These excitations involve particle-hole pairs of the same spin.

5.3 Spin-Polarised DFPT

This section will employ the collinear representation to present the Sternheimer equation with spin dependencies. The response function of interest is the spin susceptibility which connects the induced spin density response to an external spin-polarised perturbation:

$$\delta m(\boldsymbol{r},t) = \int\int d\boldsymbol{r}'dt'\chi(\boldsymbol{r},t,\boldsymbol{r}',t')\delta B_{ext}(\boldsymbol{r}',t'). \tag{5.12}$$

In the frequency domain:

$$\delta m(\boldsymbol{r},\omega) = \int d\boldsymbol{r}'\chi(\boldsymbol{r},\boldsymbol{r}',\omega)\delta B_{ext}(\boldsymbol{r}',\omega), \tag{5.13}$$

having defined:

$$\delta m(\boldsymbol{r},\omega) = \int dt\delta m(\boldsymbol{r},t)e^{-i\omega t}. \tag{5.14}$$

The Sternheimer equations in Bloch form:

$$\left(\hat{H}_{\boldsymbol{k}+\boldsymbol{q}} - \varepsilon_{ns\boldsymbol{k}} + \omega + i\eta\right) \delta u_{ns\boldsymbol{k}+\boldsymbol{q}}(\boldsymbol{r}, +\omega) = -(1 - \hat{P}_{occ}^{\boldsymbol{k}+\boldsymbol{q}}) \delta V_{scf}^{+\boldsymbol{q}}(\boldsymbol{r}, +\omega) u_{ns\boldsymbol{k}}(\boldsymbol{r}), \quad (5.15)$$

$$\left(\hat{H}_{\boldsymbol{k}-\boldsymbol{q}} - \varepsilon_{ns\boldsymbol{k}} - \omega + i\eta\right) \delta u_{ns\boldsymbol{k}-\boldsymbol{q}}(\boldsymbol{r}, -\omega) = -(1 - \hat{P}_{occ}^{\boldsymbol{k}-\boldsymbol{q}}) \delta V_{scf}^{-\boldsymbol{q}}(\boldsymbol{r}, -\omega) u_{ns\boldsymbol{k}}(\boldsymbol{r}), \quad (5.16)$$

where the subscript s is introduced which runs over $|\uparrow\rangle$, $|\downarrow\rangle$, the spin up and down states:

$$u_{ns\boldsymbol{k}}(\boldsymbol{r}) = \begin{pmatrix} u_{n\boldsymbol{k}}^{\uparrow}(\boldsymbol{r}) \\ u_{n\boldsymbol{k}}^{\downarrow}(\boldsymbol{r}) \end{pmatrix}. \quad (5.17)$$

Note how instead of simply $\pm\omega$ as in the dielectric case of equation (4.3), a separate Sternheimer equation is explicitly shown for $(-\boldsymbol{q}, -\omega)$. This is a consequence of the external magnetic field ($B_{ext} = V_{ext}$) breaking *time-reversal symmetry*. This means that the useful symmetry of the wavefunction $u_{\boldsymbol{q}} = u_{-\boldsymbol{q}}$ cannot be employed. Whilst time-reversal symmetry still holds for the case of long-wavelength ($\boldsymbol{q} \to 0$), here the response to a finite $\boldsymbol{q}$ vector is of interest. As a result, separate computations must be done for both the $(+\boldsymbol{q}, +\omega)$ and $(-\boldsymbol{q}, -\omega)$ channels. This has implications for how the scheme is handled in CASTEP which will be discussed in the following sections.

The variation of the density matrices involves the solution of the first-order response wavefunctions of (5.15) and (5.16):

$$\delta n_{\boldsymbol{q}}(\boldsymbol{r}, \omega) = \frac{1}{N_{\boldsymbol{k}}} \sum_{n \in occ, \boldsymbol{k}} u_{ns\boldsymbol{k}}^{\dagger}(\boldsymbol{r})\, \boldsymbol{I}_2\, \delta u_{ns\boldsymbol{k}+\boldsymbol{q}}(\boldsymbol{r}, \omega) + \frac{1}{N_{\boldsymbol{k}}} \sum_{n \in occ, \boldsymbol{k}} \delta u_{ns\boldsymbol{k}-\boldsymbol{q}}^{\dagger}(\boldsymbol{r}, -\omega)\, \boldsymbol{I}_2\, u_{ns\boldsymbol{k}}(\boldsymbol{r}), \quad (5.18)$$

where $\boldsymbol{I}_2$ is the 2×2 identity matrix. The induced spin magnetisation along z is defined with the Pauli matrix σ_z:

$$\delta m_{\boldsymbol{q}}(\boldsymbol{r},\omega) = \frac{1}{N_{\boldsymbol{k}}} \sum_{n\in occ,\boldsymbol{k}} u^{\dagger}_{ns\boldsymbol{k}}(\boldsymbol{r})\ \sigma_z\ \delta u_{ns\boldsymbol{k}+\boldsymbol{q}}(\boldsymbol{r},\omega) + \frac{1}{N_{\boldsymbol{k}}} \sum_{n\in occ,\boldsymbol{k}} \delta u^{\dagger}_{ns\boldsymbol{k}-\boldsymbol{q}}(\boldsymbol{r},-\omega)\ \sigma_z\ u_{ns\boldsymbol{k}}(\boldsymbol{r}). \quad (5.19)$$

The variation of the KS potential is defined through the unperturbed (ground-state) and induced densities:

$$\begin{aligned}\delta V^{\boldsymbol{q}}_{KS}(\boldsymbol{r},\omega) &= \sigma_z \delta B_{ext}(\boldsymbol{q},\omega) \\ &+ \int \frac{\delta n(\boldsymbol{r}',\omega)}{|\boldsymbol{r}-\boldsymbol{r}'|} e^{-i\boldsymbol{q}\cdot(\boldsymbol{r}-\boldsymbol{r}')} d\boldsymbol{r}' \\ &+ f_{xc}[n_\uparrow(\boldsymbol{r}), n_\downarrow(\boldsymbol{r}), \boldsymbol{r}]\delta n_{\uparrow,\boldsymbol{q}}(\boldsymbol{r},\omega) + f_{xc}[n_\uparrow(\boldsymbol{r}), n_\downarrow(\boldsymbol{r}), \boldsymbol{r}]\delta n_{\downarrow,\boldsymbol{q}}(\boldsymbol{r},\omega).\end{aligned} \quad (5.20)$$

The first line of (5.20) corresponds to a small, spin-polarised external perturbation. The second line of (5.20) is the Hartree term which is spin independent. The third line of (5.20) contains the exchange-correlation kernel which is evaluated for the unperturbed spin up and down densities. These can be written in terms of the charge and magnetisation densities by (5.7). The *adiabatic* local spin density approximation is used in which the kernel is evaluated at an instantaneous density:

$$f_{xc}(\boldsymbol{r}t,\boldsymbol{r}'t') = \frac{\delta^2 E_{xc}}{\delta m(\boldsymbol{r})\delta m(\boldsymbol{r}')}\delta(\boldsymbol{r}-\boldsymbol{r}')\delta(t-t'). \quad (5.21)$$

LibXC is a library of exchange-correlation functionals and has been interfaced with other DFT software packages [197]. The spin-polarised LDA functional has been interfaced with CASTEP and is used to compute the exchange-correlation kernel for the two independent spin indices. The Slater exchange, along with Perdew and Zunger's correlation functionals are used [98, 198].

From equation (5.16) it is shown that $\delta V^{-\boldsymbol{q}}_{KS}$ is required. This is done by changing the signs of $\boldsymbol{q}$ and ω in equation (5.20) and using $\delta n_{-\boldsymbol{q}} = \delta n^*_{\boldsymbol{q}}$ and $\delta m_{-\boldsymbol{q}} = \delta m^*_{\boldsymbol{q}}$.

The susceptibility can be calculated from the self-consistent solution of the induced magnetisation:

$$\chi_z(\boldsymbol{q},\omega) = \int d\boldsymbol{r}\ \delta m^{\boldsymbol{q}}_{scf}(\boldsymbol{r},\omega). \tag{5.22}$$

Which is the unit-cell average of the magnetisation in response to a small magnetic field perturbation. Making use of reciprocal space and noting that excitations of the imaginary part of the response function have physical meaning:

$$\chi''_z(\boldsymbol{q},\omega) = Im[\delta m^{\boldsymbol{q}}_{scf}(\boldsymbol{G}=0,\omega)]. \tag{5.23}$$

This scheme is equivalent to obtaining the time-dependent DFPT generalised susceptibility obtained via a Dyson equation. The reader is referred to [194, 199, 200] for further information. The quantities involved in this approach are of the form shown in Adler-Wise's formulation of the non-interacting density response function in equation (3.20). In the collinear case, the charge and spin non-interacting Kohn-Sham susceptibility are defined in terms of the unperturbed KS orbitals, the parameterisation in real space is assumed:

$$\chi^{00}_{KS}(\omega) = \sum_{ij}(f_i - f_j)\frac{[\psi_i^\dagger \boldsymbol{I}_2 \psi_j][\psi_j^\dagger \boldsymbol{I}_2 \psi_i]}{\omega - (\varepsilon_j - \varepsilon_i) + i\eta}, \tag{5.24}$$

$$\chi^{zz}_{KS}(\omega) = \sum_{ij}(f_i - f_j)\frac{[\psi_i^\dagger \sigma_z \psi_j][\psi_j^\dagger \sigma_z \psi_i]}{\omega - (\varepsilon_j - \varepsilon_i) + i\eta}, \tag{5.25}$$

where the indices i, j run over band (n), wavevector ($\boldsymbol{k}$, $\boldsymbol{k}+\boldsymbol{q}$) and spin. Attention must be paid to the occupation functions of f_i and f_j. The form of these will be discussed in a later section concerning fractional occupations which are characteristic of metallic systems. The time-dependent DFT self-consistent Dyson equation can be written as

$$\chi^{\alpha\alpha}(\omega) = \chi^{\alpha\alpha}_{KS}(\omega) + \chi^{\alpha\alpha}_{KS}(\omega) f_{Hxc}(\omega)\chi^{\alpha\alpha}(\omega). \tag{5.26}$$

In the collinear case: $\alpha = 0, z$. The solution to (5.26), yields the interacting charge-spin susceptibility of the system:

$$\delta n(\omega) = \int_{\mathbb{R}} \chi^{00}(\omega)\delta v_{ext}(\omega), \tag{5.27}$$

$$\delta m(\omega) = \int_{\mathbb{R}} \chi^{zz}(\omega)\delta v_{ext}(\omega). \tag{5.28}$$

5.4 Implementation of Spin Polarised DFPT in CASTEP

This section will describe the DFPT implementation for calculating the longitudinal spin susceptibility in CASTEP. Equations (5.15), (5.16), (5.18), (5.19) and (5.20) are solved self-consistently. It is reminded here that the approach is fully *ab initio* in that no material-specific parameters are considered.

The flowchart of 5.3 represents the process of computing the spin response. It begins with a self-consistent ground-state in which knowledge of the ground-state charge density, magnetisation, KS eigenvalues and plane-wave coefficients at $\boldsymbol{k}$ are determined.

For the $(+\boldsymbol{q},+\omega)$ and $(-\boldsymbol{q},-\omega)$ channels, the ground-state wavefunction at both $\{\boldsymbol{k}+\boldsymbol{q}\}$ and $\{\boldsymbol{k}-\boldsymbol{q}\}$ must be determined. A computational saving can be made here in the choice of $\boldsymbol{q}$. If such a $\boldsymbol{q}$ is chosen such that it is commensurate with the k-points present in the MP grid then the plane-wave coefficients are known already. This however places a restriction on the choice of $\boldsymbol{q}$ and so the decision was made to compute the ground-state wavefunctions for any choice of $\boldsymbol{q}$.

For the first iteration, the SCF potentials of $\delta V_{KS}^{+\boldsymbol{q}}$ and $\delta V_{KS}^{-\boldsymbol{q}}$ are set to the the first line of equation (5.20). This is a small, scalar, spin-polarised external potential $\frac{1}{2}\sigma_z$. The Sternheimer equation is then solved for both channels along the frequency axis offset by a small imaginary component (η). In order to treat partial occupancies, a sum-over-states (SOS) contribution is also used, this will be discussed in a later section.

The robust and thoroughly tested BiCGStab algorithm from the dielectric response computations is now employed to compute the response wavefunctions for the $(+\boldsymbol{q},+\omega)$ and $(-\boldsymbol{q},-\omega)$ channels. The induced charge and spin densities can then be computed from equations (5.18) and (5.19) respectively. The densities undergo a density mixing process designed to improve the convergence properties of the self-consistent scheme, this will be discussed shortly.

The mixed densities are then used to compute the new KS potentials using equation (5.20), the conjugate of the densities are needed in order to obtain $\delta V_{KS}^{-\boldsymbol{q}}$. A check is now done to see if the energy associated with the KS potential (and therefore densities) is similar to that of previous iterations. This will become known as the *second-order energy* (5.36) and will be discussed in due course. If the energy is sufficiently similar, the susceptibility can then be computed by the now self-consistent solution of the induced spin density. Otherwise, the KS potentials are used in another loop of the SCF Sternheimer process and this is repeated until

the energy condition is reached. The self-consistent solutions of the induced spin density are to be computed for a range of ω.

In the non-self-consistent Sternheimer method used to compute the dielectric response, it was discussed that the screened interaction requires the computation for all $\boldsymbol{G'}$ components of a perturbing potential after which inversion of the matrix is needed to obtain screening. In this scheme, the self-consistency involved in the update of the KS potentials incorporates local field effects and no inversion is required. It is the induced interacting response that is found by applying an external field and computing self-consistently. Frequency peaks in the self-consistent $\chi_z''(\boldsymbol{q},\omega)$ may be indications of a collective system response to an external perturbation.

The implementation of such an approach requires the disk storage of the ground-state wavefunctions for both $(+\boldsymbol{q},+\omega)$ and $(-\boldsymbol{q},-\omega)$ channels. The channels are solved one at a time. After computation of the ground-state wavefunction, occupancies and eigenvalues for $\{\boldsymbol{k},\boldsymbol{k}+\boldsymbol{q}\}$. The Sternheimer response and sum-over-states schemes are used to obtain the first-order response orbital at $\{+\omega\}$. At this point, the first line of equations (5.18) and (5.19) can be computed. The distributed data of $\{\boldsymbol{k},\boldsymbol{k}+\boldsymbol{q}\}$ is saved to disk. The $(-\boldsymbol{q},-\omega)$ channel is then computed in which the ground-state data for $\{\boldsymbol{k},\boldsymbol{k}-\boldsymbol{q}\}$ is determined. The Sternheimer and sum-over-states response at $\{-\omega\}$ allows for the computation of the second line in equations (5.18) and (5.19). Every subsequent self-consistent iteration requires to switch between channels which is why the distributed data is stored appropriately for the first iteration. Note the contrast to the dielectric case in which only the data at $\{\boldsymbol{k},\boldsymbol{k}+\boldsymbol{q}\}$ is required and a simple sign change of $\{\omega\}$ is used to compute the response.

5.4.1 Fractional Occupations

The implementation developed here is to be applied to systems that exhibit non-zero magnetisation in the ground-state. The transition metal systems of bcc-Iron and fcc-Nickel serve as suitable systems for testing. These are metals and as such do not exhibit the finite energy gap shown in the semiconductor systems computed previously for the dielectric response. Instead, partially occupied bands cross the Fermi level. This presents an issue with the usage of the Sternheimer equation in the definition of the projection operator onto occupied states. A costly dense sampling of reciprocal space would be needed to accurately describe the Fermi surface. However, *smearing* techniques can be used to compute an accurate density of states with relatively coarser samplings. The integer occupation number is instead replaced by a function that approximates the Dirac δ function present when approaching the Fermi level.

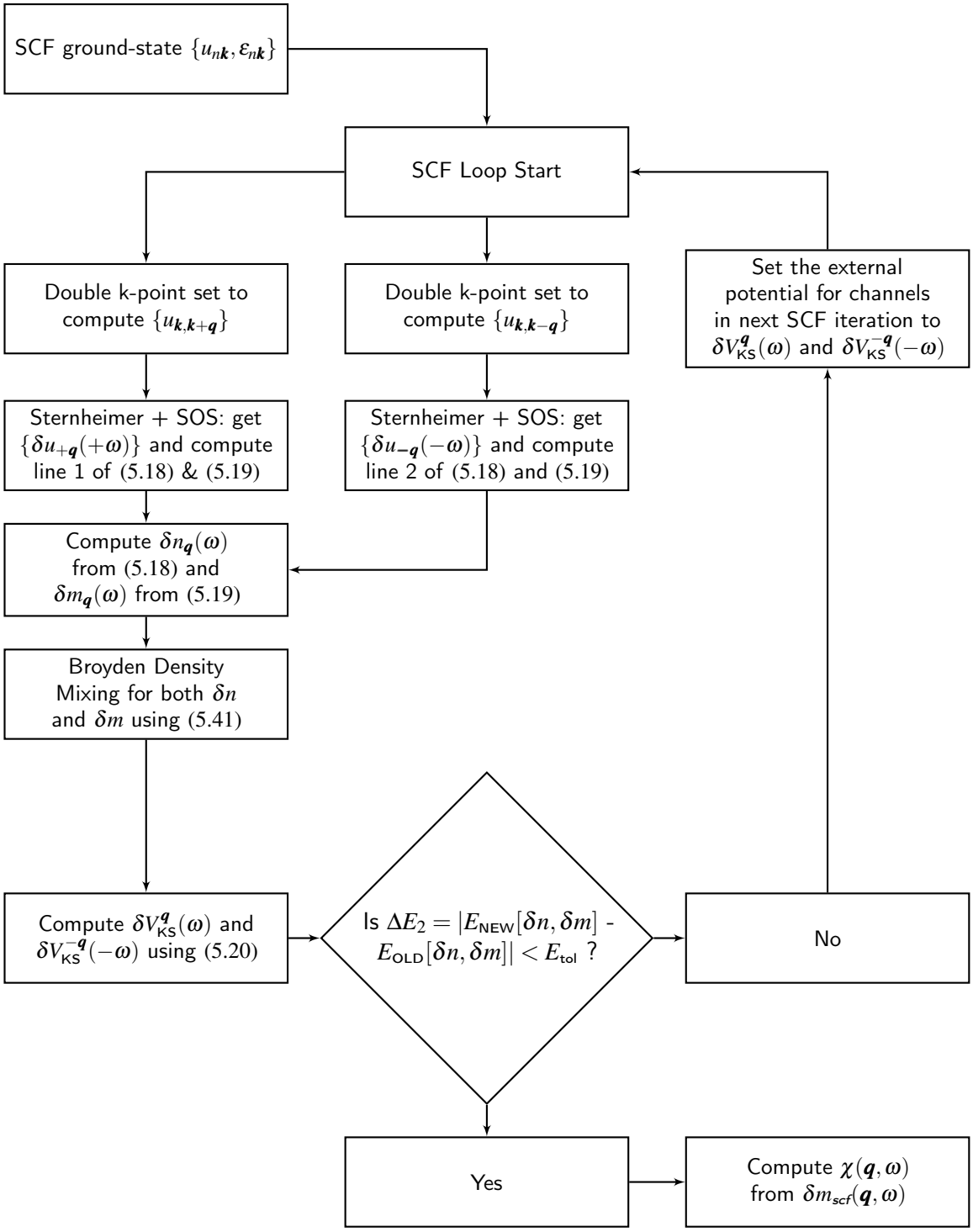

Fig. 5.3 Flow-chart of the implementation developed in CASTEP used to determine the longitudinal spin response.

The choice of function utilised for this implementation is a Gaussian [201]. Each KS energy level is broadened by a Gaussian function with a specified smearing width (broadening):

$$f(\varepsilon) = \frac{1}{2}\left[1 - \mathrm{erf}\left(\frac{\varepsilon - \mu}{\sigma}\right)\right], \tag{5.29}$$

where σ is the broadening, μ is the chemical potential and $\mathrm{erf}(x)$ is the standard error function.

Work by Gironcoli has extended the Sternheimer scheme to metallic systems [202]. In short, the formalism involves a modification of the projection operator where now occupied states, a number of partially filled bands and unoccupied states are used to compute response wavefunction.

Instead of modifying the projection operators, the computation of the response wavefunction utilises the Sternheimer scheme in conjunction with sum-over-states perturbation theory. This has already been implemented in CASTEP for the DFPT response in treating phonons and has been adapted for this work [164]. Recall section 3.3 which showed the equivalence between the two methods. The plane-wave expansion coefficients computed in sum-over-states are expressed in the following:

$$c_{nm\boldsymbol{kq}}(\omega) = \sum_{nm\boldsymbol{kq}} \frac{f_{n\boldsymbol{k}} - f_{m\boldsymbol{k}+\boldsymbol{q}}}{\varepsilon_{n\boldsymbol{k}} - \varepsilon_{m\boldsymbol{k}+\boldsymbol{q}} + \omega}, \tag{5.30}$$

where the integer occupation numbers of f_n and f_m are smeared by the Gaussian of (5.29) . These expansion coefficients contribute to the first-order response wavefunction as [110]:

$$\delta u_{n\boldsymbol{q}}(\omega) = \sum_{nm} c_{nm\boldsymbol{kq}}(\omega) \left\langle u_m \right| \delta V^{\boldsymbol{q}}_{scf} \left| u_n \right\rangle . \tag{5.31}$$

When performing computations on metallic systems, one has to make sure that an electronic state exists in which there is zero occupation on that electronic band indexed by k-point and spin. The CASTEP package displays a warning to the user if such a condition is not met. This is alleviated by the inclusion of extra bands or by reducing the smearing width.

The first-order response wavefunction used to compute the induced magnetisation and charge densities is

$$\delta u_{\boldsymbol{q}}(\omega) = \delta u_{sos,\boldsymbol{q}}(\omega) + \delta u_{stern,\boldsymbol{q}}(\omega). \tag{5.32}$$

Where δu_{sos} is the response wavefunction from equation (5.31) computed using sum-over-states perturbation theory. This includes fully occupied, partially occupied and empty states. The response wavefunction δu_{stern} refers to the numerical solution of the Sternheimer equation in (5.15), the projection operator in this case runs over fully and partially occupied states. The wavefunctions are computed independently for each $(+\boldsymbol{q}, +\omega)$ and $(-\boldsymbol{q}, -\omega)$ channels. This yields the first and second lines of the induced charge (5.18) and magnetisation (5.19) densities respectively. The implementation for Sternheimer plus sum-over-states in determining the response wavefunction has been adapted from a similar algorithm employing DFPT for phonons [164].

5.4.2 Density Mixing (DM)

In the construction of the Kohn-Sham Hamiltonian, an input density (n_{in}) is required to compute the Hartree and XC potentials. The Kohn-Sham potential is characterised as a non-linear effective potential. The output density (n_{out}) is calculated non-linearly from the eigenfunctions of the Kohn-Sham Hamiltonian [203]:

$$H_{KS}[n_{in}]\psi_i(x) = \varepsilon_i \psi_i(x), \tag{5.33}$$

$$n_{out}(x) = \sum_{i=1}^{N} |\psi_i(x)|^2. \tag{5.34}$$

Recall the flowchart of 2.2 in which self-consistency for the ground-state is reached after an iterative procedure which begins from a trial density. The energy associated with the two densities is compared and a density is said to be self-consistent if

$$n_{scf} = n_{in} = n_{out}. \tag{5.35}$$

The determination of the spin susceptibility requires a self-consistent response charge and spin density. The quantity used to check for convergence is the energy associated with the first-order KS densities and potentials. This quantity is computed as

$$E_2[\delta n, \delta m] = \int \delta n_{\uparrow}(\boldsymbol{r}) \delta V_{\uparrow}^{KS}(\boldsymbol{r}) + \delta n_{\downarrow}(\boldsymbol{r}) \delta V_{\downarrow}^{KS}(\boldsymbol{r}) d\boldsymbol{r}. \tag{5.36}$$

This is the integral of the KS potential as computed in (5.20) multiplied by the density over space. The quantity E_2 shown in equation (5.36) is also known as the second-order energy and is formulated by the first-order response quantities. The absolute value of E_2 is not of primary interest, what is desired is for the change in energy (ΔE_2) to become sufficiently small (specified by a user parameter) over the self-consistent cycles (see figure 5.3):

$$\Delta E_2 = E_2[\delta n_{(k+1)}, \delta m_{(k+1)}] - E_2[\delta n_{(k)}, \delta m_{(k)}]. \tag{5.37}$$

The direct iterative method of taking the density at iteration (k) and using this to construct the KS potentials for the $(k+1)$ iteration often does not lead to the minimisation of ΔE_2. It has been found that one needs to *mix* densities from previous iterations in an attempt to achieve a smooth and stable minimisation of ΔE_2.

Similar to many state-of-the art electronic structure codes, CASTEP hosts an array of DM schemes. The quasi-Newton method developed by Broyden [204] is utilised for the computation of the spin susceptibility. Testing was also carried out using the well-known Pulay mixing scheme [205] and for the cases of bcc-Fe and fcc-Ni, has shown similar convergence behaviour.

The $(k+1)$-th step of a self-consistent iteration can be expressed as a functional of the input density at step k:

$$n_{(k+1)} = F[n_{(k)}]. \tag{5.38}$$

The aim in mixing the density is to minimise the residual R:

$$R[n] = F[n] - n. \tag{5.39}$$

As the Broyden scheme is a quasi-Newton method, there is a requirement to construct and store the Jacobian matrix for every iteration. Work by Srivastava [206], Vanderbilt, Louie [207] and Eyert [208] developed the method to utilise an approximate Jacobian as well as optimising the order of operations required for a computationally efficient update. The exact Jacobian is defined as

$$J[n_{(k)}] = \frac{\partial R[n_{(k)}]}{\partial n_{(k)}}. \tag{5.40}$$

The Broyden method aims to update both the charge and spin density:

$$n_{out} = n_{in} - J^{-1}R[n_{in}]. \tag{5.41}$$

Johnson in 1988 combined the efforts of the previous authors and produced the modified Broyden method [209]. This uses a history of iterates to construct the inverse Jacobian and is memory efficient.

It is mentioned here that the DM scheme is by no account variational in nature. This means that there is no guarantee that a subsequent self-consistent cycle yields a minimisation of ΔE_2. This being said there are various parameters available for the user to control the DM used in electronic minimisation. The first is the cutoff energy utilised in the mixing process, this parameter takes into account any Fourier coefficients at reciprocal lattice vectors lower than the cutoff. In general, the plane-wave cutoff used for mixing is much higher than that of the standard cutoff for the basis, the reasoning is similar to that of the fine grid scale as discussed in section 4.4.2. There are also parameters which are used to specify to what extent $\delta n_{(k)}$ and $\delta m_{(k)}$ are used as input for the densities in the next iteration at $\delta n_{(k+1)}$ and $\delta m_{(k+1)}$. These are termed *mixing amplitudes* and individual control of both the charge and spin density is available in CASTEP. The user is also allowed to specify the maximum number of densities to store in history which can be used in the Broyden scheme.

The reader is referred to work by Woods *et al* [155, 203] for a more complete discussion regarding DM and preconditioning in the Kohn-Sham scheme as well as CASTEP. The *Kerker* preconditioning scheme is utilised in the self-consistent process [210]. The form of the Kerker preconditioner originates from the non-interacting density response function previously discussed in (3.20) and Thomas-Fermi theory. Charge sloshing is a potential issue faced in self-consistent calculations, in which a small variation in the input density causes a large change in the output density. This is often observed in self-consistent calculations for metallic systems and results in poor convergence. The Kerker matrix updates small $\boldsymbol{G}$ components of the density which are usually responsible for charge sloshing during an SCF optimisation:

$$n_{new}(\boldsymbol{G}) = n_{in}(\boldsymbol{G}) + A\frac{\boldsymbol{G}^2}{\boldsymbol{G}^2 + \boldsymbol{G}_{max}^2}(n_{out}(\boldsymbol{G}) - n_{in}(\boldsymbol{G})), \tag{5.42}$$

where A is the mixing amplitude and $\boldsymbol{G}_{max}$ is the cutoff wavevector. It is noted that the Kerker preconditioner is constructed with no reference to exchange and correlation. In the computation of the longitudinal spin response, the aforementioned parameters have been adjusted in attempts to achieve a self-consistent solution.

5.5 Spin Density Response Spectra

This section will demonstrate the capabilities of the scheme developed in computing longitudinal spin fluctuations from first principles. No material-specific parameters are considered. The choice of DFT parameters for the ground-state must also be utilised for the spin-polarised solution to the Sternheimer equation, see Cao for more information [194].

5.5.1 Iron

Longitudinal spin fluctuations in bcc-Fe will be presented in this section. The quantity that will be plotted is the imaginary component of the self-consistent, induced magnetisation $\{\chi_z''(\boldsymbol{q},\omega)\}$. This is computed along the frequency axis for a specified $\boldsymbol{q}$ vector. The DFT computational parameters involve a plane-wave cutoff of 1200 eV and an MP grid of $\{16 \times 16 \times 16\}$. The fine grid scale multiplicative factor utilised in these computations is 7.0 with a 5000 eV cutoff used for DM. These parameters ensure that any high $|\boldsymbol{G}|$ components which contribute to the self-consistent response are taken into account. The computations make use of the norm-conserving, on-the-fly generated (OTFG) pseudopotentials, a functionality built in CASTEP. Gaussian smearing is employed with a smearing width of 0.15 eV. Calculation of the ground-state yields the expectant ferromagnetic magnetisation with a value of 2.24 $[\hbar/2]$ per atom [96].

Figure 5.4 presents the imaginary component of the self-consistent response for $\boldsymbol{q} = (0.15, 0.00, 0.00)$ in fractional coordinates. The frequencies at $\omega = 0.7$ eV and $\omega = 0.8$ eV indicate a spectral feature however self-consistency was not reached for these frequencies. The figures of 5.5 and 5.6 illustrate the change in the second-order energy, for each iteration in the SCF process, at these frequencies. It is reminded that the change is of interest here, ΔE_2 is used for the SCF check as shown in the flowchart of 5.3.

The self-consistent tolerance parameter used for these computations is $1e-6$. In order to satisfy self-consistency, the mixing amplitudes used in these computations are small, meaning a relatively small amount of charge and spin density is mixed into the new densities relative to the default setting. This should result in a slow but stable convergence behaviour. Whilst this is achieved for other frequencies, the figure of 5.5 at $\omega = 0.7$ eV shows an overall downward trend to convergence. However, the change even after 500 iterations is still orders of magnitude above the intended tolerance factor. The convergence of ΔE_2 for $\omega = 0.8$ eV for the same choice of DM parameters indicates unstable behaviour. Multiple tests and

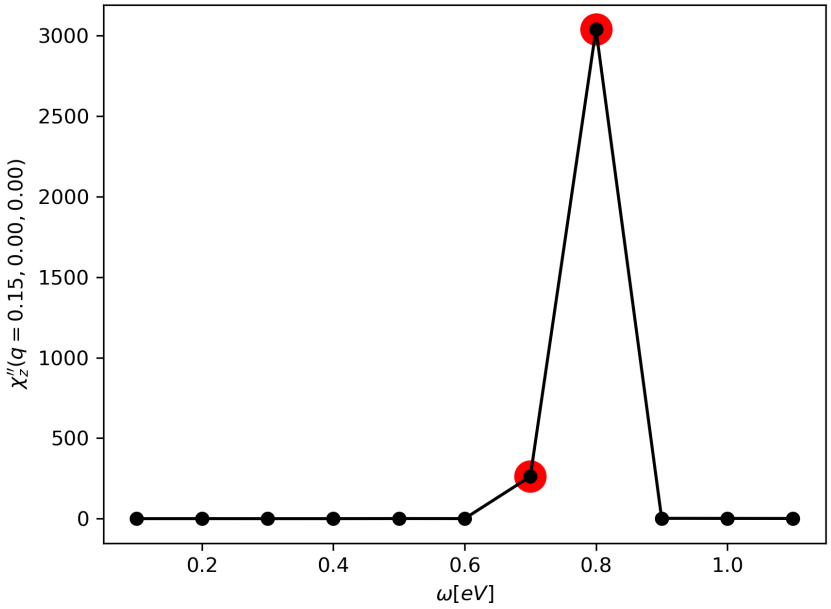

Fig. 5.4 Longitudinal spin dynamics for Bcc-Fe along the $(1,0,0)$ direction, the highlighted points at $\omega = 0.7$ and $\omega = 0.8$ failed to satisfy the criteria for self-consistency.

tuning of the DM parameters at this frequency are not sufficient to resolve the convergence behaviour for these specific frequencies.

In order to resolve the behaviour at the offending frequencies it is proposed to slightly offset the self-consistent computation along the frequency axis. There is no inter-frequency dependence in the Sternheimer/sum-over-states scheme and so this approach is valid, so long as equivalent DFT parameters and ground-state are utilised. Figure 5.7 shows the modified spectra in which all points have met the requirement for self-consistency. In an attempt to further resolve the spectral feature, a relatively dense sampling of the frequency is used between $\omega = [0.7 - 0.8]$ eV. There is a clear peak at $\omega = 0.78$ eV, the extra points computed around the peak illustrate that this collective mode has a very narrow energy band with the susceptibility quickly falling before and after the main peak. Figure 5.8 illustrates the convergence behaviour for the main peak at $\omega = 0.78$ eV.

Discussions of the longitudinal spin dynamics computed from a purely *ab initio* approach are scarce in literature as there is more focus on the transverse susceptibility for magnon modelling. However, work by Wysocki *et al* [211] and Buckzek *et al* [212] have investigated longitudinal fluctuations of the magnetisation. The formalism used by Buczek [212] involves time-dependent density functional theory based on the Korringa-Kohn-Rosotoker (KKR)

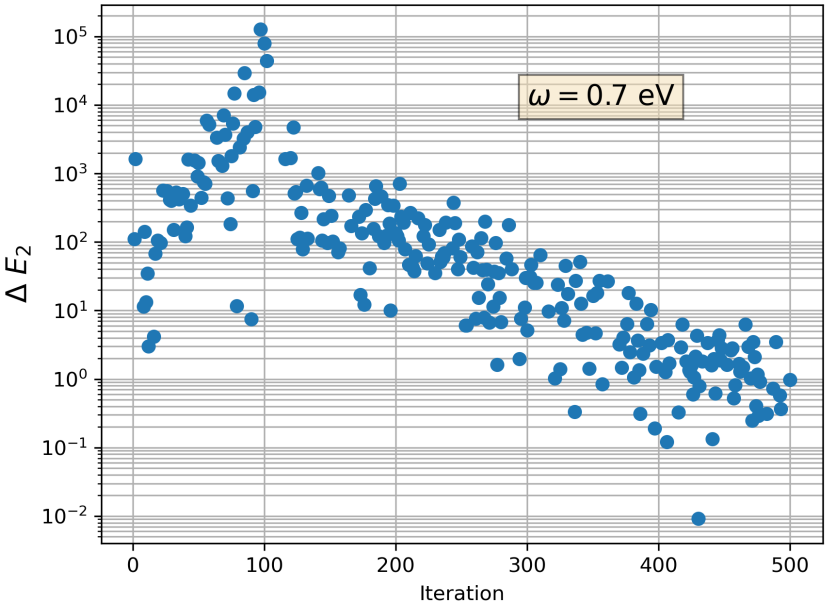

Fig. 5.5 Behaviour of ΔE_2 in Bcc-Fe for $\omega = 0.7$ eV.

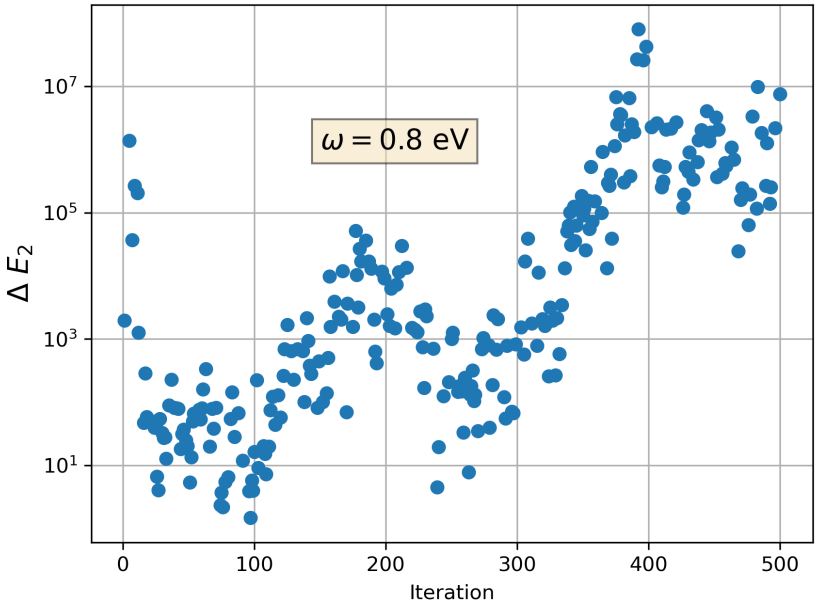

Fig. 5.6 Behaviour of ΔE_2 in Bcc-Fe for $\omega = 0.8$ eV.

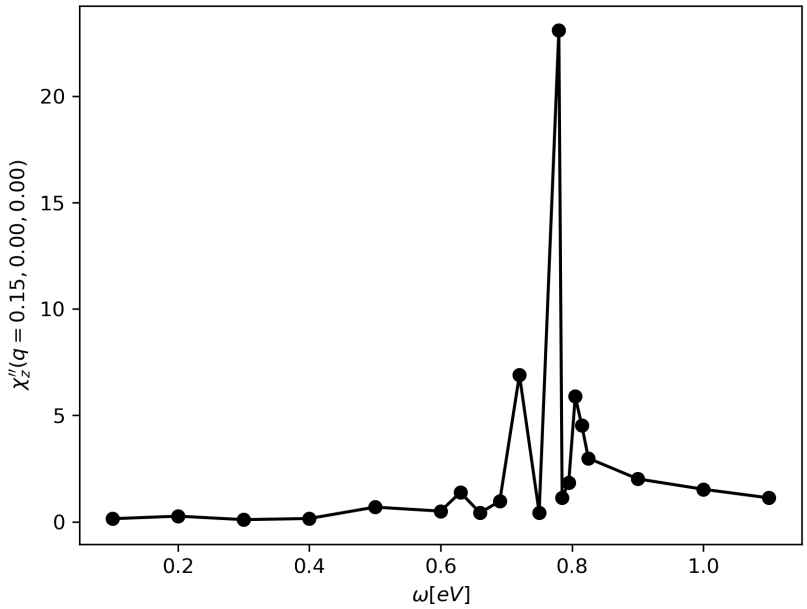

Fig. 5.7 Longitudinal spin dynamics for Bcc-Fe along the $(1,0,0)$ direction, dense frequency sampling of the self-consistent response between $\omega = [0.7 - 0.8]$ eV.

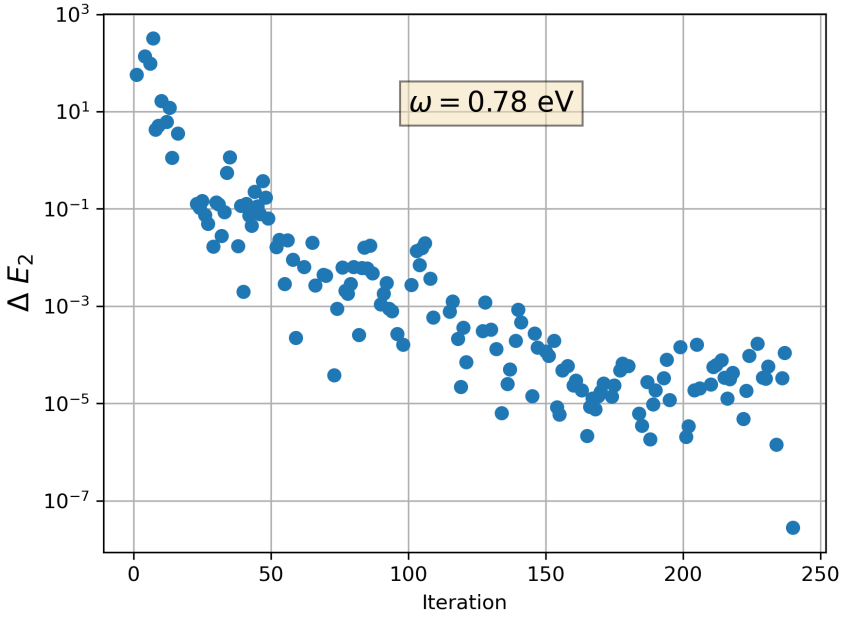

Fig. 5.8 Behaviour of ΔE_2 in Bcc-Fe for $\omega = 0.78$ eV.

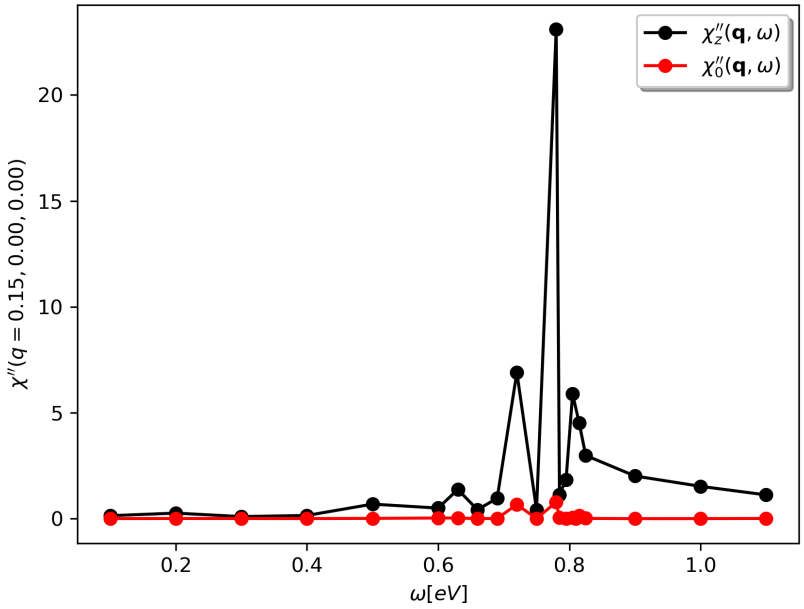

Fig. 5.9 Longitudinal and Charge dynamics plotted for Bcc-Fe in $(1,0,0)$ direction.

method in evaluating the Kohn-Sham Green's function [213]. The *enhanced susceptibility* is the term used by Buczek to describe the susceptibility with both Hartree and XC functional contributions, this is equivalent to the self-consistent response formulated in this scheme. The susceptibility in Buczek's work for the same momentum transfer of $\boldsymbol{q} = (0.15, 0.00, 0.00)$ also shows a single peak albeit at a much lower frequency of $\omega \approx 0.35$ eV.

The charge dynamics are accessible through the computation of the self-consistent charge susceptibility:

$$\chi''_0(\boldsymbol{q},\omega) = Im[\delta n^{\boldsymbol{q}}_{scf}(\boldsymbol{G}=0,\omega)] \tag{5.43}$$

Figure 5.9 shows both $\chi''_0(\boldsymbol{q},\omega)$, $\chi''_z(\boldsymbol{q},\omega)$ and there is a clear decoupling shown here between the two. The charge dynamics are effectively zero in comparison to the longitudinal magnetisation. This is in agreement with the findings of Buczek [212].

The workflow to obtain spectra illustrating longitudinal spin dynamics is summarised. An initial computation of the susceptibility is carried out to trace any potential frequency peaks. Frequencies at which self-consistency is not met are indications of significant structure in the Kohn-Sham map (perhaps a pole in the Kohn-Sham response). This is a reasonable assumption since the analysis of the convergence behaviour at these frequencies indicates

instability which is a symptom of an ill-conditioned problem. Despite the adjustment of the DM parameters, this issue remains. Consequently, additional computations are carried out at offset frequencies and upon reaching a self-consistent response, the imaginary part of the susceptibility is plotted.

5.5.2 Nickel

The longitudinal spin dynamics in fcc-Ni are now presented and the same momentum transfer of $\boldsymbol{q} = (0.15, 0.00, 0.00)$ is used. The DFT computational parameters include a 1200 eV cutoff with an MP grid of $\{16 \times 16 \times 16\}$. The fine grid scale multiplicative factor utilised in these computations is 7.0 with a 5000 eV cutoff used for the density mixing scheme. In order to achieve sufficient minimisation of the second-order energy, small mixing amplitudes are used for both the charge and spin density. Gaussian smearing is employed to treat fractional occupations with a broadening of 0.20 eV. Computations of the ground-state using the norm-conserving OTFG pseudopotential yield a ferromagnetic ground-state of 0.63 $[\hbar/2]$ per atom.

Figure 5.10 illustrates both charge and longitudinal spin response functions for a finite $\boldsymbol{q}$. The spectrum is dominated by the presence of a single strong peak at $\omega = 0.45$ eV. In a similar manner to bcc-Fe, computations of the self-consistent density in the [0.4-0.5] eV range (close to the main peak) are numerically unstable and the behaviour shown in figure 5.5 is found. Again the proposed solution is to slightly offset the frequency grid. Similarly to bcc-Fe, the decoupling between the charge and longitudinal spin susceptibilities is also shown here. The results for fcc-Ni are quantitatively similar to Buczek's computation of the enhanced susceptibility. Computations by Buczek for an equivalent $\boldsymbol{q}$-direction show a single peak in χ_z at a slightly higher $\omega \approx 0.54$ eV.

The peaks found in $\chi_z''(\boldsymbol{q}, \omega)$ are regarded as *collective excitations* since they are formed upon the inclusion of electronic interaction computed through the self-consistent process in the Sternheimer scheme. It is highlighted again here that the XC term involved in the update of the KS potential, shown in the third line of equation (5.20), is solely responsible for modelling the interacting spin-dependent electron liquid.

Echoing the discussions of Wysocki and Buczek *et al* [211, 212], the longitudinal spin dynamics presented in this work lie at energies much higher than those typically sampled in inelastic neutron scattering experiments. The issue has been one of scientific interest to date. Comparison of the cross-section using the surface-sensitive spin polarised electron energy

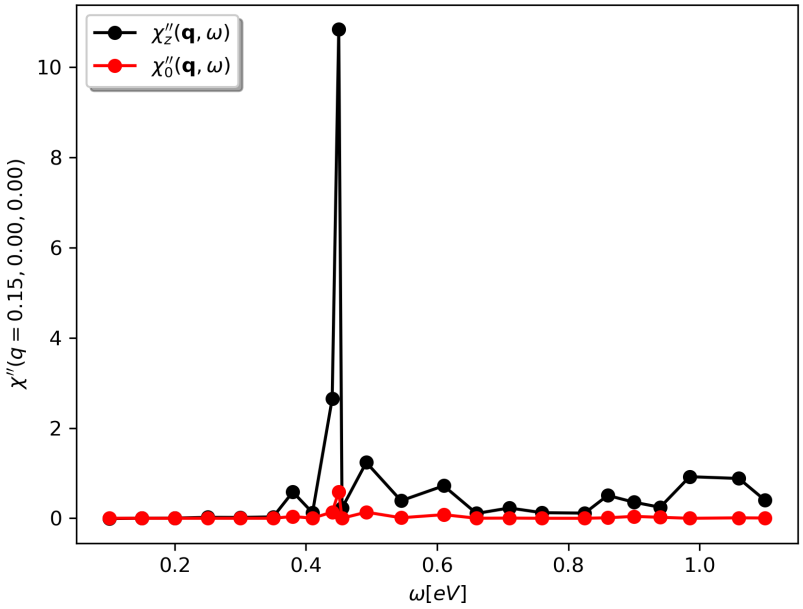

Fig. 5.10 Longitudinal and Charge dynamics plotted for Fcc-Ni in $(1,0,0)$ direction.

loss method to that of the *ab initio* self-consistent response function in bulk systems is an ongoing effort.

5.6 Summary

This chapter has provided the methodology underlying the approach to computing the longitudinal spin response. The scheme involves computing the response wavefunction by using a sum-over-states expansion along with an iterative solution to the Sternheimer equation. The current implementation of this approach has failed to display the fairly rapid SCF convergence behaviour exhibited by phonon and other self-consistent DFPT solvers. This can be attributed to the use of small mixing amplitudes, without which it is not feasible to sufficiently minimise the second-order energy for both systems. It is expressed that an implementation bug cannot be ruled out and there is a discrepancy between these computations and spectra found in the literature [212]. Attempts made in adjusting the DM parameters such as mixing amplitudes have resulted in slow but stable minimisation of the second-order energy. However, in spite of also adjusting the DFT computational parameters which include smearing width, MP grid and plane-wave cutoff, it is not possible to achieve self-consistency for certain frequencies that exist around the dominant peak. This was found for both transition metal systems and the minimisation of ΔE_2 at these frequencies is similar to the behaviour illustrated in figure 5.6. This issue was mitigated by computing the response at offset frequencies.

Chapter 6

Conclusions and Perspectives

In this thesis, a perturbative treatment of the Kohn-Sham DFT equations is applied up to first order. The resultant scheme of density functional perturbation theory is implemented to compute the dielectric and longitudinal spin dynamics of a system.

6.1 Summary of work to date

The work completed in this thesis is as follows. The non-self-consistent Sternheimer method has been developed in a fully *ab initio* plane-wave pseudopotential framework. The implementation has been applied to compute the head of the frequency-dependent dielectric matrix at long wavelength $\boldsymbol{q}$ for the prototypical case of Silicon as well as Gallium Arsenide, Zinc Oxide and Methylammonium Lead Triiodide. In order to achieve the level of numerical stability required for the first-order response wavefunctions, a BiCGStab method has been developed to solve the linear system of equations.

The longitudinal spin response function connects a spin-polarised perturbation to the induced magnetisation density. The longitudinal spin dynamics in this approach are computed via a self-consistent solution of the time-dependent Sternheimer equation. Both $(+\boldsymbol{q}, +\omega)$ and $(-\boldsymbol{q}, -\omega)$ channels are solved separately using the BiCGStab algorithm from the dielectric response scheme. In order to treat fractional occupations, Gaussian smearing is utilised along with sum-over-states perturbation theory which includes full, partial and a number of unoccupied states. This was adapted from a DFPT scheme in the CASTEP package concerning phonons. The methodology of this approach is demonstrated by calculating the longitudinal spin spectra of bcc-Fe and fcc-Ni.

The development of these two schemes constitutes novel functionality in the CASTEP package.

6.2 Perspectives

The results of the dielectric response implementation were illustrated in chapter 4 for several semiconductor systems. The computed dielectric spectra were plotted with experimental spectroscopic ellipsometry data. It was shown that for all systems, the overall shape of the dielectric spectra across the frequency range is in good agreement with experimental findings. However, a red-shift is present in all the computational results, i.e. the peaks of the computed dielectric spectra are offset to the left in comparison to the experimental peaks. It is therefore found that the Sternheimer scheme is only as accurate as the underlying DFT band-structure computation. DFT does not adequately describe the band dispersion due to an inherent lack of derivative discontinuity and the delocalisation error discussed in 3.1. Therefore the utilisation of the Kohn-Sham eigenvalues to describe real systems will present a discrepancy. Nevertheless, in accordance with the corresponding DFT band structure, the implementation developed here successfully captures the peaks corresponding to potential transitions. Both real and imaginary parts of the dielectric spectra indicate spectral features at frequency positions which are corroborated by the band structure. There are certain peaks however which are beyond the scope of the implementation, for instance, the experimental imaginary peak for Silicon at $\omega = 3.4$ eV is not reproduced. This is due to the electron-hole interaction which the Sternheimer scheme does not take into account.

The BiCGStab solver used for these computations has been demonstrated to be robust and efficient in minimising the residual norm in order to obtain accurate response wavefunctions. However, the algorithm implicitly requires double the number of operations involving the Hamiltonian (compared to BiCG) in part to obtain the stabilising parameter used to ensure the residual is minimised. Handling the Hamiltonian is a resource-intensive task which means that this solver is more expensive compared to BiCG, however, the issues with stability and minimisation of the residual norm demonstrated for BiCG suggest it is not suitable for this scheme.

The calculations concerning longitudinal spin dynamics can be compared to work by Buczek in computing the enhanced susceptibility using a different time-dependent DFT scheme. The linear response time-dependent DFT method employed by Buczek employs KKR along with the *nearly real axis approach* [214]. This evaluates the KKR Green's function away from the Kohn-Sham poles and utilises an analytic continuation in the form of Padè approximation to revert to the real axis. In comparison, the scheme developed for this thesis computes the

susceptibility for a real frequency (with a small imaginary component) and therefore, no analytic continuation is required. The peaks computed for this implementation do not line up with Buczek's work. For bcc-Fe, a peak is found at a relatively higher frequency and for fcc-Ni, the dominant peak is found at a comparatively lower frequency. However, in agreement with Buczek, there exists a single dominant peak in the magnetisation z channel with the charge dynamics being effectively zero in comparison.

The main limitation in the method developed here in computing the longitudinal spin susceptibility pertains to the difficulty in achieving self-consistency in the density mixing scheme. The approach used to compute self-consistency for the systems presented in this thesis was to use small mixing amplitudes for both the charge and spin densities. As a consequence, the convergence behaviour whilst stable is prohibitively slow and a relatively large number of iterations are required to achieve satisfactory minimisation of the second-order energy. It was typical for the number of self-consistent iterations to reach in excess of 150 SCF cycles, in comparison, self-consistency for spin-polarised phonon computations can be achieved in typically fewer than 50 SCF iterations. At certain frequencies it is unfeasible to obtain self-consistent densities, this is overcome by rerunning the computations at frequencies which are slightly offset.

6.3 Future Work

The scheme to compute the frequency-dependent dielectric response allows for the computation of the screened Coulomb interaction. Section 3.2 discussed the relation between the two quantities. The scheme presented here can be viewed as the first step towards implementing the Sternheimer*GW* method in the CASTEP package. Further work is required to develop the self-consistent framework required for obtaining the self-energy. The other quantity that would need to be developed is the non-interacting Green's function (G_0). Obtaining this involves a similar workflow to that of obtaining the screened Coulomb interaction. The development of BiCG/BiCGStab is also applicable here, as obtaining G_0 also requires solving a linear system of the form $Ax = b$.

As of present, $\boldsymbol{k}$-point parallelism is the main strategy utilised in these computations. In principle, $\boldsymbol{G}$-vector parallelism can also be exploited. This would be suitable for calculations of large simulation systems that require more plane waves and fewer k-points. Optimal performance would be achieved by combining both parallel schemes [112].

It would be beneficial to the potential user to offer a range of Sternheimer solvers in which an option is available to switch to a faster scheme at the price of reliability. Whilst the BiCGStab scheme has been developed and used exclusively in this thesis, there exists a range of Krylov subspace solvers that can be implemented. For instance, the shifted BiCG/BiCGStab methods [176] have been developed in Quantum Espresso's SternhemerGW code. It is noted that whilst BiCG has been shown to be unreliable for the NSCF Sternheimer method developed in this thesis, it may be of use in the self-consistent Sternheimer implementation which yields the inverse dielectric matrix (see sections 3.4 and 4.1).

Further developmental work is required in order to optimise the self-consistency process used to obtain the longitudinal spin response function. It is clear from computations that there exists a numerical deficiency in seeking a fixed-point to the discretised Kohn-Sham map [155, 203]. Currently, the density mixing scheme used in the computation of the ground-state is reused for the DFPT scheme. Investigation into preconditioning techniques and schemes used by other codes may be of use. A more rigorous comparison of the longitudinal spin dynamics computed in this scheme is needed to other methods, both experimental and computational. As of present, there are limited *ab initio* approaches that focus on longitudinal modes, most codes focus on transverse dynamics at low energies in order to model magnons.

Bibliography

[1] J.J. Thomson. “Cathode Rays”. In: *Philosophical Magazine and Journal of Science* (1897). DOI: 10.1080/14786449708621070.

[2] R. A. Millikan. “On the Elementary Electrical Charge and the Avogadro Constant”. In: *Physical Review* 2.2 (Aug. 1, 1913), pp. 109–143. ISSN: 0031-899X. DOI: 10.1103/PhysRev.2.109.

[3] Max Planck. “On the Law of Distribution of Energy in the Normal Spectrum”. In: *Annalen der Physik* 309.3 (1900), pp. 553–563.

[4] Louis de Broglie. “Recherches sur la théorie des quanta”. In: *Annales de Physique* 3.3 (1924), pp. 22–128.

[5] E. Schrödinger. “An Undulatory Theory of the Mechanics of Atoms and Molecules”. In: *Physical Review* 28.6 (Dec. 1, 1926), pp. 1049–1070. ISSN: 0031-899X. DOI: 10.1103/PhysRev.28.1049.

[6] W. Heisenberg. “Ber Den anschaulichen inhalt der quantentheoretischen kinematik und mechanik”. In: *Zeitschrift fur Physik* 43.3–4 (1927), pp. 172–198. DOI: 10.1007/bf01397280.

[7] Paul A. M. Dirac. “The Quantum Theory of the Emission and Absorption of Radiation”. In: *Proceedings of the Royal Society A* 114.767 (1927), pp. 243–265. DOI: 10.1098/rspa.1927.0039.

[8] Paul A.M. Dirac. “The Quantum Theory of the Electron”. In: *Proceedings of the Royal Society A* 117.778 (1928), pp. 610–624. DOI: 10.1098/rspa.1928.0023.

[9] Richard M. Martin. *Electronic Structure: Basic Theory and Practical Methods*. Cambridge University Press, 2004. DOI: 10.1017/CBO9780511805769.

[10] Eric Winsberg. “Computer Simulations in Science”. In: *The Stanford Encyclopedia of Philosophy*. Ed. by Edward N. Zalta and Uri Nodelman. Winter 2022. Metaphysics Research Lab, Stanford University, 2022.

[11] Kevin Leung. “Electronic Structure Modeling of Electrochemical Reactions at Electrode/Electrolyte Interfaces in Lithium Ion Batteries”. In: *The Journal of Physical Chemistry C* 117.4 (Jan. 31, 2013), pp. 1539–1547. ISSN: 1932-7447, 1932-7455. DOI: 10.1021/jp308929a. arXiv: 1304.5976 [cond-mat].

[12] H. Euchner and A. Groß. “Atomistic modeling of Li- and post-Li-ion batteries”. In: *Phys. Rev. Mater.* 6 (4 2022), p. 040302. DOI: 10.1103/PhysRevMaterials.6.040302.

[13] Vishnu Sudarsanan, Anu Maria Augustine, and P. Ravindran. "Investigation of Electronic Structure and Electrochemical Properties of Na2MnSiO4 as a Cathode Material for Na Ion Batteries". In: *The Journal of Physical Chemistry C* 125.47 (Dec. 2, 2021), pp. 25968–25982. ISSN: 1932-7447. DOI: 10.1021/acs.jpcc.1c07386.

[14] Shuang Zhao et al. "Modulating the Electronic Structure of Nanomaterials to Enhance Polysulfides Confinement for Advanced Lithium–Sulfur Batteries". In: *Journal of Materials Chemistry A* 9.35 (2021), pp. 18927–18946. ISSN: 2050-7488, 2050-7496. DOI: 10.1039/D1TA02741G.

[15] Gabriele Giuliani and Giovanni Vignale. *Quantum Theory of the Electron Liquid*. Cambridge University Press, 2005. DOI: 10.1017/CBO9780511619915.

[16] Ye Luo and Sandro Sorella. "Ab Initio Molecular Dynamics with Quantum Monte Carlo". In: *Frontiers in Materials* 2 (Apr. 7, 2015). ISSN: 2296-8016. DOI: 10.3389/fmats.2015.00029.

[17] J. C. Slater. "A Simplification of the Hartree-Fock Method". In: *Physical Review* 81.3 (Feb. 1, 1951), pp. 385–390. ISSN: 0031-899X. DOI: 10.1103/PhysRev.81.385.

[18] Feliciano Giustino. *Materials Modelling using Density Functional Theory: Properties and Predictions*. Oxford University Press, 2014. ISBN: 9780199662449.

[19] P. Hohenberg and W. Kohn. "Inhomogeneous Electron Gas". In: *Physical Review* 136 (3B Nov. 9, 1964), B864–B871. ISSN: 0031-899X. DOI: 10.1103/PhysRev.136.B864.

[20] L. J. Sham and W. Kohn. "One-Particle Properties of an Inhomogeneous Interacting Electron Gas". In: *Physical Review* 145.2 (May 13, 1966), pp. 561–567. ISSN: 0031-899X. DOI: 10.1103/PhysRev.145.561.

[21] R. O. Jones. "Density Functional Theory: Its Origins, Rise to Prominence, and Future". In: *Reviews of Modern Physics* 87.3 (Aug. 25, 2015), pp. 897–923. ISSN: 0034-6861, 1539-0756. DOI: 10.1103/RevModPhys.87.897.

[22] C. David Sherrill and Henry F. Schaefer. "The Configuration Interaction Method: Advances in Highly Correlated Approaches". In: ed. by Per-Olov Löwdin et al. Vol. 34. Advances in Quantum Chemistry. Academic Press, 1999, pp. 143–269. DOI: https://doi.org/10.1016/S0065-3276(08)60532-8.

[23] W. Kohn and L. J. Sham. "Self-Consistent Equations Including Exchange and Correlation Effects". In: *Physical Review* 140 (4A Nov. 15, 1965), A1133–A1138. ISSN: 0031-899X. DOI: 10.1103/PhysRev.140.A1133.

[24] Robin Haunschild, Andreas Barth, and Bernie French. "A Comprehensive Analysis of the History of DFT Based on the Bibliometric Method RPYS". In: *Journal of Cheminformatics* 11.1 (Dec. 2019), p. 72. ISSN: 1758-2946. DOI: 10.1186/s13321-019-0395-y.

[25] O. Gunnarsson and P. Johansson. "Spin-density functional formalism for quantum-mechanical calculations—Test on diatomic molecules with an efficient numerical method". In: *International Journal of Quantum Chemistry* 10 (1976), pp. 307–323. DOI: 10.1002/qua.560100209.

[26] U von Barth and L Hedin. "A Local Exchange-Correlation Potential for the Spin Polarized Case. i". In: *Journal of Physics C: Solid State Physics* 5.13 (July 10, 1972), pp. 1629–1642. ISSN: 0022-3719. DOI: 10.1088/0022-3719/5/13/012.

[27] O Gunnarsson and R O Jones. “Density Functional Calculations for Atoms, Molecules and Clusters”. In: *Physica Scripta* 21.3-4 (Jan. 1, 1980), pp. 394–401. ISSN: 0031-8949, 1402-4896. DOI: 10.1088/0031-8949/21/3-4/027.

[28] Benny G. Johnson, Peter M. W. Gill, and John A. Pople. “The Performance of a Family of Density Functional Methods”. In: *The Journal of Chemical Physics* 98.7 (Dec. 16, 1992), pp. 5612–5626. ISSN: 0021-9606, 1089-7690. DOI: 10.1063/1.464906.

[29] E. Anderson et al. *LAPACK Users' Guide*. Third. Philadelphia, PA: Society for Industrial and Applied Mathematics, 1999. ISBN: 0-89871-447-8 (paperback).

[30] Message Passing Interface Forum. *MPI: A Message-Passing Interface Standard Version 4.0*. 2021. URL: https://www.mpi-forum.org/docs/mpi-4.0/mpi40-report.pdf.

[31] R. Car and M. Parrinello. “Unified Approach for Molecular Dynamics and Density-Functional Theory”. In: *Physical Review Letters* 55.22 (Nov. 25, 1985), pp. 2471–2474. ISSN: 0031-9007. DOI: 10.1103/PhysRevLett.55.2471.

[32] Jürgen Hafner. “A Joint Effort with Lasting Impact”. In: *Nature Materials* 9.9 (Sept. 2010), pp. 690–692. ISSN: 1476-1122, 1476-4660. DOI: 10.1038/nmat2838.

[33] Chuan-Jia Tong et al. “Density Functional Theory and Experimental Determination of Band Gaps and Lattice Parameters in Kesterite $Cu_2ZnSn(S_xSe_{1-x})_4$”. In: *The Journal of Physical Chemistry Letters* 11.24 (Dec. 17, 2020), pp. 10463–10468. ISSN: 1948-7185, 1948-7185. DOI: 10.1021/acs.jpclett.0c03205.

[34] Annika Stuke et al. “Atomic Structures and Orbital Energies of 61,489 Crystal-Forming Organic Molecules”. In: *Scientific Data* 7.1 (Feb. 18, 2020), p. 58. ISSN: 2052-4463. DOI: 10.1038/s41597-020-0385-y.

[35] Hossein Tavakol. “Study of Binding Energies Using DFT Methods, Vibrational Frequencies and Solvent Effects in the Interaction of Silver Ions with Uracil Tautomers”. In: *Arabian Journal of Chemistry* 10 (Feb. 2017), S786–S799. ISSN: 18785352. DOI: 10.1016/j.arabjc.2012.12.007.

[36] Jagannath Pal, Arnab Patla, and Ranga Subramanian. “Thermodynamic properties of forming methanol-water and ethanol-water clusters at various temperatures and pressures and implications for atmospheric chemistry: A DFT study”. In: *Chemosphere* 272 (2021), p. 129846. ISSN: 0045-6535. DOI: https://doi.org/10.1016/j.chemosphere.2021.129846.

[37] Evan Kiely et al. “Density Functional Theory Predictions of the Mechanical Properties of Crystalline Materials”. In: *CrystEngComm* 23.34 (2021), pp. 5697–5710. ISSN: 1466-8033. DOI: 10.1039/D1CE00453K.

[38] Wei Hu et al. “High performance computing of DGDFT for tens of thousands of atoms using millions of cores on Sunway TaihuLight”. In: *Science Bulletin* 66.2 (2021), pp. 111–119. ISSN: 2095-9273. DOI: https://doi.org/10.1016/j.scib.2020.06.025.

[39] John L. Gustafson. “Moore's Law”. In: *Encyclopedia of Parallel Computing*. Ed. by David Padua. Boston, MA: Springer US, 2011, pp. 1177–1184. ISBN: 978-0-387-09766-4. DOI: 10.1007/978-0-387-09766-4_81.

[40] Phil Hasnip and Ed Higgins. “OPTIMISING CASTEP ON INTEL'S KNIGHT'S LANDING PLATFORM TECHNICAL REPORT FOR ECSE11-17”. In: *Embedded CSE support ARCHER Technical Report* (Apr. 2019).

[41] David Padua. *FFTW*. Ed. by David Padua. Boston, MA: Springer US, 2011, pp. 671–671. DOI: 10.1007/978-0-387-09766-4_397.

[42] *Frontier High-Performance Computing System*. Oak Ridge Leadership Computing Facility. URL: https://docs.olcf.ornl.gov/systems/frontier_user_guide.html. 2023.

[43] J. Dongarra et al. "LINPACK: A Linear Algebra Package for High-Performance Computers". In: *SIAM Journal on Scientific and Statistical Computing* 8.1 (1987), pp. 62–68. DOI: 10.1137/0908005.

[44] P. A. Simionescu and Mehrube Mehrubeoglu. "New Concepts on Two-Dimensional Data Visualization With Applications in Engineering Analysis and Design". In: *Journal of Computing and Information Science in Engineering* 12.2 (June 1, 2012), p. 024501. ISSN: 1530-9827, 1944-7078. DOI: 10.1115/1.4006204.

[45] M. C. Payne et al. "Iterative Minimization Techniques for *Ab Initio* Total-Energy Calculations: Molecular Dynamics and Conjugate Gradients". In: *Reviews of Modern Physics* 64.4 (Oct. 1, 1992), pp. 1045–1097. ISSN: 0034-6861, 1539-0756. DOI: 10.1103/RevModPhys.64.1045.

[46] Jack Dongarra. *Performance of Various Computers Using Standard Linear Equations Software*. Tech. rep. CS-89-85. University of Tennessee, Knoxville TN, 1989. URL: http://www.netlib.org/benchmark/performance.ps.

[47] TOP500. *TOP500 - LINPACK Benchmark*. URL: https://www.top500.org/. 2023.

[48] Bronson E Messer II. *Simulating a more detailed universe with Frontier ORNL*. URL: https://www.ornl.gov/news/simulating-more-detailed-universe-frontier/. 2023.

[49] E3SM Project. *Energy Exascale Earth System Model (E3SM)*. [Computer Software] https://dx.doi.org/10.11578/E3SM/dc.20230110.5. Jan. 2023. DOI: 10.11578/E3SM/dc.20230110.5.

[50] Oliver Peckham. *Frontier Supercomputer Powers 'SCREAM' Climate Model*. hpcwire - URL: https://www.hpcwire.com/2023/04/07/frontier-supercomputer-powers-scream-climate-model/. 2023.

[51] Stephen Ezell. *A New Frontier: Sustaining U.S. High-Performance Computing Leadership in an Exascale Era*. Sept. 12, 2022.

[52] Vikram Gavini et al. *Roadmap on Electronic Structure Codes in the Exascale Era*. Sept. 26, 2022. arXiv: 2209.12747 [cond-mat, physics:physics]. preprint.

[53] Ada Sedova et al. *HPC Molecular Simulation Tries Out a New GPU: Experiences on Early AMD Test Systems for the Frontier Supercomputer*. 2022. URL: https://www.osti.gov/biblio/1883870.

[54] Karol Kowalski et al. "From NWChem to NWChemEx: Evolving with the Computational Chemistry Landscape". In: *Chemical Reviews* 121.8 (Apr. 28, 2021), pp. 4962–4998. ISSN: 0009-2665. DOI: 10.1021/acs.chemrev.0c00998.

[55] Choongseok Chang et al. "Simulations in the Era of Exascale Computing". In: *Nature Reviews Materials* 8.5 (Mar. 13, 2023), pp. 309–313. ISSN: 2058-8437. DOI: 10.1038/s41578-023-00540-6.

[56] T.G. Perring, A.D. Taylor, and G.L. Squires. "High-Energy Spin Waves in Hexagonal Cobalt". In: *Physica B: Condensed Matter* 213–214 (Aug. 1995), pp. 348–350. ISSN: 09214526. DOI: 10.1016/0921-4526(95)92829-Y.

[57] Hiroyuki Fujiwara. *Spectroscopic Ellipsometry: Principles and Applications*. 1st ed. Wiley, Jan. 26, 2007. DOI: 10.1002/9780470060193.

[58] R. L. Hengehold, R. J. Almassy, and F. L. Pedrotti. "Electron Energy-Loss and Ultraviolet-Reflectivity Spectra of Crystalline ZnO". In: *Physical Review B* 1.12 (June 15, 1970), pp. 4784–4791. ISSN: 0556-2805. DOI: 10.1103/PhysRevB.1.4784.

[59] B. Lake, D. A. Tennant, and S. E. Nagler. "Longitudinal Magnetic Dynamics and Dimensional Crossover in the Quasi-One-Dimensional Spin- 1 2 Heisenberg Antiferromagnet KCuF 3". In: *Physical Review B* 71.13 (Apr. 15, 2005), p. 134412. ISSN: 1098-0121, 1550-235X. DOI: 10.1103/PhysRevB.71.134412.

[60] R Kubo. "The fluctuation-dissipation theorem". In: *Reports on Progress in Physics* 29.1 (1966), p. 255. DOI: 10.1088/0034-4885/29/1/306.

[61] Robert van Leeuwen. "Mapping from Densities to Potentials in Time-Dependent Density-Functional Theory". In: *Physical Review Letters* 82.19 (May 10, 1999), pp. 3863–3866. ISSN: 0031-9007, 1079-7114. DOI: 10.1103/PhysRevLett.82.3863.

[62] Robert L. Peterson. "Formal Theory of Nonlinear Response". In: *Reviews of Modern Physics* 39.1 (Jan. 1, 1967), pp. 69–77. ISSN: 0034-6861. DOI: 10.1103/RevModPhys.39.69.

[63] David A. Strubbe et al. "Response Functions in TDDFT: Concepts and Implementation". In: *Fundamentals of Time-Dependent Density Functional Theory*. Ed. by Miguel A.L. Marques et al. Vol. 837. Berlin, Heidelberg: Springer Berlin Heidelberg, 2012, pp. 139–166. DOI: 10.1007/978-3-642-23518-4_7.

[64] R. M. Sternheimer. "Electronic Polarizabilities of Ions from the Hartree-Fock Wave Functions". In: *Physical Review* 96.4 (Nov. 15, 1954), pp. 951–968. ISSN: 0031-899X. DOI: 10.1103/PhysRev.96.951.

[65] Thorbjørn Skovhus and Thomas Olsen. "Dynamic Transverse Magnetic Susceptibility in the Projector Augmented-Wave Method. Application to Fe, Ni, and Co". May 12, 2021. arXiv: 2103.05409 [cond-mat].

[66] S. Y. Savrasov. "Linear Response Calculations of Spin Fluctuations". In: *Physical Review Letters* 81.12 (Sept. 21, 1998), pp. 2570–2573. ISSN: 0031-9007, 1079-7114. DOI: 10.1103/PhysRevLett.81.2570.

[67] Ryogo Kubo. "Statistical-Mechanical Theory of Irreversible Processes. I. General Theory and Simple Applications to Magnetic and Conduction Problems". In: *Journal of the Physical Society of Japan* 12.6 (1957), pp. 570–586.

[68] Erich Runge and E. K. U. Gross. "Density-Functional Theory for Time-Dependent Systems". In: *Physical Review Letters* 52.12 (Mar. 19, 1984), pp. 997–1000. ISSN: 0031-9007. DOI: 10.1103/PhysRevLett.52.997.

[69] Kieron Burke, Jan Werschnik, and E. K. U. Gross. "Time-Dependent Density Functional Theory: Past, Present, and Future". In: *The Journal of Chemical Physics* 123.6 (Aug. 8, 2005), p. 062206. ISSN: 0021-9606, 1089-7690. DOI: 10.1063/1.1904586.

[70] Manfred Lein, E. K. U. Gross, and John P. Perdew. "Electron Correlation Energies from Scaled Exchange-Correlation Kernels: Importance of Spatial versus Temporal Nonlocality". In: *Physical Review B* 61.20 (May 15, 2000), pp. 13431–13437. ISSN: 0163-1829, 1095-3795. DOI: 10.1103/PhysRevB.61.13431.

[71] P J Stephens et al. "Determination of absolute configuration using concerted ab Initio DFT calculations of electronic circular dichroism and optical rotation: bicyclo[3.3.1]nonane diones". In: *Journal of Organic Chemistry* 69.6 (2004), pp. 1948–1958. DOI: 10.1021/jo0357061.

[72] Filippo Angelis, Simona Fantacci, and Annabella Selloni. "Time-dependent density functional theory study of the absorption spectrum of [Ru(4,4-COOH-2,2-bpy)2(NCS)2] in water solution: Influence of the pH". In: *Chemical Physics Letters* 389 (May 2004), pp. 204–208. DOI: 10.1016/j.cplett.2004.03.074.

[73] Talgat M. Inerbaev et al. "Excited State Properties and Quadratic Optical Nonlinearities in Charged Organic Chromophores: Theoretical Analysis". In: *The Journal of Chemical Physics* 125.23 (Dec. 21, 2006), p. 234702. ISSN: 0021-9606, 1089-7690. DOI: 10.1063/1.2403864.

[74] K. Yabana and G. F. Bertsch. "Optical response of small silver clusters". In: *Phys. Rev. A* 60 (5 1999), pp. 3809–3814. DOI: 10.1103/PhysRevA.60.3809.

[75] K. Yabana and G. F. Bertsch. "Time-Dependent Local-Density Approximation in Real Time: Application to Conjugated Molecules". In: *International Journal of Quantum Chemistry* 75.1 (1999), pp. 55–66. ISSN: 0020-7608, 1097-461X. DOI: 10.1002/(SICI)1097-461X(1999)75:1<55::AID-QUA6>3.0.CO;2-K.

[76] Fabian Hofmann, Ingo Schelter, and Stephan Kümmel. "Linear Response Time-Dependent Density Functional Theory without Unoccupied States: The Kohn-Sham-Sternheimer Scheme Revisited". In: *The Journal of Chemical Physics* 149.2 (July 14, 2018), p. 024105. ISSN: 0021-9606, 1089-7690. DOI: 10.1063/1.5030652.

[77] M. E. Casida. "Time-Dependent Density Functional Response Theory for Molecules". In: *Recent Advances in Density Functional Theory, Vol. I*. Ed. by D. P. Chong. World Scientific, 1995. DOI: 10.1142/9789812830586_0005.

[78] Mark E. Casida et al. "Molecular excitation energies to high-lying bound states from time-dependent-density-functional response theory: Characterization and correction of the time-dependent local density approximation ionization threshold". In: *The Journal of Chemical Physics* 108.11 (Mar. 1998), pp. 4439–4449. ISSN: 0021-9606. DOI: 10.1063/1.475855.

[79] Jonas Greiner and Dage Sundholm. "Calculation of Vibrationally Resolved Absorption and Fluorescence Spectra of the Rylenes". In: *Physical Chemistry Chemical Physics* 22.4 (2020), pp. 2379–2385. ISSN: 1463-9076, 1463-9084. DOI: 10.1039/C9CP06089H.

[80] Xavier Andrade et al. "A Time-Dependent Density Functional Theory Scheme for Efficient Calculations of Dynamic (Hyper)Polarizabilities". Jan. 25, 2007. DOI: 10.1063/1.2733666. arXiv: cond-mat/0701632.

[81] Professor David Tong. *Lectures on Theoretical Physics - Kinetic Theory*. 2012.

[82] Qi Tan, Pat Irwin, and Yang Cao. "Advanced Dielectrics for Capacitors". In: *Ieej Transactions on Fundamentals and Materials* 126 (Jan. 2006), pp. 1153–1159. DOI: 10.1541/ieejfms.126.1153.

[83] G Gautham Prasad et al. "Supercapacitor technology and its applications: a review". In: *IOP Conference Series: Materials Science and Engineering* 561 (Nov. 2019), p. 012105. DOI: 10.1088/1757-899X/561/1/012105.

[84] A Buzulutskov et al. “Study of photocathode protection with thin dielectric films”. In: *Nuclear Instruments and Methods in Physics Research Section A: Accelerators, Spectrometers, Detectors and Associated Equipment* 371.1 (1996). Proceedings of the Second International Workshop on Ring Imaging Cherenkov Detectors, pp. 147–150. ISSN: 0168-9002. DOI: https://doi.org/10.1016/0168-9002(95)01148-X. URL: https://www.sciencedirect.com/science/article/pii/016890029501148X.

[85] Rajiv Kumar Pandey et al. “Review on ZnO-based piezotronics and piezoelectric nanogenerators: aspects of piezopotential and screening effect”. In: *Journal of Physics: Materials* 4.4 (2021), p. 044011. DOI: 10.1088/2515-7639/ac130a. URL: https://dx.doi.org/10.1088/2515-7639/ac130a.

[86] Jinming Ti et al. “Magnetron sputtering of ZnO thick film for high frequency focused ultrasonic transducer”. In: *Journal of Alloys and Compounds* 933 (2023), p. 167764. ISSN: 0925-8388. DOI: https://doi.org/10.1016/j.jallcom.2022.167764. URL: https://www.sciencedirect.com/science/article/pii/S092583882204155X.

[87] Michael Woodhouse et al. “On the Path to SunShot: The Role of Advancements in Solar Photovoltaic Efficiency, Reliability, and Costs”. In: (2016).

[88] Arie Wibowo et al. “ZnO Nanostructured Materials for Emerging Solar Cell Applications”. In: *RSC Advances* 10.70 (2020), pp. 42838–42859. ISSN: 2046-2069. DOI: 10.1039/D0RA07689A.

[89] E. Grochowski and R. D. Halem. “Technological Impact of Magnetic Hard Disk Drives on Storage Systems”. In: *IBM Systems Journal* 42.2 (2003), pp. 338–346. ISSN: 0018-8670. DOI: 10.1147/sj.422.0338.

[90] Gurney D. “Platinum/Cobalt Multilayers TNE NEXT GENERATION MAGNETO-OPTIC DATA STORAGE MEDIUM”. In: *Platinum Metals Rev* 37.3 (1993), pp. 130–135.

[91] Giovanni Finocchio et al. “The Promise of Spintronics for Unconventional Computing”. In: *Journal of Magnetism and Magnetic Materials* 521 (Mar. 2021), p. 167506. ISSN: 03048853. DOI: 10.1016/j.jmmm.2020.167506.

[92] Dmytro Apalkov, Bernard Dieny, and J. M. Slaughter. “Magnetoresistive Random Access Memory”. In: *Proceedings of the IEEE* 104.10 (2016), pp. 1796–1830. DOI: 10.1109/JPROC.2016.2590142.

[93] Michael J. Caruso. “Applications of Magnetoresistive Sensors in Navigation Systems”. In: *SAE International Congress and Exposition* (Feb. 24, 1997), p. 970602. DOI: 10.4271/970602.

[94] M. Born and R. Oppenheimer. “Zur Quantentheorie der Molekeln”. In: *Annalen der Physik* 389.20 (1927), pp. 457–484. DOI: https://doi.org/10.1002/andp.19273892002.

[95] J. Harris. “Simplified method for calculating the energy of weakly interacting fragments”. In: *Phys. Rev. B* 31 (4 Feb. 1985), pp. 1770–1779. DOI: 10.1103/PhysRevB.31.1770.

[96] J.K. Kübler. *Theory of Itinerant Electron Magnetism*. International series of monographs on physics. Oxford University Press, 2021. ISBN: 9780191915833. URL: https://books.google.co.uk/books?id=ubtSzwEACAAJ.

[97] A. K. Rajagopal and J. Callaway. "Inhomogeneous Electron Gas". In: *Physical Review B* 7.5 (Mar. 1, 1973), pp. 1912–1919. ISSN: 0556-2805. DOI: 10.1103/PhysRevB.7.1912.

[98] J. P. Perdew and Alex Zunger. "Self-Interaction Correction to Density-Functional Approximations for Many-Electron Systems". In: *Physical Review B* 23.10 (May 15, 1981), pp. 5048–5079. ISSN: 0163-1829. DOI: 10.1103/PhysRevB.23.5048.

[99] John P. Perdew and Yue Wang. "Accurate and Simple Analytic Representation of the Electron-Gas Correlation Energy". In: *Physical Review B* 45.23 (June 15, 1992), pp. 13244–13249. ISSN: 0163-1829, 1095-3795. DOI: 10.1103/PhysRevB.45.13244.

[100] John P. Perdew et al. "Atoms, Molecules, Solids, and Surfaces: Applications of the Generalized Gradient Approximation for Exchange and Correlation". In: *Physical Review B* 46.11 (Sept. 15, 1992), pp. 6671–6687. ISSN: 0163-1829, 1095-3795. DOI: 10.1103/PhysRevB.46.6671.

[101] John P. Perdew, Kieron Burke, and Matthias Ernzerhof. "Generalized Gradient Approximation Made Simple". In: *Phys. Rev. Lett.* 77 (18 1996), pp. 3865–3868. DOI: 10.1103/PhysRevLett.77.3865.

[102] John P. Perdew, Kieron Burke, and Yue Wang. "Generalized Gradient Approximation for the Exchange-Correlation Hole of a Many-Electron System". In: *Physical Review B* 54.23 (Dec. 15, 1996), pp. 16533–16539. ISSN: 0163-1829, 1095-3795. DOI: 10.1103/PhysRevB.54.16533.

[103] Eberhard K. U. Gross and Neepa T. Maitra. "Introduction to TDDFT". In: *Fundamentals of Time-Dependent Density Functional Theory*. Ed. by Miguel A.L. Marques et al. Vol. 837. Lecture Notes in Physics. Berlin, Heidelberg: Springer Berlin Heidelberg, 2012, pp. 53–99. DOI: 10.1007/978-3-642-23518-4_4.

[104] Miguel A. L. Marques and E. K. Uwe Gross. "Time-dependent density functional theory". In: *Annual Review of Physical Chemistry* 55 (2004), pp. 427–455. DOI: 10.1146/annurev.physchem.55.091602.094449.

[105] C. A. Ullrich, U. J. Gossmann, and E. K. U. Gross. "Time-Dependent Optimized Effective Potential". In: *Physical Review Letters* 74.6 (Feb. 6, 1995), pp. 872–875. ISSN: 0031-9007, 1079-7114. DOI: 10.1103/PhysRevLett.74.872.

[106] John F. Dobson, M. J. Bünner, and E. K. U. Gross. "Time-Dependent Density Functional Theory beyond Linear Response: An Exchange-Correlation Potential with Memory". In: *Physical Review Letters* 79.10 (Sept. 8, 1997), pp. 1905–1908. ISSN: 0031-9007, 1079-7114. DOI: 10.1103/PhysRevLett.79.1905.

[107] Xavier Gonze. "Adiabatic Density-Functional Perturbation Theory". In: *Physical Review A* 52.2 (Aug. 1, 1995), pp. 1096–1114. ISSN: 1050-2947, 1094-1622. DOI: 10.1103/PhysRevA.52.1096.

[108] Vladimir Goncharov. *Non-Linear Optical Response in Atoms, Molecules and Clusters: An Explicit Time Dependent Density Functional Approach*. Springer, 2014.

[109] G. Kresse and J. Furthmüller. "Efficient Iterative Schemes for *Ab Initio* Total-Energy Calculations Using a Plane-Wave Basis Set". In: *Physical Review B* 54.16 (Oct. 15, 1996), pp. 11169–11186. ISSN: 0163-1829, 1095-3795. DOI: 10.1103/PhysRevB.54.11169.

[110] Stefano Baroni et al. “Phonons and Related Crystal Properties from Density-Functional Perturbation Theory”. In: *Reviews of Modern Physics* 73.2 (July 6, 2001), pp. 515–562. ISSN: 0034-6861, 1539-0756. DOI: 10.1103/RevModPhys.73.515.

[111] Stewart J. Clark et al. “First Principles Methods Using CASTEP”. In: *Zeitschrift für Kristallographie - Crystalline Materials* 220.5/6 (Oct. 21, 2004). ISSN: 2196-7105, 2194-4946. DOI: 10.1524/zkri.220.5.567.65075.

[112] Stewart Clark. *Introduction to Parallelism in CASTEP*. online resource. URL: http://www.castep.org/files/workshop_lectures_2012/parallel_castep.pdf.

[113] Jun Chen, Liangjie Fu, and Huaming Yang. “Parallel Efficiency and Parametric Optimization in CASTEP”. In: *2011 Fourth International Symposium on Parallel Architectures, Algorithms and Programming* (2011), pp. 14–18. DOI: 10.1109/PAAP.2011.56.

[114] P. Giannozzi et al. “Quantum ESPRESSO: A Modular and Open-Source Software Project for Quantum Simulations of Materials”. In: *Journal of Physics: Condensed Matter* 21.39 (Sept. 30, 2009), p. 395502. ISSN: 0953-8984, 1361-648X. DOI: 10.1088/0953-8984/21/39/395502. arXiv: 0906.2569 [cond-mat].

[115] Xavier Gonze et al. “The Abinit project: Impact, environment and recent developments”. In: *Comput. Phys. Commun.* 248 (2020), p. 107042. DOI: 10.1016/j.cpc.2019.107042.

[116] Neil W Ashcroft. *Solid state physics*. eng. New York ; London: Holt, Rinehart and Winston , Brooks/Cole, 1976. ISBN: 0030839939.

[117] Dominik Bogdan Jochym. “Development of non-local density functional methods”. PhD thesis. Durham University, 2008. URL: http://etheses.dur.ac.uk/2174/.

[118] Paul R. Tulip. “Dielectric and Lattice Dynamical Properties of Molecular Crystals via Density Functional Perturbation Theory: Implementation within a First Principles Code”. Durham theses, Durham University. Available at Durham E-Theses Online: http://etheses.dur.ac.uk/2969/. PhD thesis. Durham University, 2004.

[119] James D. Pack and Hendrik J. Monkhorst. “"Special Points for Brillouin-zone Integrations"—a Reply”. In: *Physical Review B* 16.4 (Aug. 15, 1977), pp. 1748–1749. ISSN: 0556-2805. DOI: 10.1103/PhysRevB.16.1748.

[120] Hendrik J. Monkhorst and James D. Pack. “Special Points for Brillouin-zone Integrations”. In: *Physical Review B* 13.12 (June 15, 1976), pp. 5188–5192. ISSN: 0556-2805. DOI: 10.1103/PhysRevB.13.5188.

[121] Matthew Smith, Arjen Tamerus, and Phil Hasnip. “Portable Acceleration of Materials Modeling Software: CASTEP, GPUs, and OpenACC”. In: *Computing in Science & Engineering* 24.1 (Jan. 1, 2022), pp. 46–55. ISSN: 1521-9615, 1558-366X. DOI: 10.1109/MCSE.2022.3141714.

[122] Dominik Jochym et al. “Boosting the Scaling Performance of CASTEP: Enabling next Generation HPC for next Generation Science”. In: *Hector CSE Reports* (2012).

[123] Andrea Dal Corso, Alfredo Pasquarello, and Alfonso Baldereschi. “Density-functional perturbation theory for lattice dynamics with ultrasoft pseudopotentials”. eng. In: *Physical review. B, Condensed matter* 56.18 (1997), R11369–R11372. ISSN: 0163-1829.

[124] Andrea Urru and Andrea Dal Corso. "Density Functional Perturbation Theory for Lattice Dynamics with Fully Relativistic Ultrasoft Pseudopotentials: The Magnetic Case". In: *Physical Review B* 100.4 (July 12, 2019), p. 045115. ISSN: 2469-9950, 2469-9969. DOI: 10.1103/PhysRevB.100.045115.

[125] Philipp Löper et al. "Complex Refractive Index Spectra of $CH_3NH_3PbI_3$ Perovskite Thin Films Determined by Spectroscopic Ellipsometry and Spectrophotometry". In: *The Journal of Physical Chemistry Letters* 6.1 (Jan. 2, 2015), pp. 66–71. ISSN: 1948-7185, 1948-7185. DOI: 10.1021/jz502471h.

[126] S.W. Lovesey. *Theory of Neutron Scattering from Condensed Matter*. International series of monographs on physics v. 1. Clarendon, 1984. URL: https://books.google.co.uk/books?id=7b8pxAEACAAJ.

[127] R. Vollmer et al. "Spin-Polarized Electron Energy Loss Spectroscopy of High Energy, Large Wave Vector Spin Waves in Ultrathin fcc Co Films on Cu(001)". In: *Phys. Rev. Lett.* 91 (14 Sept. 2003), p. 147201. DOI: 10.1103/PhysRevLett.91.147201.

[128] M. Plihal, D. L. Mills, and J. Kirschner. "Spin Wave Signature in the Spin Polarized Electron Energy Loss Spectrum of Ultrathin Fe Films: Theory and Experiment". In: *Phys. Rev. Lett.* 82 (12 Mar. 1999), pp. 2579–2582. DOI: 10.1103/PhysRevLett.82.2579.

[129] Kurt A. Johnson and N. W. Ashcroft. "Corrections to Density-Functional Theory Band Gaps". In: *Physical Review B* 58.23 (Dec. 15, 1998), pp. 15548–15556. ISSN: 0163-1829, 1095-3795. DOI: 10.1103/PhysRevB.58.15548.

[130] L. J. Sham and M. Schlüter. "Density-Functional Theory of the Energy Gap". In: *Physical Review Letters* 51.20 (Nov. 14, 1983), pp. 1888–1891. ISSN: 0031-9007. DOI: 10.1103/PhysRevLett.51.1888.

[131] John P. Perdew et al. "Density-Functional Theory for Fractional Particle Number: Derivative Discontinuities of the Energy". In: *Physical Review Letters* 49.23 (Dec. 6, 1982), pp. 1691–1694. ISSN: 0031-9007. DOI: 10.1103/PhysRevLett.49.1691.

[132] John P. Perdew and Mel Levy. "Physical Content of the Exact Kohn-Sham Orbital Energies: Band Gaps and Derivative Discontinuities". In: *Physical Review Letters* 51.20 (Nov. 14, 1983), pp. 1884–1887. ISSN: 0031-9007. DOI: 10.1103/PhysRevLett.51.1884.

[133] Stewart J. Clark and John Robertson. "Screened Exchange Density Functional Applied to Solids". In: *Physical Review B* 82.8 (Aug. 27, 2010), p. 085208. ISSN: 1098-0121, 1550-235X. DOI: 10.1103/PhysRevB.82.085208.

[134] Lars Hedin. "New Method for Calculating the One-Particle Green's Function with Application to the Electron-Gas Problem". In: *Physical Review* 139 (3A Aug. 2, 1965), A796–A823. ISSN: 0031-899X. DOI: 10.1103/PhysRev.139.A796.

[135] Dorothea Golze, Marc Dvorak, and Patrick Rinke. "The GW Compendium: A Practical Guide to Theoretical Photoemission Spectroscopy". In: *Frontiers in Chemistry* 7 (July 9, 2019), p. 377. ISSN: 2296-2646. DOI: 10.3389/fchem.2019.00377. arXiv: 1912.04893.

[136] H Lambert and Henry Allen Robert Lambert. "Electronic excitations in semiconductors and insulators using the Sternheimer-GW method". PhD thesis. University of Oxford, 2014.

[137] E G Maksimov et al. “Excitation Spectra of Semiconductors and Insulators: A Density-Functional Approach to Many-Body Theory”. In: *Journal of Physics: Condensed Matter* 1.14 (Apr. 10, 1989), pp. 2493–2504. ISSN: 0953-8984, 1361-648X. DOI: 10.1088/0953-8984/1/14/005.

[138] Tom Ziegler, Mykhaylo Krykunov, and Jochen Autschbach. “Derivation of the RPA (Random Phase Approximation) Equation of ATDDFT (Adiabatic Time Dependent Density Functional Ground State Response Theory) from an Excited State Variational Approach Based on the Ground State Functional”. In: *Journal of Chemical Theory and Computation* 10.9 (Sept. 9, 2014), pp. 3980–3986. ISSN: 1549-9618, 1549-9626. DOI: 10.1021/ct500385a.

[139] Erik G. C. P. van Loon et al. “Random Phase Approximation for Gapped Systems: Role of Vertex Corrections and Applicability of the Constrained Random Phase Approximation”. In: *Physical Review B* 104.4 (July 22, 2021), p. 045134. ISSN: 2469-9950, 2469-9969. DOI: 10.1103/PhysRevB.104.045134.

[140] Stephen L. Adler. “Quantum Theory of the Dielectric Constant in Real Solids”. In: *Physical Review* 126.2 (Apr. 15, 1962), pp. 413–420. ISSN: 0031-899X. DOI: 10.1103/PhysRev.126.413.

[141] Nathan Wiser. “Dielectric Constant with Local Field Effects Included”. In: *Physical Review* 129.1 (Jan. 1, 1963), pp. 62–69. ISSN: 0031-899X. DOI: 10.1103/PhysRev.129.62.

[142] Davis M. Welakuh et al. “Frequency-Dependent Sternheimer Linear-Response Formalism for Strongly Coupled Light–Matter Systems”. In: *Journal of Chemical Theory and Computation* 18.7 (July 12, 2022), pp. 4354–4365. ISSN: 1549-9618, 1549-9626. DOI: 10.1021/acs.jctc.2c00076.

[143] Feliciano Giustino, Marvin L Cohen, and Steven G Louie. “GW Method with the Self-Consistent Sternheimer Equation”. In: *Phys. Rev. B* 81 (11 2010), p. 17. DOI: 10.1103/PhysRevB.81.115105.

[144] Henry Lambert and Feliciano Giustino. “Ab Initio Sternheimer-GW Method for Quasiparticle Calculations Using Plane Waves”. In: *Physical Review B* 88.7 (Aug. 8, 2013), p. 075117. ISSN: 1098-0121, 1550-235X. DOI: 10.1103/PhysRevB.88.075117.

[145] G M Del Corso, O Menchi, and F Romani. *Krylov Subspace Methods for Solving Linear Systems*. Tech. rep. URL: https://core.ac.uk/download/pdf/144217006.pdf. Universita di Pisa Dipartimento di Informatica, 2015.

[146] Jörg Liesen and Zdenek Strakos. *Krylov subspace methods principles and analysis*. Numerical Mathematics and Scientific Computation. Oxford University Press, 2012.

[147] Claude Lemaréchal. “Cauchy and the Gradient Method”. In: *Optimization Stories*. Ed. by Martin Grötschel. 1st ed. EMS Press, Jan. 1, 2012, pp. 251–254. DOI: 10.4171/dms/6/27.

[148] M.J. Box. *Non-linear Optimization Techniques, by M.J. Box, D. Davies and W.H. Swann*. Mathematical and Statistical Techniques for Industry, Monograph no. 5. Oliver and Boyd for Imperial Chemical Industries, 1969. URL: https://books.google.co.uk/books?id=xBLsjgEACAAJ.

[149] David G. Luenberger and Yinyu Ye. *Linear and nonlinear programming*. Springer, 2021.

[150] Stephen G. Nash and Ariela Sofer. *Linear and nonlinear programming*. McGraw-Hill, 2003.

[151] Dimitri P. Bertsekas and John N. Tsitsiklis. "Gradient Convergence in Gradient Methods with Errors". In: *SIAM Journal on Optimization* 10.3 (Jan. 2000), pp. 627–642. ISSN: 1052-6234, 1095-7189. DOI: 10.1137/S1052623497331063.

[152] Gérard Meurant. "On Prescribing the Convergence Behavior of the Conjugate Gradient Algorithm". In: *Numerical Algorithms* 84.4 (Aug. 2020), pp. 1353–1380. ISSN: 1017-1398, 1572-9265. DOI: 10.1007/s11075-019-00851-2.

[153] Z. Strakoš. "On the Real Convergence Rate of the Conjugate Gradient Method". In: *Linear Algebra and its Applications* 154–156 (Aug. 1991), pp. 535–549. ISSN: 00243795. DOI: 10.1016/0024-3795(91)90393-B.

[154] Desmond J. Higham. "Condition Numbers and Their Condition Numbers". In: *Linear Algebra and its Applications* 214 (Jan. 1995), pp. 193–213. ISSN: 00243795. DOI: 10.1016/0024-3795(93)00066-9.

[155] Nick Woods. *On the Nature of Self-Consistency in Density Functional Theory*. Mar. 5, 2018. arXiv: 1803.01763 [cond-mat, physics:physics].

[156] Michael P. Teter, Michael C. Payne, and Douglas C. Allan. "Solution of Schrödinger's Equation for Large Systems". In: *Physical Review B* 40.18 (Dec. 15, 1989), pp. 12255–12263. ISSN: 0163-1829. DOI: 10.1103/PhysRevB.40.12255.

[157] Gerard L.G. Sleijpen and Henk A. van der Vorst. "An Overview of Approaches for the Stable Computation of Hybrid BiCG Methods". In: *Applied Numerical Mathematics* 19.3 (Dec. 1995), pp. 235–254. ISSN: 01689274. DOI: 10.1016/0168-9274(95)00085-2.

[158] H. A. van der Vorst. "Bi-CGSTAB: A Fast and Smoothly Converging Variant of Bi-CG for the Solution of Nonsymmetric Linear Systems". In: *SIAM Journal on Scientific and Statistical Computing* 13.2 (1992), pp. 631–644. DOI: 10.1137/0913035.

[159] Xavier Gonze and Changyol Lee. "Dynamical Matrices, Born Effective Charges, Dielectric Permittivity Tensors, and Interatomic Force Constants from Density-Functional Perturbation Theory". In: *Physical Review B* 55.16 (Apr. 15, 1997), pp. 10355–10368. ISSN: 0163-1829, 1095-3795. DOI: 10.1103/PhysRevB.55.10355.

[160] Xavier Gonze. "First-Principles Responses of Solids to Atomic Displacements and Homogeneous Electric Fields: Implementation of a Conjugate-Gradient Algorithm". In: *Physical Review B* 55.16 (Apr. 15, 1997), pp. 10337–10354. ISSN: 0163-1829, 1095-3795. DOI: 10.1103/PhysRevB.55.10337.

[161] P J Hasnip et al. *Band Parallelism in CASTEP: Scaling to More Than 1000 Cores*. Tech. rep. STFC, Rutherford Appleton Laboratory and Daresbury Laboratory, UK, 2009.

[162] Randolph E. Bank and Tony F. Chan. "An Analysis of the Composite Step Biconjugate Gradient Method". In: *Numerische Mathematik* 66.1 (Dec. 1993), pp. 295–319. ISSN: 0029-599X, 0945-3245. DOI: 10.1007/BF01385699.

[163] Charles H. Tong and Qiang Ye. "Analysis of the Finite Precision Bi-Conjugate Gradient Algorithm for Nonsymmetric Linear Systems". In: *Mathematics of Computation* 69.232 (Aug. 19, 1999), pp. 1559–1576. ISSN: 0025-5718. DOI: 10.1090/S0025-5718-99-01171-0.

[164] Keith Refson, Paul R. Tulip, and Stewart J. Clark. "Variational Density-Functional Perturbation Theory for Dielectrics and Lattice Dynamics". In: *Physical Review B* 73.15 (Apr. 19, 2006), p. 155114. ISSN: 1098-0121, 1550-235X. DOI: 10.1103/PhysRevB.73.155114.

[165] Roland W. Freund, Martin H. Gutknecht, and Noël M. Nachtigal. "An Implementation of the Look-Ahead Lanczos Algorithm for Non-Hermitian Matrices". In: *SIAM Journal on Scientific Computing* 14.1 (Jan. 1993), pp. 137–158. ISSN: 1064-8275, 1095-7197. DOI: 10.1137/0914009.

[166] C. Brezinski, M. Redivo Zaglia, and H. Sadok. "A Breakdown-Free Lanczos Type Algorithm for Solving Linear Systems". In: *Numerische Mathematik* 63.1 (Dec. 1992), pp. 29–38. ISSN: 0029-599X, 0945-3245. DOI: 10.1007/BF01385846.

[167] C Brezinski and M Redivo-Zaglia. "Transpose-Free Lanczos-type Algorithms for Nonsymmetric Linear Systems". In: *Numerical Algorithms* (May 1, 1998). DOI: https://doi.org/10.1023/A:1012085428800.

[168] Diederik R. Fokkema, Gerard L.G. Sleijpen, and Henk A. Van der Vorst. "Generalized Conjugate Gradient Squared". In: *Journal of Computational and Applied Mathematics* 71.1 (July 1996), pp. 125–146. ISSN: 03770427. DOI: 10.1016/0377-0427(95)00227-8.

[169] Silvana Botti et al. "Long-Range Contribution to the Exchange-Correlation Kernel of Time-Dependent Density Functional Theory". In: *Physical Review B* 69.15 (Apr. 23, 2004), p. 155112. ISSN: 1098-0121, 1550-235X. DOI: 10.1103/PhysRevB.69.155112.

[170] P. Lautenschlager et al. "Temperature Dependence of the Dielectric Function and Interband Critical Points in Silicon". In: *Physical Review B* 36.9 (Sept. 15, 1987), pp. 4821–4830. ISSN: 0163-1829. DOI: 10.1103/PhysRevB.36.4821.

[171] C-Y Wang et al. "Real Time Scissor Correction in TD-DFT". In: *Journal of Physics: Condensed Matter* 31.21 (May 29, 2019), p. 214002. ISSN: 0953-8984, 1361-648X. DOI: 10.1088/1361-648X/ab048a.

[172] Zachary H. Levine and Douglas C. Allan. "Linear Optical Response in Silicon and Germanium Including Self-Energy Effects". In: *Physical Review Letters* 63.16 (Oct. 16, 1989), pp. 1719–1722. ISSN: 0031-9007. DOI: 10.1103/PhysRevLett.63.1719.

[173] Francesco Sottile. "Response Functions of Semiconductors and Insulators : From the Bethe-Salpeter Equation to Time-Dependent Density Functional Theory". PhD thesis. ecole polytechnique, 2003.

[174] Giovanni Onida, Lucia Reining, and Angel Rubio. "Electronic Excitations: Density-Functional versus Many-Body Green's-Function Approaches". In: *Reviews of Modern Physics* 74.2 (June 7, 2002), pp. 601–659. ISSN: 0034-6861, 1539-0756. DOI: 10.1103/RevModPhys.74.601.

[175] Martin Schlipf et al. "SternheimerGW: A Program for Calculating GW Quasiparticle Band Structures and Spectral Functions without Unoccupied States". Dec. 10, 2018. arXiv: 1812.03717 [cond-mat].

[176] A. Frommer. "BiCGStab(l) For Families of Shifted Linear Systems". In: *Computing* 70.2 (Apr. 1, 2003), pp. 87–109. ISSN: 0010-485X, 1436-5057. DOI: 10.1007/s00607-003-1472-6.

[177] Ram Chhavi Sharma et al. “Gallium Arsenide and Gallium Nitride Semiconductors for Power and Optoelectronics Devices Applications”. In: *Journal of Physics: Conference Series* 2426.1 (Feb. 1, 2023), p. 012008. ISSN: 1742-6588, 1742-6596. DOI: 10.1088/1742-6596/2426/1/012008.

[178] Andrew M. Rappe et al. “Optimized Pseudopotentials”. In: *Physical Review B* 41.2 (Jan. 15, 1990), pp. 1227–1230. ISSN: 0163-1829, 1095-3795. DOI: 10.1103/PhysRevB.41.1227.

[179] P. Lautenschlager et al. “Interband Critical Points of GaAs and Their Temperature Dependence”. In: *Physical Review B* 35.17 (June 15, 1987), pp. 9174–9189. ISSN: 0163-1829. DOI: 10.1103/PhysRevB.35.9174.

[180] Waqas Mahmood and Bing Dong. “Application of k $$\cdot $$ p Method on Band Structure of GaAs Obtained through Joint Density-Functional Theory”. In: *Bulletin of Materials Science* 43.1 (Dec. 2020), p. 235. ISSN: 0250-4707, 0973-7669. DOI: 10.1007/s12034-020-02204-5.

[181] Rita John and S. Padmavathi. “Ab Initio Calculations on Structural, Electronic and Optical Properties of ZnO in Wurtzite Phase”. In: *Crystal Structure Theory and Applications* 05.02 (2016), pp. 24–41. ISSN: 2169-2491, 2169-2505. DOI: 10.4236/csta.2016.52003.

[182] G. E. Jellison and L. A. Boatner. “Optical Functions of Uniaxial ZnO Determined by Generalized Ellipsometry”. In: *Physical Review B* 58.7 (Aug. 15, 1998), pp. 3586–3589. ISSN: 0163-1829, 1095-3795. DOI: 10.1103/PhysRevB.58.3586.

[183] M. Rakel et al. “ELECTRONIC AND OPTICAL PROPERTIES OF ZnO BETWEEN 3 AND 32 eV”. In: *EPIOPTICS-9*. Proceedings of the 39th Course of the International School of Solid State Physics. Erice, Italy: WORLD SCIENTIFIC, Jan. 2008, pp. 115–123. DOI: 10.1142/9789812794031_0010.

[184] Z. Charifi, H. Baaziz, and Ali Hussain Reshak. “Ab-Initio Investigation of Structural, Electronic and Optical Properties for Three Phases of ZnO Compound”. In: *physica status solidi (b)* 244.9 (Sept. 2007), pp. 3154–3167. ISSN: 03701972, 15213951. DOI: 10.1002/pssb.200642471.

[185] H.I. Berrezoug et al. “Ab-Initio Calculations of Structural, Electronic, and Dielectric Properties of ZnO”. In: *2014 North African Workshop on Dielectic Materials for Photovoltaic Systems (NAWDMPV)*. 2014 North African Workshop on Dielectric Materials for Photovoltaic Systems (NAWDMPV). Tlemcen: IEEE, Oct. 2014, pp. 1–5. DOI: 10.1109/NAWDMPV.2014.6997621.

[186] A. Schleife et al. “First-Principles Study of Ground- and Excited-State Properties of MgO , ZnO , and CdO Polymorphs”. In: *Physical Review B* 73.24 (June 21, 2006), p. 245212. ISSN: 1098-0121, 1550-235X. DOI: 10.1103/PhysRevB.73.245212.

[187] A. Schleife et al. “Optical and Energy-Loss Spectra of MgO, ZnO, and CdO from *Ab Initio* Many-Body Calculations”. In: *Physical Review B* 80.3 (July 10, 2009), p. 035112. ISSN: 1098-0121, 1550-235X. DOI: 10.1103/PhysRevB.80.035112.

[188] M. K. Yaakob et al. “First Principles LDA+U Calculations for ZnO Materials”. In: *Integrated Ferroelectrics* 155.1 (July 24, 2014), pp. 15–22. ISSN: 1058-4587, 1607-8489. DOI: 10.1080/10584587.2014.905086.

[189] Xiao Zhang. “First Principles Calculations on ZnO Non-equilibrium Phase”. MA thesis. University of Illinois, 2016.

[190] H. El-Ghtami, A. Laref, and S. Laref. “Electronic and Optical Behaviors of Methylammonium and Formamidinium Lead Trihalide Perovskite Materials”. In: *Journal of Materials Science: Materials in Electronics* 30.1 (Jan. 2019), pp. 711–720. ISSN: 0957-4522, 1573-482X. DOI: 10.1007/s10854-018-0340-2.

[191] Guanhua Chen and William A. Goddard. “The Magnon Pairing Mechanism of Superconductivity in Cuprate Ceramics”. In: *Science* 239.4842 (1988), pp. 899–902. DOI: 10.1126/science.239.4842.899.

[192] J. Rusz, I. Turek, and M. Diviš. “Random-Phase Approximation for Critical Temperatures of Collinear Magnets with Multiple Sublattices: Gd X Compounds (X = Mg , Rh , Ni , Pd)”. In: *Physical Review B* 71.17 (May 11, 2005), p. 174408. ISSN: 1098-0121, 1550-235X. DOI: 10.1103/PhysRevB.71.174408.

[193] Robert G. Parr and Yang Weitao. *Density-Functional Theory of Atoms and Molecules*. Oxford University Press, USA, 1994. ISBN: 0195092767.

[194] Kun Cao et al. “*Ab Initio* Calculation of Spin Fluctuation Spectra Using Time-Dependent Density Functional Perturbation Theory, Plane Waves, and Pseudopotentials”. In: *Physical Review B* 97.2 (Jan. 19, 2018), p. 024420. ISSN: 2469-9950, 2469-9969. DOI: 10.1103/PhysRevB.97.024420.

[195] N Tancogne-Dejean, F G Eich, and A Rubio. “Time-Dependent Magnons from First Principles”. In: *J. Chem. Theory Comput.* (2020), p. 11.

[196] Bruno Rousseau, Asier Eiguren, and Aitor Bergara. “Efficient Computation of Magnon Dispersions within Time-Dependent Density Functional Theory Using Maximally Localized Wannier Functions”. In: *Physical Review B* 85.5 (Feb. 17, 2012), p. 054305. ISSN: 1098-0121, 1550-235X. DOI: 10.1103/PhysRevB.85.054305.

[197] Susi Lehtola et al. “Recent Developments in Libxc — A Comprehensive Library of Functionals for Density Functional Theory”. In: *SoftwareX* 7 (Jan. 2018), pp. 1–5. ISSN: 23527110. DOI: 10.1016/j.softx.2017.11.002.

[198] P. A. M. Dirac. “Note on Exchange Phenomena in the Thomas Atom”. In: *Mathematical Proceedings of the Cambridge Philosophical Society* 26.3 (1930), pp. 376–385. DOI: 10.1017/S0305004100016108.

[199] E. K. U. Gross and Walter Kohn. “Local Density-Functional Theory of Frequency-Dependent Linear Response”. In: *Physical Review Letters* 55.26 (Dec. 23, 1985), pp. 2850–2852. ISSN: 0031-9007. DOI: 10.1103/PhysRevLett.55.2850.

[200] Zhixin Qian and Giovanni Vignale. “Spin Dynamics from Time-Dependent Spin-Density-Functional Theory”. In: *Physical Review Letters* 88.5 (Jan. 17, 2002), p. 056404. ISSN: 0031-9007, 1079-7114. DOI: 10.1103/PhysRevLett.88.056404.

[201] C. -L. Fu and K. -M. Ho. “First-Principles Calculation of the Equilibrium Ground-State Properties of Transition Metals: Applications to Nb and Mo”. In: *Physical Review B* 28.10 (Nov. 15, 1983), pp. 5480–5486. ISSN: 0163-1829. DOI: 10.1103/PhysRevB.28.5480.

[202] Stefano de Gironcoli. “Lattice Dynamics of Metals from Density-Functional Perturbation Theory”. In: *Physical Review B* 51.10 (Mar. 1, 1995), pp. 6773–6776. ISSN: 0163-1829, 1095-3795. DOI: 10.1103/PhysRevB.51.6773.

[203] N D Woods, M C Payne, and P J Hasnip. "Computing the Self-Consistent Field in Kohn–Sham Density Functional Theory". In: *Journal of Physics: Condensed Matter* 31.45 (Nov. 13, 2019), p. 453001. ISSN: 0953-8984, 1361-648X. DOI: 10.1088/1361-648X/ab31c0.

[204] C. G. Broyden. "A Class of Methods for Solving Nonlinear Simultaneous Equations". In: *Mathematics of Computation* 19.92 (1965), pp. 577–593. ISSN: 0025-5718, 1088-6842. DOI: 10.1090/S0025-5718-1965-0198670-6.

[205] Péter Pulay. "Convergence acceleration of iterative sequences. the case of scf iteration". In: *Chemical physics letters* 73.2 (1980), pp. 393–398. ISSN: 0009-2614.

[206] G P Srivastava. "Broyden's Method for Self -Consistent Field Convergence Acceleration". In: *Journal of Physics A: Mathematical and General* 17.6 (1984), p. L317. DOI: 10.1088/0305-4470/17/6/002.

[207] David Vanderbilt and Steven G. Louie. "Total Energies of Diamond (111) Surface Reconstructions by a Linear Combination of Atomic Orbitals Method". In: *Physical Review B* 30.10 (Nov. 15, 1984), pp. 6118–6130. ISSN: 0163-1829. DOI: 10.1103/PhysRevB.30.6118.

[208] V. Eyert. "A Comparative Study on Methods for Convergence Acceleration of Iterative Vector Sequences". In: *Journal of Computational Physics* 124.2 (Mar. 1996), pp. 271–285. ISSN: 00219991. DOI: 10.1006/jcph.1996.0059.

[209] D. D. Johnson. "Modified Broyden's Method for Accelerating Convergence in Self-Consistent Calculations". In: *Physical Review B* 38.18 (Dec. 15, 1988), pp. 12807–12813. ISSN: 0163-1829. DOI: 10.1103/PhysRevB.38.12807.

[210] G. P. Kerker. "Efficient Iteration Scheme for Self-Consistent Pseudopotential Calculations". In: *Physical Review B* 23.6 (Mar. 15, 1981), pp. 3082–3084. ISSN: 0163-1829. DOI: 10.1103/PhysRevB.23.3082.

[211] A. L. Wysocki et al. "Spin-Density Fluctuations and the Fluctuation-Dissipation Theorem in 3d Ferromagnetic Metals". In: *Physical Review B* 96.18 (Nov. 15, 2017), p. 184418. ISSN: 2469-9950, 2469-9969. DOI: 10.1103/PhysRevB.96.184418. arXiv: 1706.00512.

[212] Paweł Buczek et al. "First-Principles Perspective on Magnetic Second Sound". In: *Physical Review B* 101.21 (June 11, 2020), p. 214420. ISSN: 2469-9950, 2469-9969. DOI: 10.1103/PhysRevB.101.214420.

[213] Paweł Buczek, Arthur Ernst, and Leonid M. Sandratskii. "Different Dimensionality Trends in the Landau Damping of Magnons in Iron, Cobalt, and Nickel: Time-dependent Density Functional Study". In: *Physical Review B* 84.17 (Nov. 18, 2011), p. 174418. ISSN: 1098-0121, 1550-235X. DOI: 10.1103/PhysRevB.84.174418.

[214] J. Schmalian et al. "Self-Consistent Summation of Many-Particle Diagrams on the Real Frequency Axis and Its Application to the FLEX Approximation". In: *Computer Physics Communications* 93.2-3 (Feb. 1996), pp. 141–151. ISSN: 00104655. DOI: 10.1016/0010-4655(95)00134-4.